FABRICATION and APPLICATION of SEMICONDUCTOR RADIATION DETECTORS in HIGH RESOLUTION NUCLEAR DECAY STUDIES

by

ALVIN HARVEY SHER

A.M., Washington University, 1965

A DISSERTATION SUBMITTED IN PARTIAL FULFILLMENT

OF THE REQUIREMENTS FOR THE DEGREE OF

DOCTOR OF PHILOSOPHY

in the Department

of

Chemistry

Simon Fraser University

© ALVIN HARVEY SHER 1967

SIMON FRASER UNIVERSITY

NOVEMBER, 1967

EXAMINING COMMITTEE APPROVAL

Professor B.D. Pate, Head
Department of Chemistry
Simon Fraser University
Research Supervisor

Professor R.G. Korteling
Department of Chemistry
Simon Fraser University
Examining Committee

Professor S.K. Lower
Department of Chemistry
Simon Fraser University
Examining Committee

Professor R.E. Bell, Director
Foster Radiation Laboratory
McGill University
External Examiner

PARTIAL COPYRIGHT LICENSE

I hereby grant to Simon Fraser University the right to lend my thesis or dissertation (the title of which is shown below) to users of the Simon Fraser University Library, and to make partial or single copies only for such users or in response to a request from the library of any other university, or other educational institution, on its own behalf or for one of its users. I further agree that permission for multiple copying of this thesis for scholarly purposes may be granted by me or the Dean of Graduate Studies. It is understood that copying or publication of this thesis for financial gain shall not be allowed without my written permission.

Title of Thesis/Dissertation:

____

____

____

____

Author: ____________________

(signature)

____

(name)

____

(date)

ABSTRACT

Factors which determine performance of lithium-drifted semiconductor radiation detectors, particularly lithium-drifted germanium detectors for gamma-ray spectroscopy, are discussed in terms of general semiconductor theory. The analysis includes the effects of electronic noise and the statistical effects of radiation-induced ionization and charge collection in semiconductors.

The fabrication technique is discussed for obtaining small volume planar Ge(Li) detectors and large volume (totally compensated) Ge(Li) detectors using the lithium-ion drifting process. In the case of detectors of the former type, devices have been fabricated with unusual operating characteristics; excellent resolution has been obtained from such devices at collection fields as low as 15 volts/mm. A new technique for treating the exposed surfaces of Ge(Li) detectors by coating them with a layer of CaF_2 which both lowers detector leakage current and protects the surface from exposure to the ambient is discussed.

An estimate of the Fano factor in germanium has been made using Ge(Li) detectors. The value of $F = 0.11 \pm 0.05$ has been obtained, and this result as well as previous ones is discussed in terms of the charge collection efficiency of Ge(Li) detectors, the interaction of gamma-rays with matter and the radiation-induced ionization process, and recent theoretical predictions for the Fano factor.

The calibration and use of Ge(Li) detectors for gamma-ray spectroscopy is discussed. Detectors fabricated in this laboratory have been used as gamma-ray spectrometers in high resolution nuclear decay studies.

In the study of the decay of Co^{56} and Mn^{56} two previously unobserved gamma-rays have been detected at energies of 3119.3 keV and 3598.7 keV;

these new transitions result in placing of two levels in Fe^{56} at energies of 3119.3 keV and 4445.3 keV which have been previously observed only in nuclear reaction studies. The present study, which has included both single Ge(Li) detector measurements and two-parameter coincidence experiments using a Ge(Li) detector and NaI(Tl) detector, has confirmed the existence of certain other energy levels in Fe^{56} and has provided added information on spin and parity assignments to the levels.

The nuclear decay study of Ge^{66} has yielded new results for the levels in Ga^{66}. A gamma-ray of energy 536.9 keV has been detected for the first time resulting in the placement of a new energy level in Ga^{66} of this energy. The previously reported gamma-ray of energy 185 keV has been resolved with Ge(Li) detectors into two transitions of energies 181.9 keV and 189.8 keV. The existence of a gamma-ray of energy 515.0 keV has been postulated; more precise values for the energies of the other gamma-rays from the decay of Ge^{66} have been obtained and a revised decayed scheme has been constructed.

The decay of Ga^{68} has been studied using Ge(Li) detectors and preliminary gamma-ray data obtained.

FABRICATION and APPLICATION of SEMICONDUCTOR RADIATION DETECTORS in HIGH RESOLUTION NUCLEAR DECAY STUDIES

TABLE of CONTENTS

	Page
INTRODUCTION	1
PART ONE - Lithium-Drifted Semiconductor Radiation Detectors: Theory	3
CHAPTER I Introductory Theory	4
1.1 Properties of Semiconductors	4
1.1.1 Band Theory of Solids	4
1.1.2 Intrinsic Conductivity	7
1.1.3 The Fermi Level	11
1.1.4 Impurity Conductivity	13
1.1.5 Energy Levels of Impurity Atoms	16
1.1.6 Properties of Germanium	18
1.2 Semiconductor Junctions	18
1.2.1 p-n Junctions	19
1.2.2 p-i-n Junctions	24
CHAPTER II Characteristics of p-i-n Junctions	28
2.1 Production of Charge	29
2.1.1 Interaction of Gamma-rays with Matter	32
2.1.2 Statistics of Charge Production	34
2.2 Effects of Charge Collection	40
2.2.1 Plasma Recombination	40
2.2.2 Carrier Trapping	40

	Page
2.3 Detector Noise	44
2.3.1 Bulk Generated Leakage Current	44
2.3.2 Noise Due to Poor Electrical Contacts	46
2.3.3 Surface Generated Noise	47
PART TWO- Fabrication of Lithium-Drifted Germanium Radiation Detectors: Experiment	54
CHAPTER III Experimental Technique	55
3.1 DC-Drift	56
3.1.1 Sawing and Lapping	56
3.1.2 Lithium Diffusion	57
3.1.3 Etching	59
3.1.4 Lithium-ion Drift	60
3.2 AC-Drift	65
3.3 Post-Drift Procedures	69
3.3.1 Clean-up Drift	69
3.3.2 Surface Treatment	70
CHAPTER IV Experimental Results	73
4.1 Rectification Characteristics	73
4.1.1 CaF_2 Compensation of Surface States in Ge (Li) Detectors	78
4.2 Spectrometer Performance	89
CHAPTER V Operating Characteristics of Ge(Li) Detectors	94
5.1 Ge(Li) Detector Response	94
5.2 Detector Efficiency	98
5.2.1 Full-Energy Peak Efficiency	98

Page

5.2.2 Escape-Peak Efficiency 104

5.3 Resolution and Fano Factor 106

5.3.1 Method for Determining Fano Factor 107

5.3.2 Experimental Results 108

5.3.3 Discussion of Results 111

5.3.4 Conclusion 113

PART THREE - Experimental Application of Ge(Li) Detectors: Nuclear Decay Studies 115

CHAPTER VI Spectroscopic Techniques 116

6.1 Single Detector Measurements 116

6.1.1 Location of Peak Positions 117

6.1.2 Energy Calibration and Computation 118

6.1.3 Gamma-ray Intensity Determination 121

6.2 Measurement of Coincidences Between Two Gamma-Rays 121

CHAPTER VII Nuclear Decay Studies 124

7.1 The Decay of Co^{56} and Mn^{56} 124

7.1.1 Source Preparation 125

7.1.2 Single Detector Measurements 125

7.1.3 Gamma-Gamma Coincidence Studies 136

7.1.4 Discussion of Results 137

7.1.5 Conclusion 150

7.2 The Decay of Ge^{66} 152

7.2.1 Source Preparation 152

7.2.2 Single Detector Measurements 153

7.2.3 Discussion of Results 157

Page

7.3 The Decay of Ga^{68} 161

7.3.1 Source Preparation 161

7.3.2 Single Detector Measurements 161

7.3.3 Discussion of Results 165

LITERATURE CITED 167

APPENDIX A: Four-Point Probe 173

APPENDIX B: Cryostat Design for Ge(Li) Detectors 176

APPENDIX C: Standard Gamma-Ray Energies used in Calibration Measurements 180

APPENDIX D: FORTRAN Program MFIT 181

LIST of TABLES

		Page
I:	Properties of germanium	18
II:	Specifications of p-type germanium ingots	55
III:	Sample computer output for Ge^{66} gamma-ray energies	120
IV:	Gamma-ray energy and intensity measurements on Co^{56}	132
V:	Gamma-ray energy and intensity measurements on Mn^{56}	133
VI:	Gamma-gamma coincidences in Co^{56}	143
VII:	Gamma-ray energy and intensity measurements on Ge^{66}	156
VIII:	Gamma-ray energy and intensity measurements on Ga^{68}	164
IX:	Energies of gamma-rays assigned to impurity activities	164

LIST of FIGURES

Page

Figure 1: Energy of electronic bands in metal of low atomic number vs interatomic distance R. 6

Figure 2: Electronic energy bands in germanium vs interatomic distance R. 8

Figure 3: Energy bands for intrinsic conductivity in a semiconductor at $0^{o}K$; at right are shown the directions of the velocity and current of electrons e and holes h. 9

Figure 4: Fermi function f(E) vs energy. 12

Figure 5: Charges associated with impurity atoms in germanium; (a) donor impurity, and (b) acceptor impurity. 14

Figure 6: Ionization energy of donor and acceptor atoms in germanium. 17

Figure 7: p-n junction at equilibrium. 20

Figure 8: p-n junction under reverse bias. 22

Figure 9: (a) Electron potentials for a p-i-n junction under reverse bias, and (b) electric field in a p-i-n junction vs distance through the device. 25

Figure 10: Energy loss processes in radiation-induced ionization in semiconductors. 31

Figure 11: Gamma-ray mass attenuation coefficients for germanium. 33

Figure 12: Calculated ionization efficiency Y and Fano factor F vs K. 37

Figure 13: "Crazy carpentry" applied to radiation-induced ionization energy loss processes in semiconductors. 39

Figure 14: Charge collection efficiency η vs drift length parameter λ/w. 43

Figure 15: Percent resolution $100\sigma/q$ vs drift length parameter λ/w. 43

Figure 16: Energy level diagram for an n-type semiconductor with donor-like surface states; (a) immediately after introduction of the states, and (b) after thermal equilibrium has been reached. 49

		Page
Figure 17:	Energy level diagram indicating the various energy parameters used to characterize the space-charge region for a p-type semiconductor with (a) an accumulation layer, and (b) an inversion layer.	51
Figure 18:	Electron energy vs distance x through a p-i-n junction device. Dashed lines represent the electron potential at the surface due to the presence of an n-type inversion layer.	53
Figure 19:	Concentration of lithium donor atoms vs distance from the surface of a semiconductor crystal (a) after thermal diffusion and (b) after ion drift.	61
Figure 20:	DC-drifting bath.	63
Figure 21:	AC-drifting bath.	67
Figure 22:	Leakage current vs reverse bias for a p-i-n diode from Sylvania ingot 597G-6.	74
Figure 23:	Leakage current vs reverse bias for a p-i-n diode from Sylvania ingot 564G-1.	76
Figure 24:	Capacitance vs Bias for a p-i-n diode.	77
Figure 25:	(a) Detector mount which detaches from cold finger. Pins fabricated from BNC connectors permit uncoupling of the signal lead. (b) Schematic of the apparatus used in the CaF_2 treatment. The detector and quartz crystal monitor are approximately 20 inches above the source.	80
Figure 26:	Leakage current vs bias curves at $77^{o}K$ showing effect of 200 A^{o} CaF_2 coating on a Ge(Li) detector.	82
Figure 27:	Leakage current vs bias curves at $77^{o}K$ showing effect of 200 A^{o} coating of CaF_2 on a Ge(Li) detector.	83
Figure 28:	Leakage current vs bias curves at $77^{o}K$ showing effect of 150 A^{o} coating of CaF_2 on a Ge(Li) detector.	84
Figure 29:	Gamma-ray spectrum of Co^{57} obtained with Ge(Li) detector coated with 150 A^{o} CaF_2.	86
Figure 30:	Portion of Co^{60} gamma-ray spectrum obtained with Ge(Li) detector coated with 150 A^{o} CaF_2.	87

		Page
Figure 31:	Co^{57} gamma-ray spectrum obtained with Ge(Li) detector with bevelled edges.	90
Figure 32:	Portion of Co^{60} gamma-ray spectrum obtained with Ge(Li) detector with bevelled edges at 70 volts and 55 volts bias.	91
Figure 33:	Plot of equipotential lines for electric field across i-region of Ge(Li) detector with bevelled edges.	93
Figure 34:	Cross section of a Ge(Li) detector showing the interaction of gamma-rays with the detector.	95
Figure 35:	Gamma-ray spectrum of Na^{24} obtained with an 8 cm^3 Ge(Li) detector.	96
Figure 36:	Constant geometry source holder.	99
Figure 37:	Full-energy peak efficiency (%) vs gamma-ray energy for Ge(Li) detectors of different volumes.	100
Figure 38:	Full-energy peak efficiency vs gamma-ray energy for three Ge(Li) detectors of approximately equal volumes; a) is from ref. 35, and b) from ref.39	102
Figure 39:	Detector volume vs detection efficiency at 1 MeV.	103
Figure 40:	Escape peak data vs gamma-ray energy for Ge(Li) detectors; (a) is from ref. 43	105
Figure 41:	Detector resolution (keV^2 FWHM) vs reciprocal field strength.	109
Figure 42:	Ratio of variance-to -yield vs reciprocal field.	110
Figure 43:	Block diagram of equipment used in two-parameter coincidence experiments.	123
Figure 44:	Mn^{56} half-life determination.	126
Figure 45:	Lower energy portion of Ge(Li) detector gamma-ray spectrum from Co^{56} using biased amplifier.	128
Figure 46:	Upper energy portion of Ge(Li) detector gamma-ray spectrum from Co^{56} using biased amplifier.	129
Figure 47:	Co^{56} gamma-ray singles spectrum-low energy region.	130

		Page
Figure 48:	Regions of particular interest in the Co^{56} gamma-ray spectra.	131
Figure 49:	Mn^{56} gamma-ray singles spectrum.	134, 135
Figure 50:	Co^{56} spectrum of gamma-rays in coincidence with the 847-keV transition.	138
Figure 51:	Co^{56} spectrum of gamma-rays in coincidence with the 1038-keV transition.	139
Figure 52:	Co^{56} spectrum of gamma-rays in coincidence with the 1238-keV transition.	140
Figure 53:	Co^{56} gamma-rays in coincidence with 847-keV and 1238-keV transitions: 1600 to 2700 keV region.	141
Figure 54:	Gamma-rays in the energy-region 600 to 990 keV in coincidence with the Co^{56} 847-keV transition.	142
Figure 55:	Decay scheme of Co^{56} and Mn^{56}; beta decay data with superscript a) are from ref. 93, and b) from ref.63	144
Figure 56:	Ge^{66} gamma-ray singles spectrum: 0 to 400 keV region.	154
Figure 57:	Ge^{66} gamma-ray singles spectrum: 400 to 750 keV region.	155
Figure 58:	Decay scheme of Ge^{66}; data with superscript a) are from ref. 64	158
Figure 59:	Ga^{68} gamma-ray singles spectrum.	162, 163
Figure 60:	Decay scheme of Ga^{68} ; beta-decay data with superscript a) are from ref. 64	166
Figure A1:	Circuit for four-point probe.	174
Figure B1:	Cryostat for Ge(Li) detectors.	177
Figure B2:	Detector mounting pedestal modifications used in this laboratory.	179

ACKNOWLEDGEMENT

It is a pleasure to acknowledge the help of the Faculty and Staff of Simon Fraser University, especially the following:

Professor B.D. Pate for his guidance, criticism, and patience during the period in which this work was carried out;

F.H. Ruddy for suggesting and providing the initial sources for the decay scheme work;

Prof. R.G. Korteling, Prof. C.H.W. Jones, Dr. J.A. Coleman, J.F. O'Hanlon, and J.C. Conradi for helpful discussions;

J. Gislason for providing an extra pair of able hands during the latter stages of the detector fabrication work;

T.S.R. Bennett and Mrs. T.S.R. Bennett for their aid in data reduction; and,

Other inhabitants of the "Nuclear Suite" for diversion and discussion.

Special notice is due F. Wick (Machine Shop), W. Hall (Electronics), A. Stuart (Glassblowing) and their crews who fabricated the various pieces of equipment required, often on short notice.

I would also like to thank the Defense Research Board of Canada for support under Grant Number 1680-40, the SFU Computing Centre supported in part by National Research Council Grant Number E-997, and the crew of the University of Washington cyclotron for their hospitality.

And finally, to my wife, Adrienne, a special acknowledgement for finding the time to type the various drafts and final manuscript of this thesis while caring for our house and children.

INTRODUCTION

The use and utility of semiconductor radiation detectors is now amply documented in the literature. In evaluating tools available for nuclear spectroscopic research, one must consider at least three important criteria: (1) the resolution in energy obtainable with the system; the better the resolution, the easier it becomes to analyze complex spectra accurately; (2) the time in which a meaningful amount of data can be collected, which is of great importance in work on short-lived nuclei; and (3) the detection efficiency of the system, which places a lower limit on the strength of the source which can be used, and which also determines the effects of background or noise on the experiment.

In general, semiconductor radiation detectors represent a practical balance among these factors and overall performance is as good or better than most other available detection systems. Until very recently, the low detection efficiency of lithium-drifted germanium detectors for gamma-radiation (as compared to scintillation devices) was their greatest drawback. The development of large-volume Ge(Li) detectors, and the use of several such devices in parallel represent a step towards solving this problem.

Particularly in the field of high resolution gamma-ray spectroscopy using Ge(Li) detectors, the emphasis has recently turned from the "revolutionary" aspects of these devices to a thorough study of the theoretical and operational characteristics of lithium-drifted detectors in order to optimize their performance along with that of the associated electronic equipment. Such phenomena as charge collection, surface chemistry and physics, and characteristics of starting materials are being investigated in light of the above. There are, however, certain limitations inherent in the materials currently used for semiconductor radiation

detectors. In germanium the relatively low Z presents problems in efficient detection of gamma-rays. The difficulties in producing single crystals of germanium of sufficient size for high detection efficiency with the required degree of perfection have not as yet been overcome. Also the requirement for low temperature operation of Ge(Li) detectors limits the flexibility of the system. Thus while optimization of Ge(Li) detector systems proceeds, work has begun to find other suitable materials for use as semiconductor radiation detectors which might offer improved characteristics over present systems. The possibility of using certain compound semiconductors is under immediate investigation.[12]

It is the intent of this dissertation to examine specifically the lithium-drifted germanium detector for high resolution gamma-ray spectroscopy in terms of recent theory and experimental work undertaken to obtain optimum performance from such detectors. Along with this are presented certain nuclear decay studies which were performed using Ge(Li) detectors. In some cases, comparison is drawn with previous studies performed with other detection systems, namely crystal diffraction, internal- and external-conversion studies with magnetic spectrometers, and scintillation spectrometers.

Part One

Lithium-Drifted Semiconductor Radiation Detectors: Theory

CHAPTER I

INTRODUCTORY THEORY

1. An understanding of the operation of devices such as lithium-drifted germanium detectors must of necessity begin with a description of the properties of the base material, germanium. However certain aspects of the theory set forth to explain various processes in solid-state detectors become more complex and of less certain validity as one proceeds from describing relatively simple systems such as crystal conduction counters to diffused-junction devices to thick, lithium-drifted p-i-n junction detectors. Coupled to this is the fact that the interaction of gamma-radiation with Ge(Li) detectors and the subsequent events which produce an external signal are more complex than the interaction of charged-particles or beta-rays.

1.1 Properties of Semiconductors A semiconductor is an insulator in which at thermal equilibrium some charge carriers are mobile.[60] At absolute zero, a perfect, pure crystal of most semiconductors would be an insulator; the characteristic semiconducting properties are usually brought about by thermal agitation, impurities, lattice defects, or non-stoichiometric composition. Conductivities of solids can be grouped into three categories at room temperature[60] as follows: metals (10^5 $ohm^{-1}cm^{-1}$), semiconductors (10^2 to 10^{-9} $ohm^{-1}cm^{-1}$), and insulators (10^{-14} to 10^{-22} $ohm^{-1}cm^{-1}$).

1.1.1 Band Theory of Solids Under an applied electric field, conduction in a crystalline solid can occur only if there is superimposed upon the random motion of some of the electrons a component in the direction of the field. If closely spaced electron energy levels exist in the material, the electrons

can gain the increased energy required for the additional motion, but because of the Pauli exclusion principle, electronic transitions to levels of higher energy can occur only if such levels are unoccupied.[118]

Consider the energy levels within a single crystal. If the exclusion principle is not to be violated, i.e., if pairs of electrons are not to occupy identical quantum states, the energy levels of the various electron shells must be modified in some way. In the simplest case where two atoms of the same element are in close proximity, each energy level splits into two levels of slightly different energy, and the electrons which would have originally occupied two identical quantum states in separate systems now occupy two levels of slightly different energy in the same system.[121] In the case of many atoms bound in a lattice array in a crystal, the atomic energy levels are replaced by bands of closely-spaced energy levels. The total number of states with a given principle quantum number n, however, remains unchanged,[109] e.g., there are eight possible $n = 2$ states in an atom (two 2s and six 2p states); if N atoms are brought together, there will be exactly $8N$ states, even though there will be considerable alteration of the energies of the individual levels. The spacing of these electronic energy levels becomes small for large N, and there may exist gaps between bands of levels corresponding to different principal quantum number n, the positions of the tops and bottoms of each band being independent of the number of atoms N.[47]

Figure 1 illustrates the effect of close atomic spacing on the energy levels of a metal of low atomic number such as sodium or magnesium. As the interatomic distance R decreases, the well-defined electronic energy levels of the isolated atoms are replaced by wide bands. The outer electron shells are first affected, the innermost shells remaining isolated systems

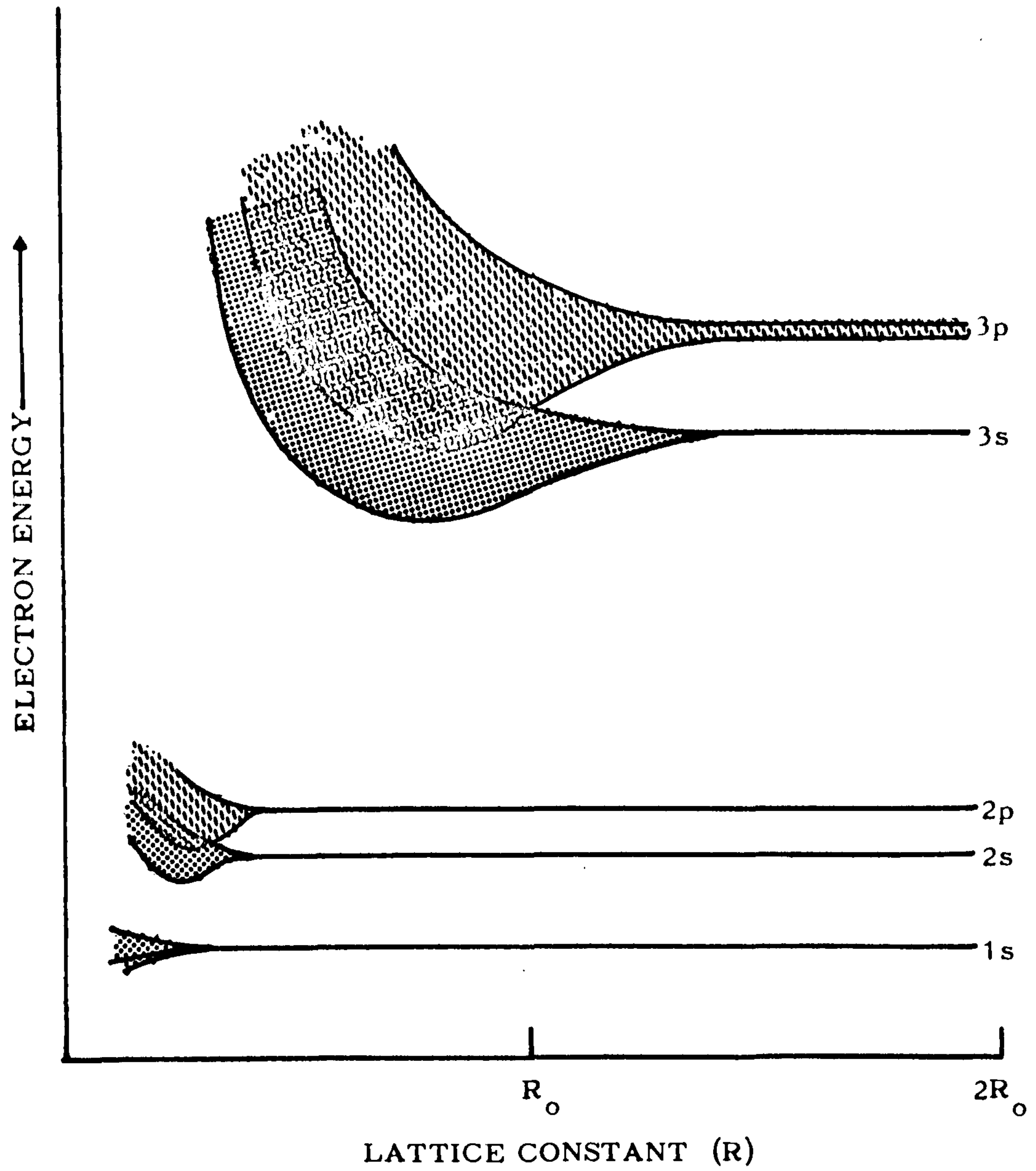

FIGURE 1: ENERGY OF ELECTRONIC BANDS OF LOW ATOMIC NUMBER METAL vs INTER-ATOMIC DISTANCE R.

down to very small values of R. At R_o, the observed lattice constant under normal conditions of temperature and pressure, it is seen that the 3s and 3p bands have overlapped, thus electrons in the 3s band have access to unfilled levels in the 3p band so that conduction can readily occur.[121]

For solids which exhibit covalent binding, such as germanium, silicon, diamond, and gray tin, the behavior of the electronic energy levels with decreasing interatomic distance is illustrated in Figure 2, for germanium. The splitting of the outer shells into bands of high and low energy is a characteristic of covalently-bound solids,[109] the upper branch corresponding to antisymmetric or non-bonding states, and the lower to symmetric or bonding states. At R_o the bands are seen to cross leaving an energy gap E_g rather than to overlap as in the case of metallic binding.

1.1.2 Intrinsic Conductivity In certain substances, e.g., germanium and silicon, the band structure is such that the uppermost filled band is separated from a higher empty band by a small energy gap E_g. The character of the electronic band scheme leading to intrinsic conductivity is indicated in Figure 3. The uppermost filled band, the valence band, is separated from the conduction band by E_g. At 0^oK the conduction band is empty of electrons, and the conductivity is zero. As the temperature is increased, the electrons are thermally excited from the valence band into the conduction band leaving vacant states or holes in the valence band. Under an applied electric field, both the electrons in the conduction band and the holes in the valence band can contribute to the electrical conductivity, the relative directions of the electron and hole currents and velocities with respect to the applied field being shown in Figure 3. The intrinsic temperature range

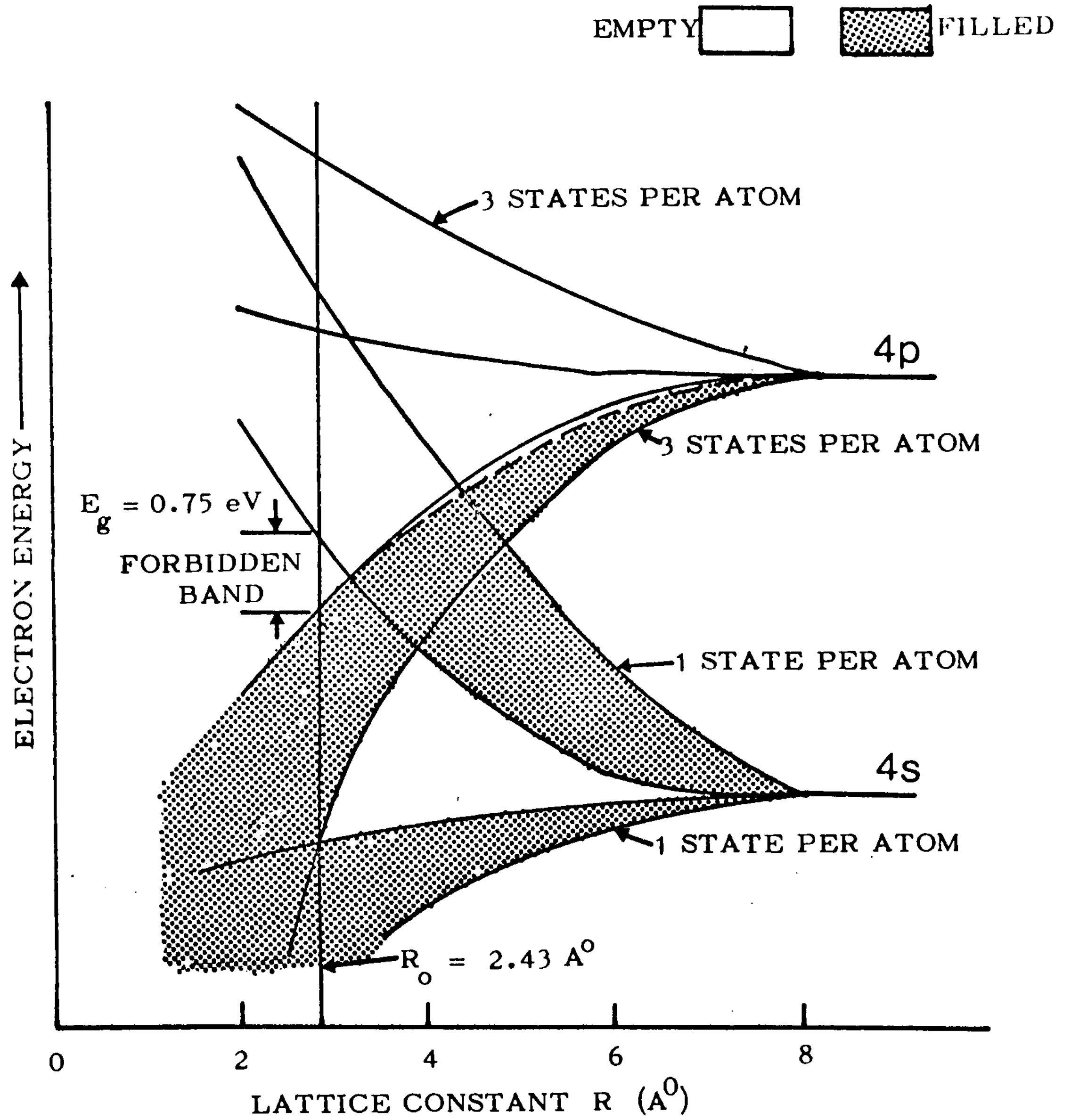

FIGURE 2: ELECTRONIC ENERGY BANDS IN GERMANIUM vs INTERATOMIC DISTANCE R.

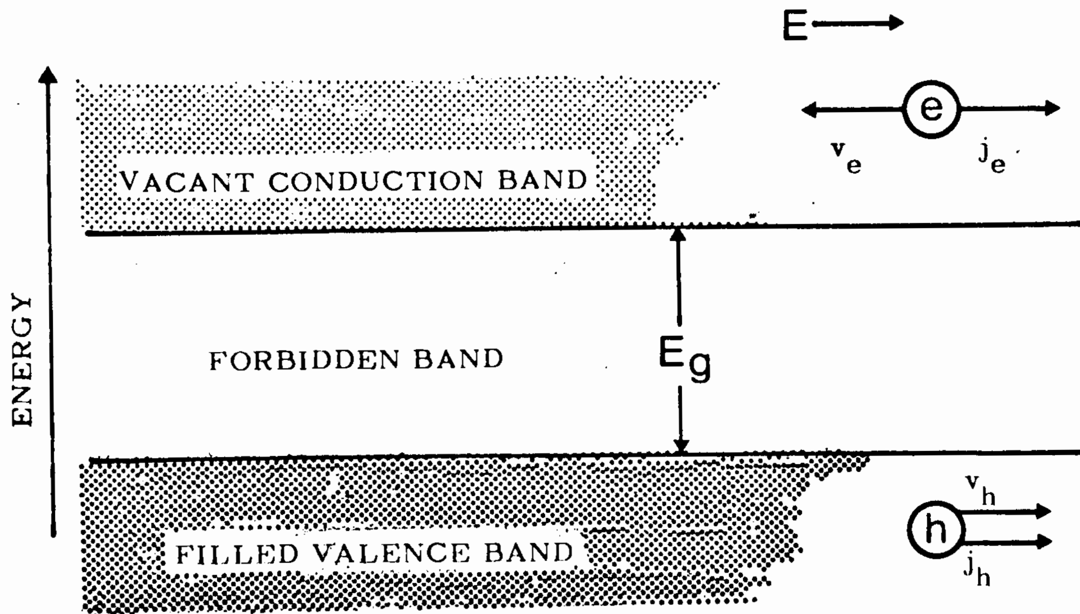

FIGURE 3: ENERGY BANDS FOR INTRINSIC CONDUCTIVITY IN A SEMICONDUCTOR AT $0^{o}K$; AT RIGHT THE DIRECTIONS OF THE VELOCITY AND CURRENT OF ELECTRONS e AND HOLES h ARE SHOWN.

is that in which the electrical properties of a semiconductor are not essentially modified by impurities in the crystal. At temperatures below the intrinsic range, the electrical properties are controlled by impurities, and we then speak of impurity or extrinsic conductivity.[60]

The total conductivity σ can be approximated[101] by:

$$\sigma = (\text{constant})\exp(-E_g/2kT) \tag{1-1}$$

where E_g is the value of the energy gap, k is the Boltzmann constant, and T is the absolute temperature. Thus by raising any insulating solid to a sufficiently high temperature (where chemically feasible) intrinsic conductivity may be expected since a large energy gap may be overcome by a large enough temperature to reduce the ratio $E_g/2kT$ in the exponential in equation 1-1.[87]

During the passage through the crystal of electrons and holes under an applied field, an electron may fall back into the valence band by recombining with a hole. An equilibrium is thus established due to the continual thermal generation and recombination of electrons and holes.[47] The law of mass action can be applied to this equilibrium; the product of the electron concentration n and hole concentration p is equal to an equilibrium constant which depends only upon the temperature T for a given solid:[60]

$$np = 4(2\pi kT/h^2)^3(m_e m_h)^{3/2}\exp(-E_g/\ kT) \tag{1-2}$$

where h is Planck's constant, m_e and m_h are the electron and hole masses, respectively. At 300°K the value of np for germanium[60] is 5.7×10^{26} cm^{-6}. In intrinsic semiconductors where the thermal excitation of an electron from the valence band leaves behind a hole, $n = p$. Introduction of a small amount of a suitable impurity into a crystal to increse n

must decrease p since the product np is a constant as given in equation 1-2.

1.1.3 <u>The Fermi Level</u> Electrons obey Fermi-Dirac statistics; thus the probability at a given temperature that a particular energy level E will be occupied is given by the Fermi function $f(E)$:

$$f(E) = \frac{1}{1 + \exp(E - E_f)/kT} \qquad (1\text{-}3)$$

where E_f is the Fermi energy or Fermi level. The general behavior of the Fermi distribution function is shown in Figure 4 in which is plotted $f(E)$ vs E for $T = 0$ and for $T \ll E_f/k$. At 0^oK $f(E) = 1$ for $E < E_f$, and $f(E) = 0$ for $E > E_f$[47], i.e., all electrons occupy the lowest energy states at 0^oK. Thus at absolute zero, E_f is the energy associated with the highest occupied state. At higher temperatures, the probability function $f(E)$ remains symmetric about E_f so that $1 - f(E)$ at an energy below E_f of ΔE is equal to $f(E)$ at ΔE above E_f; thus for $T > 0$, E_f is the energy for which $f(E) = \frac{1}{2}$.

At any temperature above zero, it is possible to determine E_f. In an intrinsic semiconductor, one hole (empty quantum state) is produced in the valence band for each electron thermally excited to the conduction band, thus the density of states is equal in both the conduction and valence bands, and:

$$f(E_g) = 1 - f(0). \qquad (1\text{-}4)$$

By substituting the explicit expressions for the $f(E)$'s from equation 1-3 into equation 1-4, one obtains:

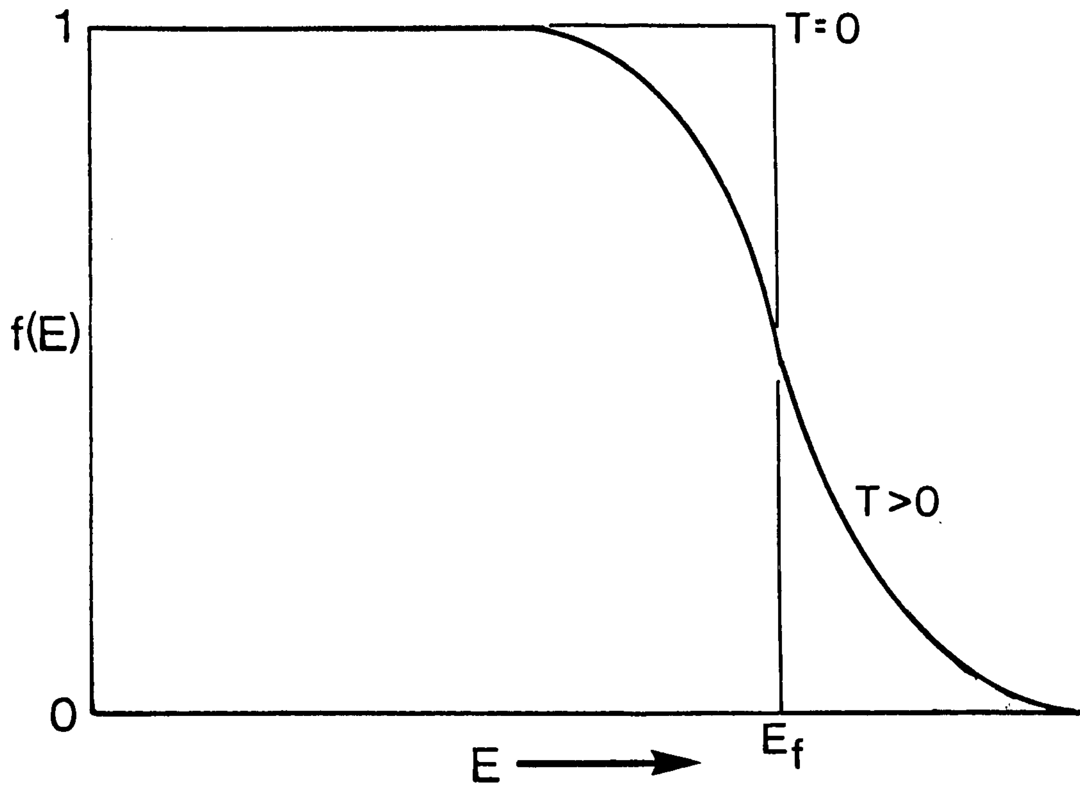

FIGURE 4: FERMI FACTOR f(E) vs ENERGY

$$\frac{1}{1 + \exp(E_g - E_f)/kT} = 1 - \frac{1}{1 + \exp(-E_f/kT)} = \frac{\exp(-E_f/kT)}{1 + \exp(-E_f/kT)}$$

$$1 + \exp(-E_f/kT) = \exp(-E_f/kT)[\exp(E_g - E_f)/kT + 1]$$

$$1 = \exp(E_g - 2E_f)/kT$$

$$E_f = E_g/2 \qquad (1\text{-}5)$$

Thus we obtain the result that in an intrinsic semiconductor, the Fermi level E_f is located midway between the top of the valence band and the bottom of the conduction band.[110]

1.1.4 Impurity Conductivity Of pertinent interest to a discussion of semiconductor radiation detectors is the case of impurity semiconductors in which electrical characteristics of the crystal can be altered drastically by the addition of certain foreign atoms in substitutional or interstitial positions in the lattice. In a germanium crystal each atom has four electrons available for bonding, resulting in an array of germanium atoms each bound to four others by covalent bonds. Three-dimensionally, each atom is bound to its neighbors in a tetrahedral configuration; however, for the purposes of the present discussion, the lattice can be represented as shown in Figure 5.

Figure 5(a) shows the situation which arises when an atom of an element from Group V, such as arsenic, replaces a germanium atom. Four of the five valence electrons in arsenic are shared with four adjacent germanium atoms to form covalent bonds similar to those existing between germanium atoms themselves. The fifth valence electron is not held in any chemical bond, but moves in the Coulomb potential of the impurity arsenic substituent.

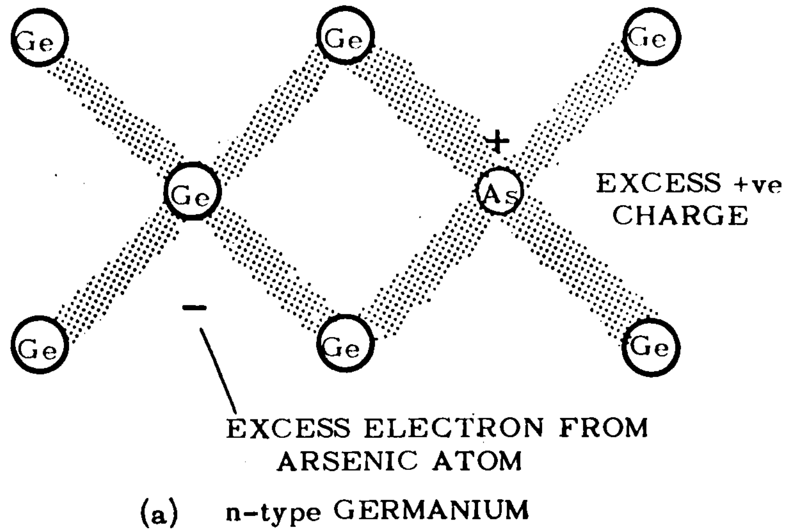

(a) n-type GERMANIUM

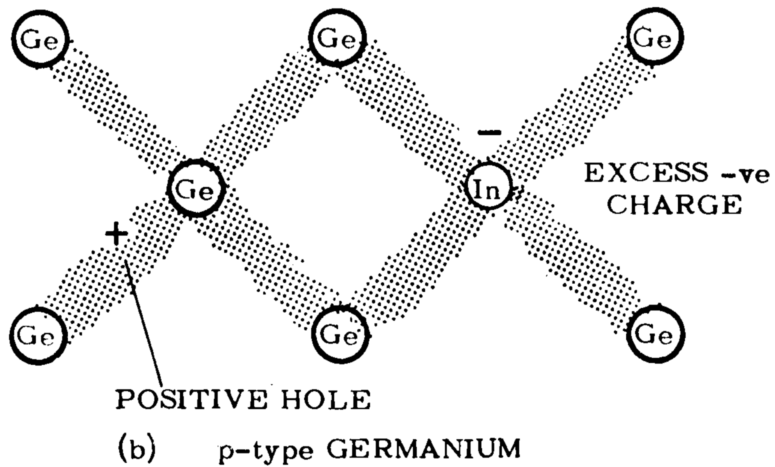

(b) p-type GERMANIUM

FIGURE 5: CHARGES ASSOCIATED WITH IMPURITY ATOMS IN GERMANIUM. (a) DONOR IMPURITY, AND (b) ACCEPTOR IMPURITY.

Under an applied field, the extra electron may be removed to the conduction band thus contributing to the electrical conductivity, and the energy required to excite the electron to the higher energy state is termed the impurity ionization energy. Such Group V impurity atoms are called "donors" since they can donate electrons to the conduction band, and germanium doped with a donor impurity is "n-type" since $n > p$; thus the majority charge carriers are negative electrons.

Lithium in germanium and silicon enters the lattice occupying an interstitial position. The single 2s valence electron is easily ionized, and the electrical consequences of interstitial donors such as lithium are similar to those of the substitutional donors such as arsenic.

The replacement of a germanium atom in a crystal by an atom of an element from Group III is illustrated in Figure 5(b), for indium. The three available valence electrons of an indium atom form covalent bonds with three of four adjacent germanium atoms, but no electron is available to complete the fourth bond. The trivalent impurities, then, can accept electrons from the valence band leaving holes in the band. "Acceptor" impurities are ionized by bringing an electron up from the valence band (electron energy increases), and taking the hole into the valence band (hole energy also increases); thus the problem is analogous to that involving donor atoms. Germanium containing excess acceptor atoms is termed "p-type" since $p > n$, and the majority charge carriers are positive holes. No case of interstitial impurities which act as acceptors has been found.[47]

Since the product np is a constant at a given temperature from equation 1-2, one can see that if excess donor atoms are present and a sufficient number are ionized, the concentration of holes is suppressed below the intrinsic value. Similarly, excess ionized acceptors will suppress the

electron concentration below the intrinsic value.

In anticipation of a more detailed discussion to follow later, impurity "compensation" can occur in a suitably doped semiconductor. The effects of donor (or acceptor) impurities can be neutralized by the addition of suitable concentrations of acceptor(or donor) atoms. Near perfect compensation can be achieved in germanium and silicon such that portions of the crystal take on the electrical characteristics of intrinsic material.

In general, the impurity semiconductor differs from the intrinsic type because of the equal numbers of electrons and holes in the latter and an unequal number in the former. Since no crystal is perfect (any macroscopic crystal may be considered imperfect if only because of the presence of its surface), the limit of intrinsic conductivity is never exactly reached. The term is usually applied to the case in which the number of donor and/or acceptor states is of negligible importance in determining the electrical characteristics of the crystal.[101]

1.1.5 Energy Levels of Impurity Atoms An estimate of the binding energy of a donor impurity can be made by modifying the result of the Bohr theory for an electron in atomic hydrogen to acccount for the dielectric constant of the semiconductor and the effective mass of the electron in the periodic potential of the crystal.[60,110] The result obtained for one-electron donors is that the level of the donor lies approximately 0.01 eV below the bottom of the conduction band.[47]

Figure 6 presents in schematic form some experimental values for donor and acceptor ionization energies in germanium.[45,118] The indicated ionization energy (in eV) is that energy required to produce the ionic state

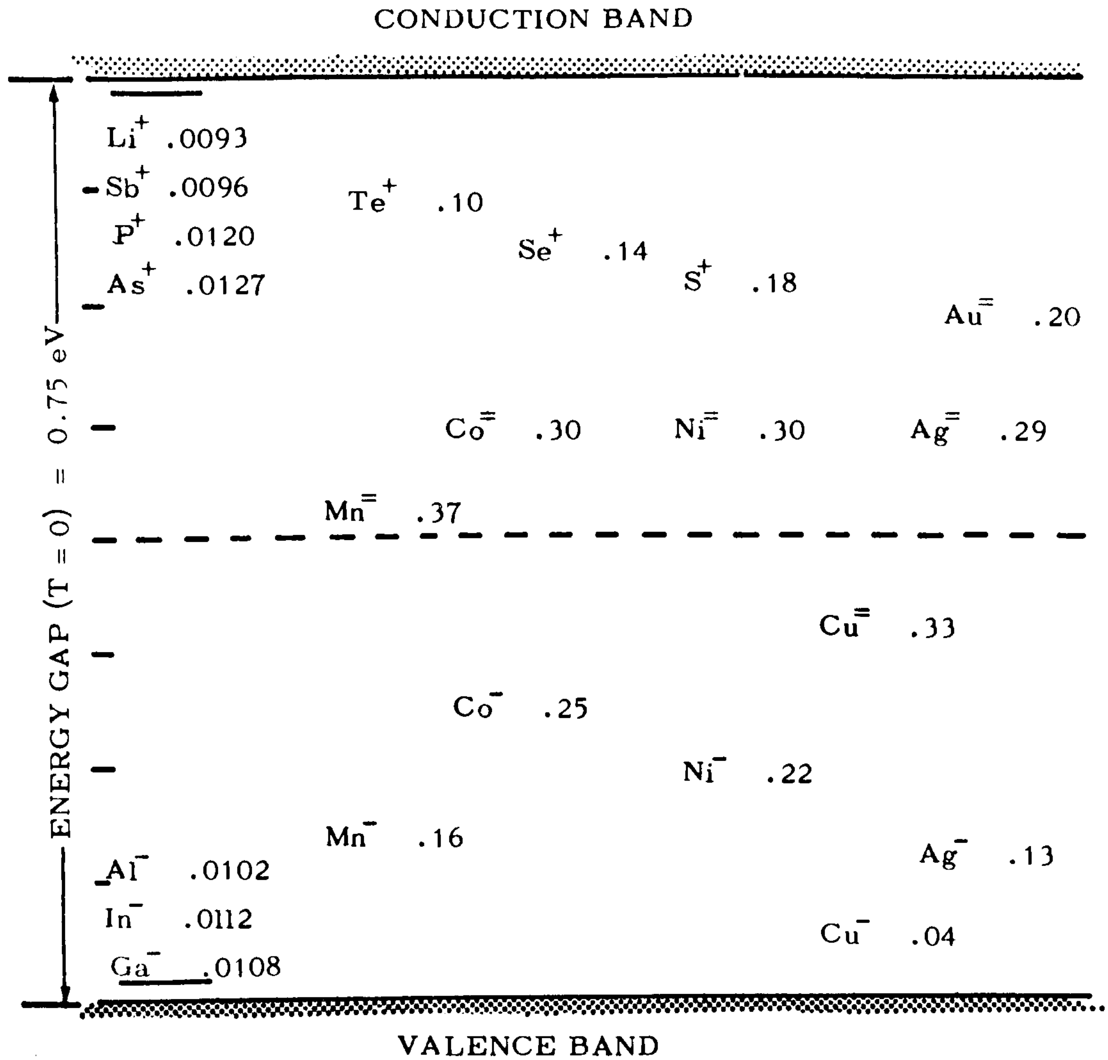

FIGURE 6: IONIZATION ENERGY OF DONOR AND ACCEPTOR ATOMS IN GERMANIUM.

shown, and is measured from the nearest band edge, i.e., bottom of the conduction band for donors and top of the valence band for acceptors. The results for the one-electron donors is in good agreement with the modified hydrogen atom approximation above, and such impurity centers are often termed "hydrogen-like."

The position of the Fermi level E_f is shifted by excess donor or acceptor concentrations. For the case of excess donor impurity centers present, E_f is shifted above its intrinsic value of $E_g/2$ by an amount depending upon the ionized impurity concentration. Similarly for excess acceptors present, E_f shifts below $E_g/2$.[110]

1.1.6 Properties of Germanium The following table summarizes certain experimentally obtained values for the properties of germanium at room temperature and 77°K.

TABLE I: Properties of Germanium[a]

T (°K)	E_g (eV)	Electron Mobility (cm^2/V-sec)	Intrinsic Resistivity (Ω -cm)	Dielectric Constant
300	0.66	3800	47	15.7
77	0.75	23,000[b]	5×10^4	

a) from ref. 121 unless otherwise noted; b) from ref. 91

1.2 Semiconductor Junctions It is possible to fabricate within a single crystal of germanium or silicon regions of n- and p-type material having a common internal boundary. Such "p-n junction" devices can be used for the detection of alpha- and beta-radioactivity, examples being diffused junction and metal-semiconductor surface-barrier detectors. Multiple

junction devices may also be constructed having n-type, intrinsic, and p-type material within a single crystal. Such "p-i-n junction" detectors of germanium are used in gamma-ray spectroscopy.

1.2.1 p-n Junctions[33,47,110,119] In order to describe the characteristics of p-i-n devices, it will be instructive first to examine p-n junctions. Figure 7 presents an electron energy diagram of a p-n junction at equilibrium, where electron energy is plotted against distance through the crystal. The convention followed is that in a region of negative charge, the electrons have higher energy than in a region of positive charge. If one considers the Fermi energy E_f as the electrochemical potential or partial molar free energy of an electron[47] then when regions of p-type and n-type material are brought into contact, their Fermi energies must be equal at equilibrium.

At equilibrium the conduction electrons contributed by the ionized donors will be found chiefly in the n-region where the electrons neutralize the space-charge of the donor ions, whereas holes contributed by acceptor ions will be found chiefly in the p-region. Electrons and holes cannot remain separated in this way unless an electric field exists in the junction region, since the electrons and holes would intermix by diffusion in the absence of such a field. If initially there is no electric field across the junction, holes will diffuse in one direction leaving behind on one side of the junction negatively charged acceptor ions, and electrons will diffuse in the opposite direction leaving positively charged donor ions. This initial diffusion of carriers will establish an electrostatic dipole layer at the junction giving rise to a potential difference ΔE which opposes futher flow across the junction.

Even in thermal equilibrium there will be a small flow of electrons J_{nr}

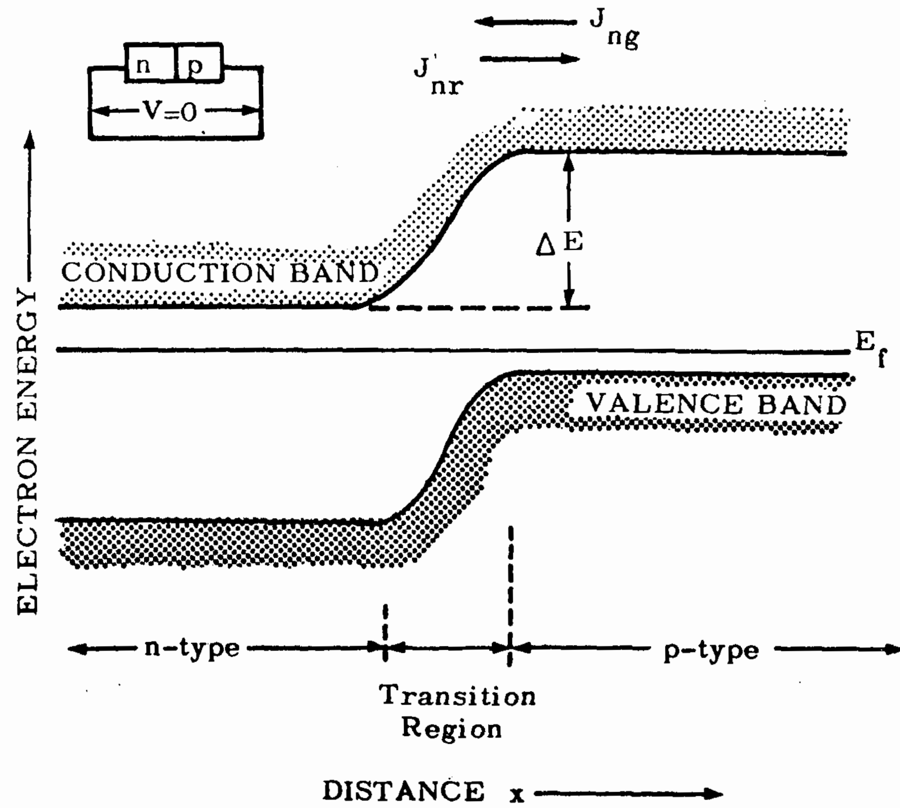

FIGURE 7: p-n JUNCTION AT EQUILIBRIUM

from the n-region into the p-region, these electrons recombining with holes. This flow will be balanced by the flow J_{ng} of electrons thermally generated in the p-region and which diffuse into the n-region.[60] In the condition of thermal equilibrium $(V = 0)$, the recombination current of electrons J_{nr} must be equal and opposite to the thermal generation electron current J_{ng} (otherwise electrons would pile up on one side of the barrier) thus:[60]

$$J_{nr}(0) + J_{ng}(0) = 0 \tag{1-6}$$

as shown in Figure 7.

The current rectification action of a p-n junction can be demonstrated assuming that nearly all of an applied voltage will appear across the transition region. Since the total carrier concentration $n + p$ is a minimum there due to the constancy of the np product as shown in equation 1-2, this is a reasonable assumption.

If a reverse or back bias (n-side positive, p-side negative) is applied to a p-n junction, the potential difference between the two regions is increased as shown in Figure 8. The generation current of electrons is not particularly affected by the reverse bias since the generation electrons are flowing down across the potential anyway:

$$J_{ng}(V \text{ reverse}) = J_{ng}(0) \tag{1-7}$$

The recombination current is affected, however, since the increased potential barrier will allow less electrons to flow across. The number of electrons which can flow across the barrier is proportional to the Boltzmann factor,[101] thus:

$$J_{nr}(V \text{ reverse}) = J_{nr}(0)\exp(-e|V|/kT) \tag{1-8}$$

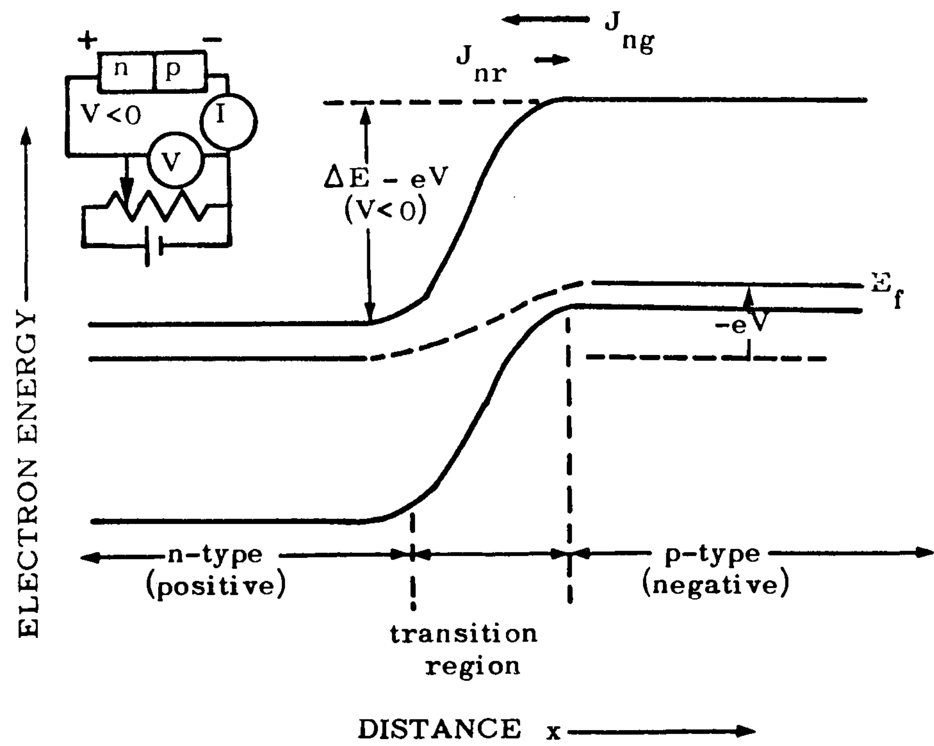

FIGURE 8: p-n JUNCTION UNDER REVERSE BIAS

When a forward bias is applied, the recombination current increases by the Boltzmann factor because the potential barrier is lowered below the equilibrium height, enabling more electrons to flow from the n- to the p-side:

$$J_{nr}(V\ \text{forward}) = J_{nr}(0)\exp(e|V|/kT) \qquad (1\text{-}9)$$

Again the generation current is unchanged:[60]

$$J_{ng}(V\ \text{forward}) = J_{ng}(0) \qquad (1\text{-}10)$$

The hole current flowing across the junction can be obtained in an analogous manner to that for electrons since the applied voltage which lowers the barrier height for electrons also lowers it for holes, so that large numbers of holes flow from the p-region to the n-region under the same conditions which produce large electron currents in the opposite direction. The electrical current due to electrons and holes add, so that the total electrical current I is given by:[101]

$$I = I_o[\exp(eV/kT) - 1] \qquad (1\text{-}11)$$

where I_o is the sum of the two generation currents. Under forward bias (defined for positive eV)[60] a p-n junction passes an exponentially increasing current with increasing voltage,

$$I \simeq I_o\exp(eV/kT) \qquad (1\text{-}12)$$

and under reverse bias (negative eV) an essentially constant current:

$$I \simeq -I_o \qquad (1\text{-}13)$$

However, when sufficient bias has been applied such that charge carrier

velocities become large enough to cause additional ionization in the solid, the current will rapidly increase. This condition is termed "avalanche breakdown."[110]

Since under a reverse bias, the thermal generation current dominates the recombination current (see equations 1-6, 1-7, and 1-8), one would expect that cooling a p-n junction will lead to reduced reverse current. It is also observed[101] that as the temperature is decreased, the ratio of reverse to forward currents decreases, and thus the rectifying action increases.

1.2.2 <u>p-i-n Junctions</u> As stated earlier, the lithium-drifted germanium detectors used in gamma-ray spectroscopy have a p-i-n structure; within a single crystal of germanium are well-defined regions of p-, "intrinsic," and n-type material. The so-called intrinsic region is actually compensated semiconductor in which, by means to be discussed later, excess acceptor atoms are in effect neutralized by an equal number of lithium donor atoms. This region thus has few free charge carriers in comparison to the impurity regions.

Operationally, the p-i-n diodes are similar to the p-n junction devices discussed above, the region depleted of charge carriers in the former being on the order of centimeters in maximum thickness while in the latter, only tenths of millimeters maximum.[119] Figure 9(a) shows the electron potentials for a p-i-n diode under reverse bias; the conventions are the same as for the p-n junction shown in Figure 8 which may be used for comparison; however, there is one important difference. The distance scale (abscissa) in Figure 9(a) is many orders of magnitude greater than in Figure 8. The potential gradient shown between the n- and p-regions

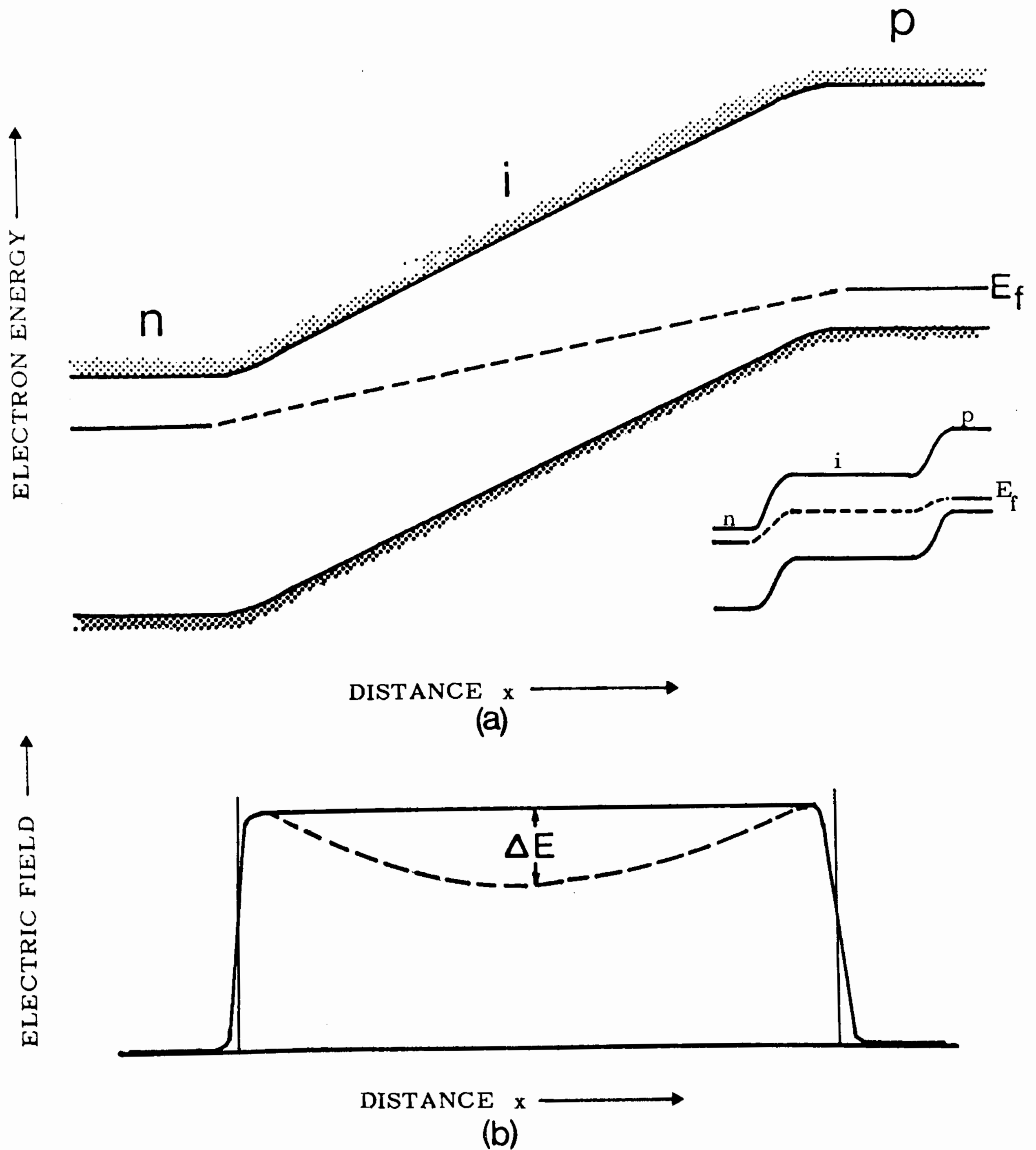

FIGURE 9: (a) p-i-n JUNCTION UNDER REVERSE BIAS

(b) ELECTRIC FIELD vs DISTANCE x THROUGH i-REGION OF p-i-n JUNCTION DEVICE

across the i-region exists since there is charge in transit across the compensated region due to thermal generation of carriers,[79] and the present representation is thought to be more accurate than that of Burford and Verner[14] which is shown in the inset of the figure.

It is instructive to examine in some detail the current flow in a reverse biased p-i-n junction. Recalling that eV is negative for the case of reverse bias and with reference to equation 1-11, the resulting current I_o may be expressed as the sum of two components similar to those in p-n junctions: the carrier diffusion current I_D, and the "depletion-region-generated current" I_{DRG}.[79] I_D arises from the diffusion of minority carriers into the junction regions, and for the case of a heavily-doped n-region and lightly-doped p-region, this component of the current can be written[79] as:

$$I_D = q(n_i^2/N_A)(D/\tau)^{\frac{1}{2}} \tag{1-14}$$

where n_i is the intrinsic carrier concentration, N_A the acceptor concentration, D the carrier diffusion coefficient, q the charge, and τ the carrier lifetime; the temperature dependence of I_D arises from the n_i^2 term.

I_{DRG} arises from electrons and holes thermally generated in the depletion region and swept out by the applied field. The value of this component is given[79] by:

$$I_{DRG} = qn_i w/2\tau \tag{1-15}$$

where w is the width of the compensated region. In comparison to the diffusion current, the magnitude of I_{DRG} is governed by n_i and w, and is frequently larger in magnitude than I_D.[79]

There is another source of reverse current in p-i-n junctions (as well as p-n devices), the surface leakage current I_L. The magnitude and behavior of I_L are strongly dependent upon the surface chemistry and physics of the diode and will be treated specifically in a later section.

As in the case of p-n junctions, almost all of an applied potential occurs across the compensated region as shown in Figure 9(b), thus the electric field can be written as V/w. At elevated temperatures, however, the net space-charge of the mobile carriers results in a perturbation of the electric field[79] (dashed curve in Figure 9(b)). This effect is of sufficient importance in the fabrication of p-i-n diodes by the lithium drift method, that special effort must be taken to correct for imperfect compensation of acceptors due to the space-charge generated current.

CHAPTER II

CHARACTERISTICS of p-i-n DETECTORS

2. One of the most important characteristics of lithium-drifted germanium or Ge(Li) detectors for gamma-ray spectroscopy is their excellent energy resolution. (The terms "resolution," "peak-width," and "line-width" as used herein refer to the full width at half the maximum height, FWHM, in keV of a gamma-ray peak in a pulse-height spectrum.) The radiation detection process in solid-state detectors is essentially two-staged: firstly, radiation interacts in a characteristic way with the detector material to produce free charge carriers, and secondly, the charge must be collected, i.e., swept out of the crystal for measurement by the external electronic equipment. Both the charge production and collection processes are subject to fluctuations which can broaden the line-width; other detector characteristics such as excess leakage current which do not affect the charge processes directly can also degrade the energy resolution through noise contributions.

Thus the factors which result in less than optimum resolution for Ge(Li) detectors can be discussed in terms of three general categories: charge production, charge collection, and noise effects. Factors which affect the first topic, charge production, are functions only of the detector material, and the nature and energy of the incident radiation, and cannot be manipulated. The latter two topics can be dependent upon fabrication technique, amd some improvement in charge collection and noise can be achieved by proper treatment of the detector.

2.1 Production of Charge In discussing radiation-induced ionization in semiconductors, one needs to differentiate between the interactions of gamma-rays and of densely ionizing radiations with the detection medium. A densely ionizing particle is brought to rest within the medium relatively rapidly in 10^{-12} to 10^{-11} seconds, losing almost all its energy in the production of low energy electrons by impact ionization. Gamma-rays produce at each interaction energetic electrons, by processes which will be detailed later, which may then be considered in the same way as a primary bombarding particle, though not originating at the surface of the detector.[31] The secondary electrons, in turn, lose their energy very rapidly by further impact ionization until they are of insufficient kinetic energy to produce electron-hole pairs.

We now define two quantities used in describing radiation-induced ionization in semiconductors. The radiation-ionization energy ϵ is the average energy given up by the incident radiation in the process of generating a single electron-hole pair.[61] The minimum energy required for pair production by impact ionization of valence electrons in the semiconductor by incident radiation is the ionization threshold energy E_i, and has been shown[24] to be approximately equal to $1.5E_g$ (the band gap) for a variety of elemental and compound semiconductors.

Klein[61] in deriving the relationship between band gap and radiation-ionization energy develops a qualitative picture of the various loss processes in ionization induced by radiation in semiconductors. The basis for the phenomenological approach is the treatment of each electron-hole pair as the result of some "elementary process" which does not involve the actual physics of the interaction between the medium and radiation. The

average energy for producing an electron-hole pair can be written as

$$\varepsilon = E_g + \langle W_L \rangle \tag{2-1}$$

where $\langle W_L \rangle$ represents energy spent for purposes other than ionization, i.e., lost to the lattice. Data on yield of pairs, which will be discussed later, indicate that these losses play a considerable role, and thus the process of phonon generation in the solid in the course of pair production and thermalization must be accounted for in accordance with the data.

Klein's model[61] considers loss phenomena to occur in two consecutive steps: firstly, the kinetic energy released into the system creates a non-equilibrium distribution of mobile carriers by inducing transitions from the valence band into the conduction band; this phase is completed almost instantaneously although it is probable that impact ionization competes with phonon generation. The second phase involves the thermalization, or transferring of excess kinetic energy to the lattice, a process which develops essentially after termination of the carrier generation-multiplication "cascade."[94] Figure 10 is intended to be a schematic representation of the relevant events. The loss term $\langle W_L \rangle$ includes a contribution due to "optical" phonons in addition to one due to thermalization losses:

$$\langle W_L \rangle = \langle E_R \rangle + \langle E_K \rangle \tag{2-2}$$

where the phonon loss term $\langle E_R \rangle$ reflects the observation[61] that charge carriers of pair-producing impacts are coupled to optical modes and may emit Raman phonons. Thermalization losses $\langle E_K \rangle$ arise from the fact that the culmination of the energy loss process in solids is the production of secondaries incapable of producing further ionization, and thus must convert

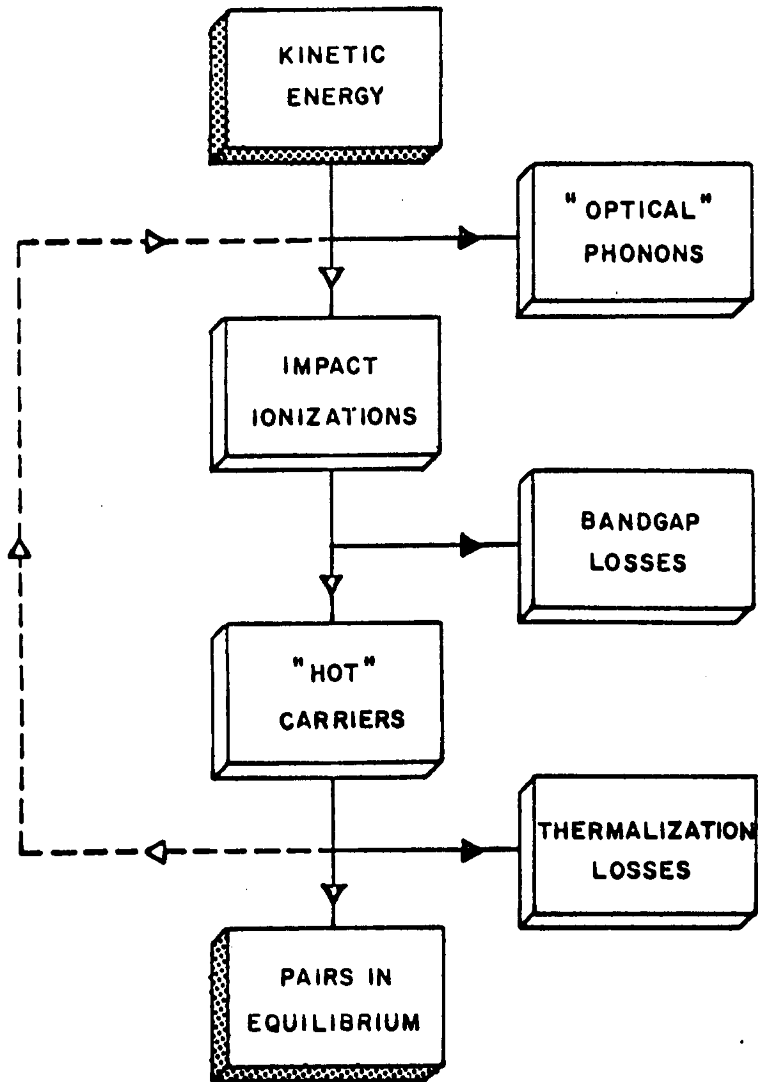

FIGURE 10: ENERGY LOSS PROCESSES IN RADIATION-INDUCED IONIZATION IN SEMICONDUCTORS.

their residual energy into lattice vibrations.

2.1.1 Interaction of Gamma-rays with Matter[28,54] We now wish to outline the three major interactions of gamma-rays with matter which produce the primary ionizing particles. The processes with which we shall be concerned are the photoelectric effect, Compton scattering, and positron-electron pair production.

a) Photoelectric effect: In this type of interaction, the incident photon causes an electron to be ejected from one of the atomic shells, the K-shell contributing most since absorption increases with increasing electron binding. The energy of the ejected photoelectron E_e is given by

$$E_e = E_\gamma - E_b \tag{2-3}$$

where E_γ is the energy of the incident photon and E_b the binding energy of the electron. From Figure 11, in which the mass attenuation coefficients[20] of germanium for the three major gamma-ray interactions are plotted vs gamma-ray energy, it can be seen that below about 0.15 MeV, the photoelectric interaction is dominant. For a constant Z, the angle of emission of a photoelectron shifts to the forward direction with increasing gamma-ray energy, e.g., the half-angle of the cone within which one-half of all the photoelectrons appear (the bipartition angle) varies from 90° for the limiting case of $E_\gamma = 0$ to 10° for $E_\gamma = 6$ MeV.[54]

b) Compton scattering: This interaction is generally defined[54] as the inelastic incoherent scattering of photons by atomic electrons. The process results in a scattered photon of energy E'_γ at an angle θ to the incident photon and an electron of energy E_e at an angle of φ. The kinetic energies of the Compton scattered photon and electron are

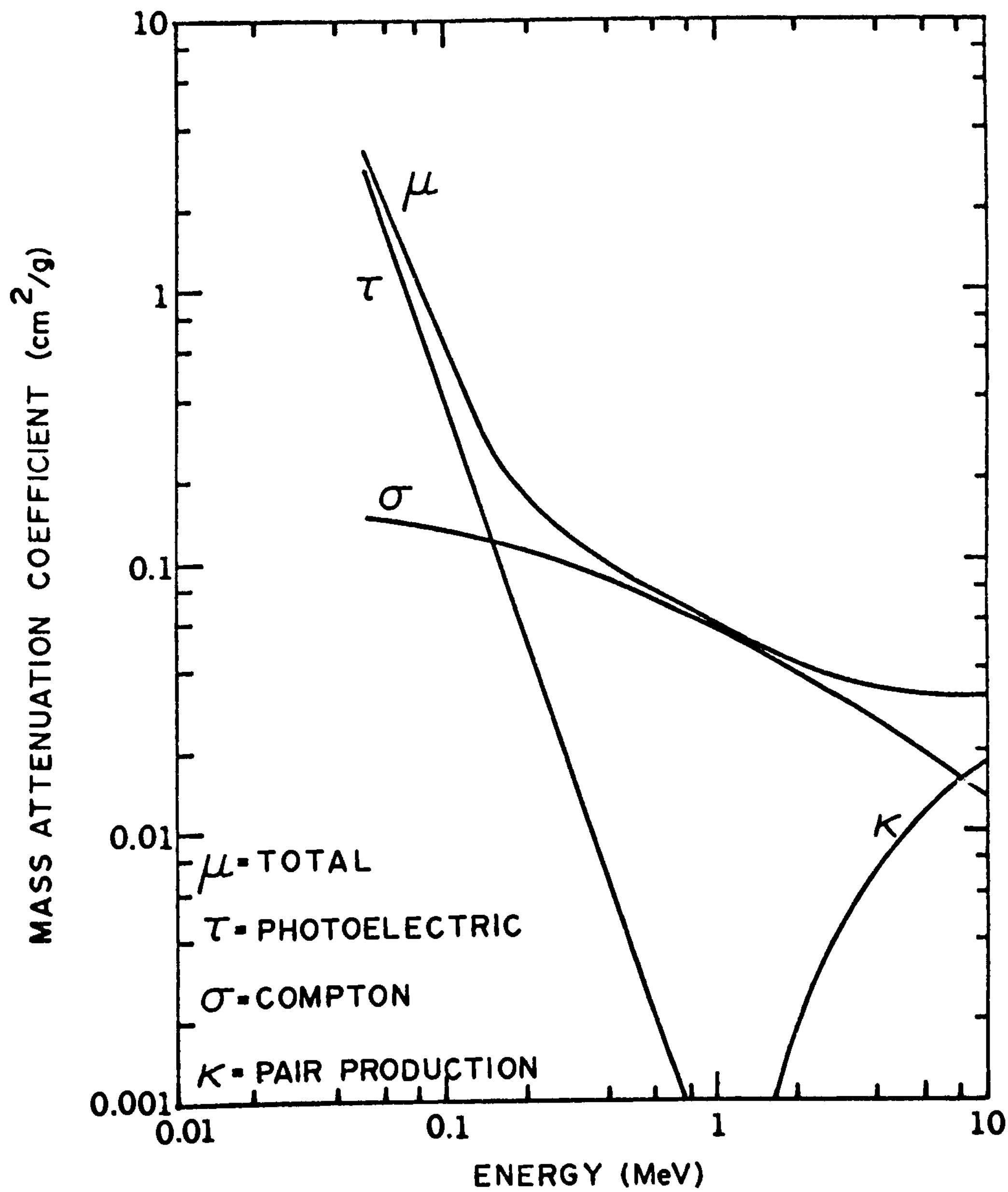

FIGURE 11: GAMMA-RAY MASS ATTENUATION COEFFICIENTS FOR GERMANIUM

dependent on the scattering angle, and are given by the following for the photon and electron, respectively:[54]

$$E'_\gamma = \frac{E_\gamma}{1 + \alpha\,(1 - \cos\theta)} \tag{2-4}$$

$$E_e = E_\gamma - E'_\gamma = \frac{E_\gamma \alpha\,(1 - \cos\theta)}{1 + \alpha(1 - \cos\theta)} \tag{2-5}$$

where $\alpha = E_\gamma/m_o c^2$. As seen in Figure 11, the Compton interaction is dominant between about 0.15 and 8 MeV.

c) Pair Production: At incident photon energies greater than $2m_o c^2$ = 1.022 MeV, the production of electron-positron pairs can be initiated in the Coulomb field of the nucleus of the absorber. The kinetic energy of the pair $E^{\pm}$ is given by:

$$E^{\pm} = E_\gamma - 2m_o c^2 \tag{2-6}$$

The subsequent annihilation of the positron results in two photons each of energy $m_o c^2 = 0.511$ MeV which may interact further with the atoms in the absorber by processes a) and b) or escape the crystal. Figure 11 shows that the pair production process does not become dominant until photon energies exceed about 8 MeV.

With respect to the radiation-induced ionization process in a solid, the three major interaction processes of gamma-rays with matter result in high energy electrons originating within the solid which may be treated as primary ionizing particles.

2.1.2 Statistics of Charge Production The average energy expended in producing an electron-hole pair ε in germanium is 2.98 eV,[3] and is larger than the forbidden gap energy E_g because, in the impact ionization

process by which the primary energetic electrons lose energy, some energy is lost in heating the crystal lattice. This division of energy between ionization and phonon production results in statistical fluctuations in the number of ion pairs produced by photons of a given energy.

The average number of ion pairs N produced by radiation of energy E is given by

$$N = E/\epsilon \tag{2-7}$$

If each ionization event were independent and N were large, the statistical fluctuation in N would be just $\sqrt{N}$. Fano[41] showed, however, that the ionization events are not completely independent since the primary particle has to lose exactly its initial kinetic energy during the slowing down process. The Fano factor F is thus defined as the ratio of the variance in the yield of ion pairs to that yield:[15,30]

$$F = \sigma_n^{\ 2}/N \tag{2-8}$$

It will also be convenient to define at this time the energy resolution of a semiconductor radiation detector in terms of the following: the energy of radiation which will produce a charge equivalent to the standard deviation is given by[32]

$$\sigma\epsilon\ /e = \sqrt{E\epsilon F} \tag{2-9}$$

and this is related to the energy resolution in keV (FWHM) as obtained from a pulse-height spectrum by

$$\mathrm{FWHM} = 2.355\sqrt{E\epsilon F} \tag{2-10}$$

Thus a knowledge of the magnitude of F in germanium will yield information

as to the ultimate resolution of Ge(Li) detectors. Also any theory which attempts to explain the ionization process in semiconductors must successfully account for the Fano factor, and experimental measurements of F could yield insight into the ionization process.

Bilger and Mann[10] proposed a simple interpretation of the Fano factor in terms of Fano's original statistical theory for gases, assuming that only the final ionization dominates, where an electron jumps from the ground state to some level in a band above the ground state. This yields an estimate of the lower limit of F of approximately 0.04.

There are at present two theories which attempt to explain ionization processes in semiconductors and which take into account the role of phonon losses. The most recent is due to Klein[61] in which a theoretical relationship is derived between the Fano factor F and two dimensionless parameters, Y, the radiation-ionization efficiency, and K, the relative phonon loss, where

$$Y = E_g/\varepsilon \qquad \text{and} \qquad K = \langle E_R \rangle / E_g . \tag{2-11}$$

Evaluating F in terms of Shockley's original pair production model[2,107] Klein obtains the following:

$$F = (K^2 + 0.315)Y^2 \tag{2-12}$$

which shows[61] that residual energy fluctuations control the statistical behavior of $K^2 \leq \sim 0.3$, though Fano factor variations are entirely determined by the relative importance of optical phonon losses. Figure 12 presents Klein's results of the dependence of the ionization efficiency Y and Fano factor F on the relative amount of phonon loss K. For the case of interest, germanium at 77°K, $Y = 0.25$ using equation 2-11 and

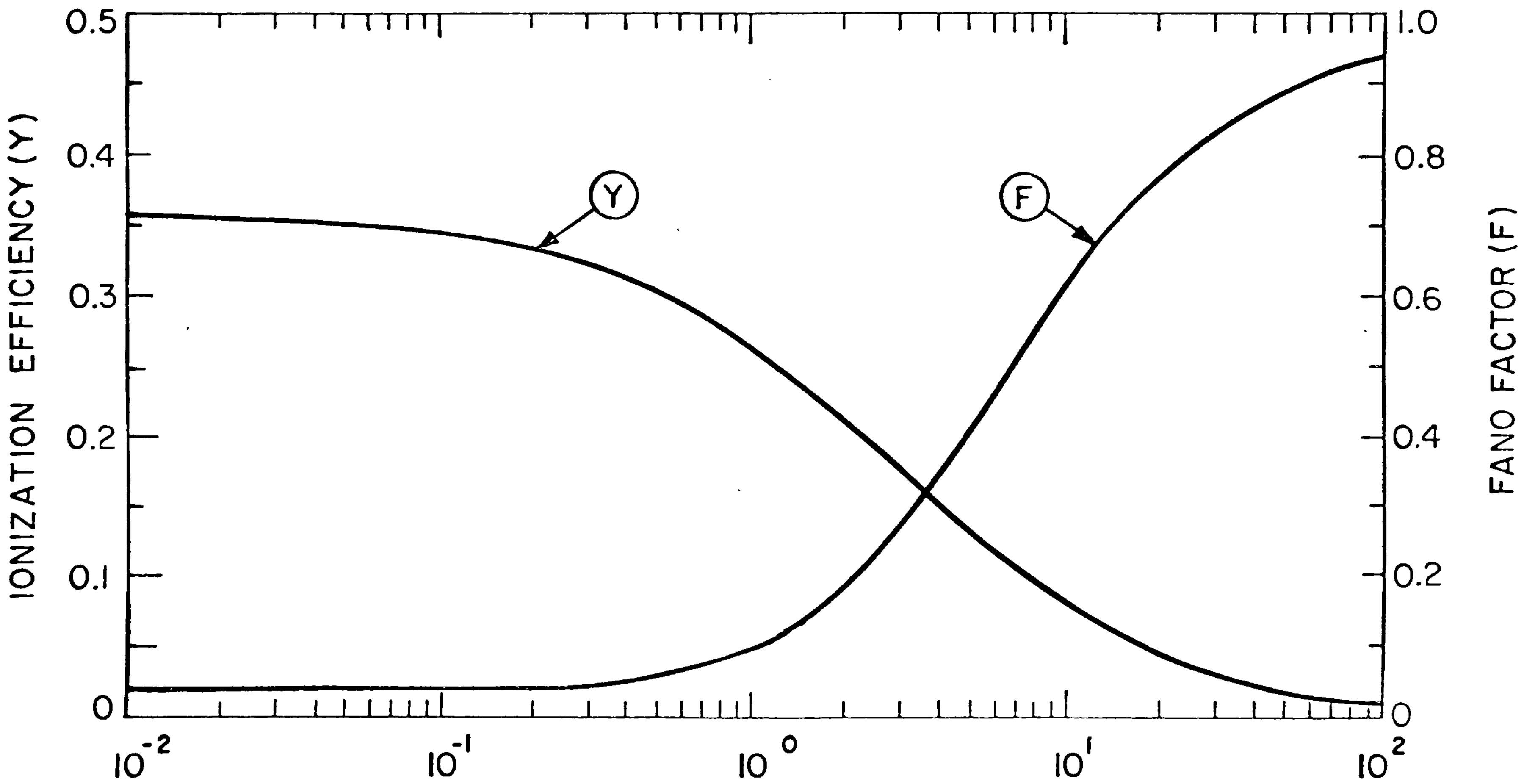

FIGURE 12

$E_g = 0.75$ eV with $\varepsilon = 2.98$ eV. For $Y = 0.25$, Figure 12 yields a theoretical value for F of 0.11.

Van Roosbroeck[123] proposed a statistical model of the ionization process independent of the details of the actual physics involved. The model is described in terms of the "crazy carpentry" problem in which the energy of a primary particle is partitioned in the following manner. Let us visualize that the energy of the incident particle is represented by a board of length L in units of the ionization threshold E_i (see Figure 13). A small piece is cut off the right-hand end with probability r, representing the generation of an optical phonon. Length unity (E_i) is removed from the right-hand end with probability 1-r representing yield of a secondary, and a random cut is made (at x). The right hand portion, the secondary remainder, represents the energy of the secondary, and in the simplest assumption, is divided in equal portions representing equal energies for the secondary electron and hole. These two portions as well as the part labelled "primary remainder" are again subjected to the partitioning process as above as long as lengths greater that E_i are available. Portions of secondary remainders which are of length less that E_i thus represent secondaries incapable of producing further ionization. For particles of large incident energy (length L), this waste is negligible in the initial stages and becomes appreciable only when the remainders are only a few units of E_i in length. It is this constraint at the end of the ionization process, where many secondaries are produced which cannot initiate further ionization, which largely determines the Fano factor.

Van Roosbroeck defines the following terms (upon which Klein's were based) for efficiency and phonon loss, respectively:

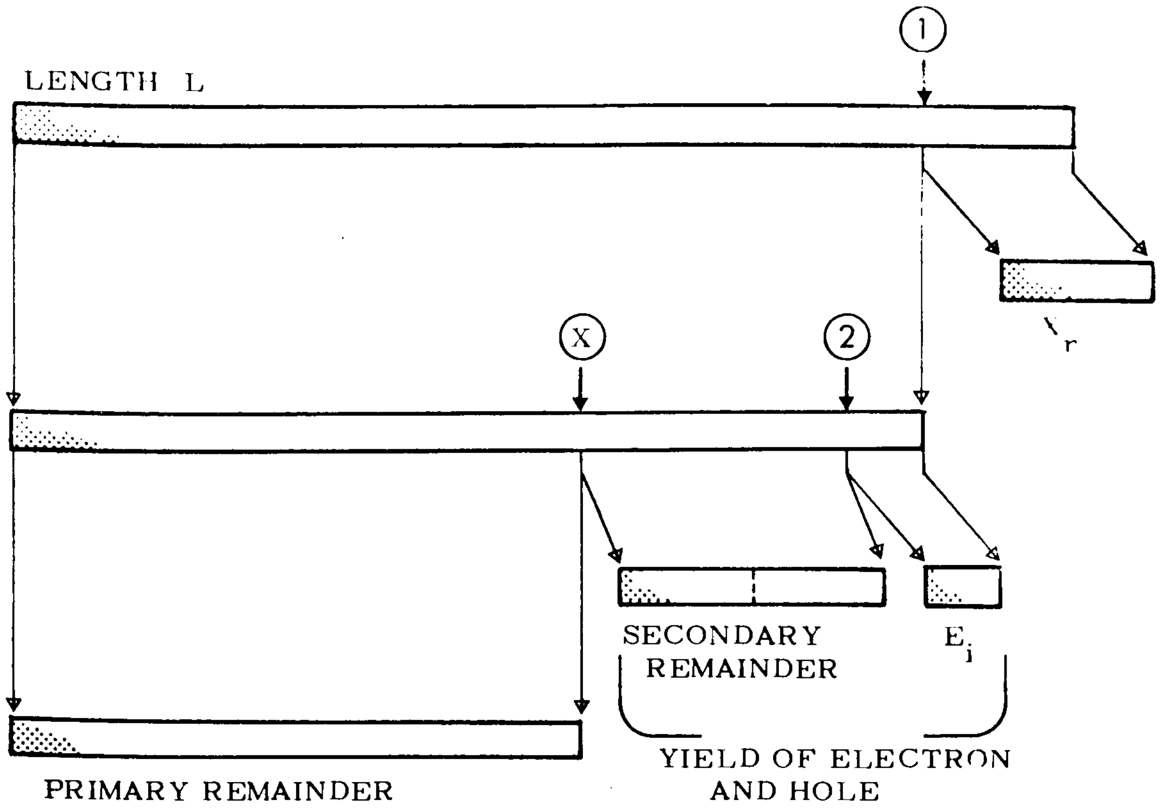

FIGURE 13: "CRAZY CARPENTRY" APPLIED TO ENERGY LOSS PROCESSES IN RADIATION-INDUCED IONIZATION IN SEMICONDUCTORS.

$$Y = E_i/\varepsilon \qquad \text{and} \qquad K = NE_R/E_i \tag{2-13}$$

For germanium at 77^oK, a value of $F = 0.32$ is obtained. It should be noted that the crazy carpentry model[123] requires $E_i = E_g$ rather than the experimentally accepted $E_i = 1.5E_g$.[24] Thus the crazy carpentry model would seem to be less acceptable than the model proposed by Klein.[61]

2.2 Effects of Charge Collection The adverse effects of incomplete charge collection on semiconductor detector resolution can be examined by considering two factors, carrier recombination and trapping. We can define trapping[118] as the removal of a carrier from its condition of mobility to a localized level within the band gap, such a level being termed a "trap" regardless of its other possible functions, e.g., as a donor or acceptor. At equilibrium, the trapping rate for each type of carrier is equal to a "release rate." Within the above definition, the recombination-generation process at localized levels might also be termed trapping. The direct recombination-generation process, i.e., directly between the valence and conduction bands, is of negligible importance in impure semiconductors.[118]

2.2.1 Plasma Recombination For densely ionizing radiations, charge carriers may be lost through direct electron-hole recombination in the plasma surrounding the ionization track, especially if there is insufficient collection field to rapidly separate the carriers. For gamma-rays, which are not ionizing like charged particles, plasma recombination has been found to be insignificant in semiconductor detectors under normal operating conditions.[81,82]

2.2.2 Carrier Trapping The problem of charge carrier trapping and its effects on detector resolution has been described by Day, et.al.,[29] for a

planar p-i-n detector. For an electrode separation w, a uniform electric field $E = V/w$, and assuming uniform charge production throughout the volume of the detector by gamma-rays, it is shown that the total charge pulse due to electrons is:

$$\bar{q}_n = N_o e(\lambda_n/w - \lambda_n^2/w^2 + \lambda_n^2/w^2 \, e^{-w/\lambda_n}) \qquad (2\text{-}14)$$

where N_o is the average number of electrons produced in the detector by a gamma-ray, e is the electron charge, and λ_n is the drift length of an electron before trapping, defined[23] as:

$$\lambda_n = \mu_n \tau E \qquad (2\text{-}15)$$

where μ_n is the electron mobility, τ is the electron lifetime, and E is the electric field.

By symmetry, Day, et.al.,[29] show that the pulse due to the collection of both electrons and holes is:

$$\bar{q} = N_o e/w^2[(\lambda_n + \lambda_p)w - (\lambda_n^2 + \lambda_p^2) + \lambda_n^2 e^{-w/\lambda_n} + \lambda_p^2 e^{-w/\lambda_p}] \qquad (2\text{-}16)$$

Assuming $\lambda_n = \lambda_p = \lambda$, equation 2-16 becomes:

$$\bar{q} = 2N_o e(\lambda/w)^2(w/\lambda - 1 + e^{-w/\lambda}) \qquad (2\text{-}17)$$

which shows the dependence of $\bar{q}$ (hence η) on λ (see Fig. 14).

The charge collection efficiency η can be thus defined as the ratio of the charge collected in the external circuit $\bar{q}$ to the charge liberated in the detector $N_o e$:

$$\eta = \bar{q}/N_o e \qquad (2\text{-}18)$$

Equation 2-17 can then be written in terms of η by substitution of equation 2-18 into 2-17:

$$\eta = 2(\lambda/w)^2(w/\lambda - 1 + e^{-w/\lambda}) \tag{2-19}$$

It can be seen that in order to maximize charge collection, λ should be much greater than w, i.e., the average distance a carrier traverses before being trapped should greatly exceed the distance between the detector electrodes if the charge is to be collected completely. For the case of interest, $\lambda > w$, the exponential term in equation 2-19 can be expanded, and the collection efficiency becomes

$$\eta \approx 1 - w/3\lambda \tag{2-20}$$

Figure 14 shows the calculated effect on η by variation of the trapping length parameter λ/w.[29] If the carrier trapping length is an order of magnitude greater than the compensated thickness w of the detector, η will be greater than 0.97.

For gamma-rays impinging on p-i-n detectors, incomplete charge collection can cause line broadening in two ways. One is that carrier drift lengths may fluctuate about a mean, and the other is collection of carriers traversing different distances in the sensitive volume of the detector. The greatest fluctuation occurs when ion pairs are created at randomly distributed positions.[29,32]

The first factor, fluctuation of carrier drift lengths, has been shown to be negligible[88] since in all detectors of practical interest $(\lambda >> w)$, almost all carriers reach the electrodes. The second, geometrical factor, is important; the standard deviation σ in pulse height due to this effect is:[32]

$$\sigma^2 = \overline{q^2} - (\overline{q})^2 \tag{2-21}$$

$$= 1/w \int_0^w (q_n + q_p)^2 dx - (\overline{q})^2$$

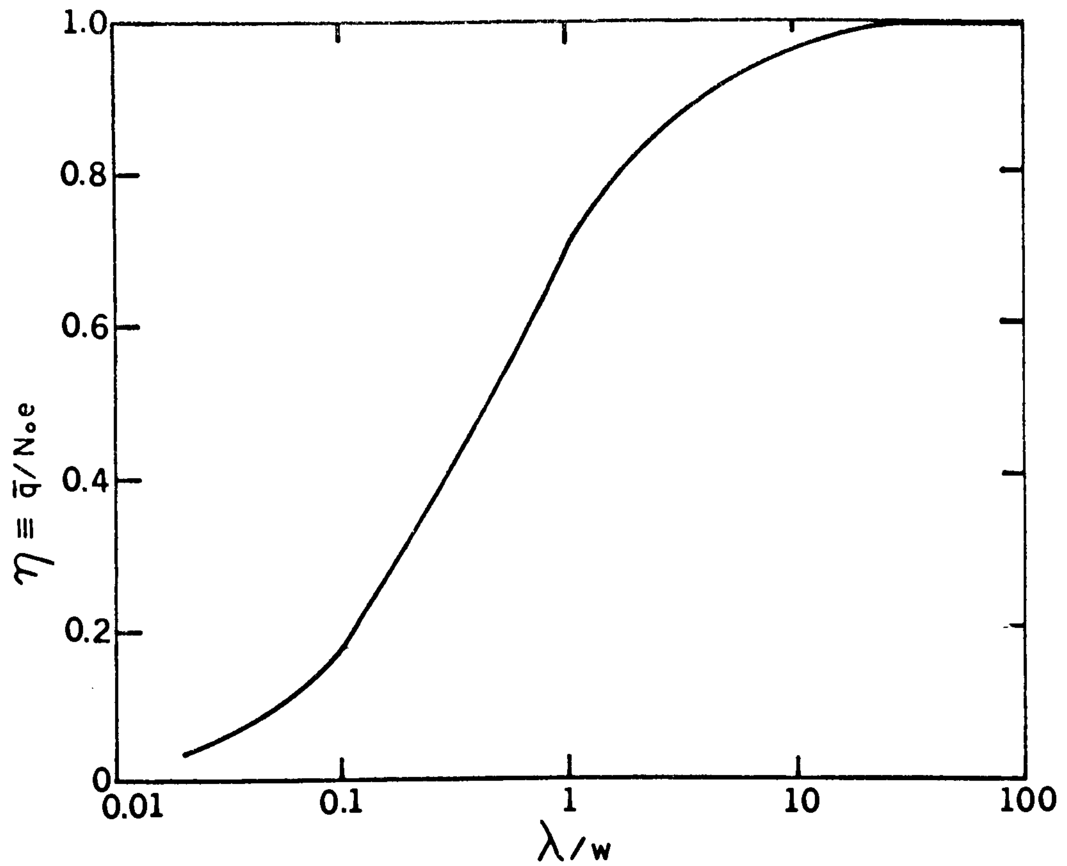

FIGURE 14: CHARGE COLLECTION EFFICIENCY η vs DRIFT-LENGTH PARAMETER λ /w.

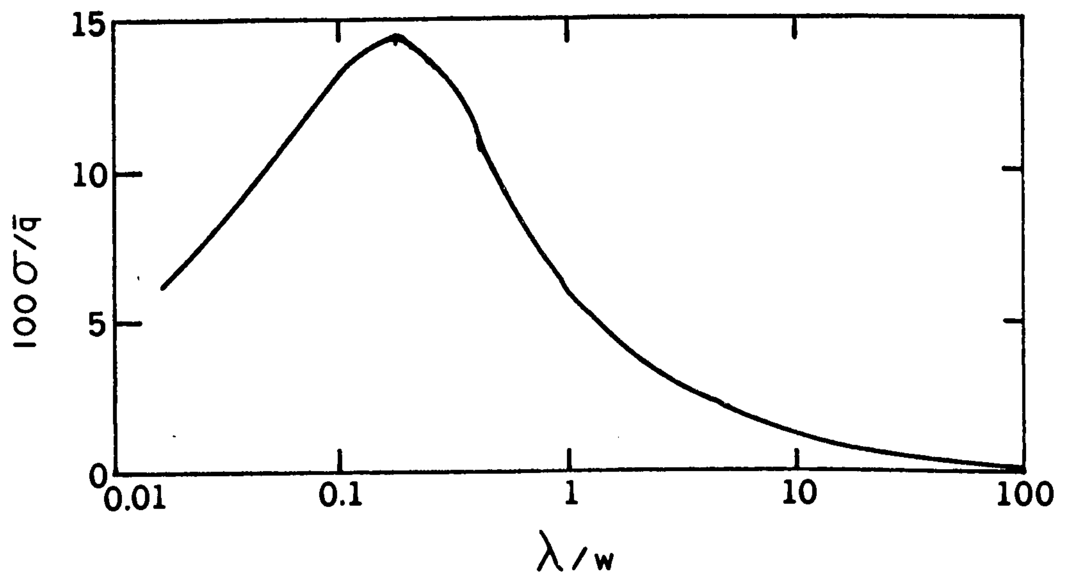

FIGURE 15: PERCENT RESOLUTION $100\sigma/q$ vs

where q_n and q_p represent the charge due to electrons and holes, respectively. Day, et. al.,[29] have computed values of σ over ranges of λ_n and λ_p, the minimum values of σ being found to occur near $\lambda_n = \lambda_p$ as is expected on grounds of symmetry. Figure 15 shows the results plotted in terms of the percent resolution $100\sigma/\overline{q}$ vs λ/w for $\lambda_n = \lambda_p$. As λ becomes small, the results will approximate the condition where no carriers reach the electrodes, and where $\sigma = \sqrt{\overline{N}_o}$.

2.3 Detector Noise The third factor affecting detector resolution aside from the statistical effects of charge production and collection, is the electrical noise generated in the detector. The sources of this noise are bulk leakage current, charge injection from non-ohmic contacts, and surface leakage currents. Of these three general sources of electronic noise, the excess current generated through detector surface imperfections are the most common and troublesome; however, the chemical state of the exposed semiconductor surface formed during final fabrication steps is amenable to various surface treatments which lower excess current with varying degrees of success. We can thus examine sources of electrical noise in p-i-n detectors with particular attention to those sources which can be minimized in some way in order to obtain optimum detector performance.

2.3.1 Bulk Generated Leakage Current Electrical noise generated within the bulk of a semiconductor detector arises fundamentally because the crystal is not a perfect dielectric and contains charge carriers in thermal equilibrium with the lattice. This type of noise may be classified into two categories:[29,32] thermal noise and current noise.

a) Thermal Noise: A convenient quantity for measuring the thermal

noise contribution is the energy W_p of a particle necessary to produce a signal equivalent to the voltage fluctuation at the detector electrodes due to the thermal current:[32]

$$W_p = (\epsilon/e)(kTC)^{\frac{1}{2}} \quad \text{keV} \tag{2-22}$$

where T is the absolute temperature and C is the detector capacitance in picofarads (pf). For a Ge(Li) detector operating at 77°K and $\epsilon = 2.98$ eV,

$$W_p = 0.6C^{\frac{1}{2}} \tag{2-23}$$

Thus for a typical detector capacitance $C = 10$ pf, $W_p = 1.8$ keV. The detector line width resulting from a particle of energy 1.8 keV is approximately 0.17 keV (FWHM) using equation 2-10 and the maximum value for the Fano factor, F = 1. Generally, then, the thermal noise contribution to line width for cooled Ge(Li) detectors is negligible for common values of detector capacitance, being less than the noise contribution of the best preamplifiers in use at present.

b) Current noise: When an electric field is applied to a detector, additional sources of noise arise; the resulting current is made up of discrete movements of charge carriers which may be trapped or thermally generated within the crystal. Any process which interrupts the movement of the electrons and holes introduces statistical fluctuations in the detector leakage current, and can contribute measurably to line width.[29,32] Two components of current noise are "shot noise" which is introduced because of the lack of correlation between carriers traversing the same path in an electric field, and "generation-recombination noise" which arises through the random breaking-up of individual carrier trajectories into separate parts due to trapping and release.

Northrop and Simpson[88] have shown that the standard deviation in line

width ΔW due to these related phenomena is of the order

$$\Delta W \approx \varepsilon (N_c/2)^{\frac{1}{2}} (t_c/t_r)^{\frac{1}{2}} \qquad (2-4)$$

where N_c is the total number of charge carriers within the sensitive volume of the detector, t_c is the amplifier time constant, and t_r is the carrier transit time, i.e., the time required for a carrier to traverse the distance between the region where it originates and an electrode. For a typical planar Ge(Li) detector of 2 cm^3 sensitive volume operating at 77°K, $\Delta W \approx 300$ eV, for $N_c \approx 5 \times 10^2$ (assuming a reverse current of 10^{-9} amps), $t_r = 3 \times 10^{-8}$ sec, and $t_c = 10^{-6}$ sec.[29] This corresponds to a FWHM, resolution contribution of 2.355×0.3 keV or approximately 0.7 keV FWHM, which would just about be measurable with some of the field-effect transistor (FET) preamplifiers currently in use. If the reverse current were 10^{-8} amps, the noise contribution would be almost 2 keV FWHM[29] thus leakage currents on the order of 10^{-9} amps or less must be achieved if the detector noise due to current sources does not dominate other contributions.

2.3.2 <u>Noise Due to Poor Electrical Contacts</u> The electrical contacts made to the n- and p-sides of a p-i-n detector must be ohmic, i.e., there must be no potential drop across the junction of the electrode and the semiconductor surface, and the concentration of charge carriers must not be modified anywhere in the detector due to the electrodes under the application of an electric field.[32] Most metals will form with n-type germanium contacts which are rectifying, the only known exception being antimony.[49] The gold-n-type silicon or germanium surface barrier detector which has the same characteristics as a p-n junction, is an example of a device in which a metal rectifying contact is desirable. If however, such a junction

were to be formed on the n-side of a p-i-n detector yielding a p-i-n-p configuration, reverse-biasing of the device would result in injection of charge in the forward biased metal-n-type germanium junction. The affects of excess current were discussed in the preceeding section; however, degradation of resolution due to poor contacts is rarely encountered in Ge(Li) detector fabrication if the n- and p- surfaces are degenerate, i.e. of very high conductivity. The procedure used[49] is to diffuse into the n- and p- type surfaces lithium and a suitable acceptor impurity, respectively, and lap or etch the surface until very low resistivities are obtained. Thus there is obtained a graded transistion between the metal contact and high resistivity compensated region of the device which permits the intro-duction and withdrawal of a continuous flow of current. The configuration of such a device could be termed p^{+}-p-i-n-n^{+}.

2.3.3 Surface Generated Noise A third and apparently major source of noise in Ge(Li) detectors is the so-called "excess" noise associated with the final chemical treatment of the crystal surface. The surface of a finite semiconductor crystal represents an abrupt termination of the periodicity of the crystal lattice. The different environment of the topmost atomic layers as compared to that of the layers in the bulk usually gives rise to a re-arrangement of the surface atoms. The special position of such outer atoms and the unsaturated bonds associated with them promote a strong interaction with various species in the surrounding media.

The most important effect of the lattice discontinuity on the electrical processes at the surface arises from the presence of "surface states" and their interaction with an underlying space-charge region. In contrast to the situation in the bulk where a valence electron belongs to the entire

crystal, "surface states" can appear at the surface where an electron may be localized in an atomic layer.[78]

In the absence of surface states, the energy bands of a semiconductor continue straight up to the surface provided there is no external field. When, for example, acceptor-like surface states are introduced below the Fermi level, they will not be in equilibrium with the energy bands as long as they remain unoccupied.[77] This situation is illustrated in Figure 16(a) where acceptor-like surface states have been introduced at an energy level E_t in an n-type semiconductor. Since these states are empty and below the Fermi level E_f, some of the electrons in the conduction band fall into them. In this process, the surface becomes negatively charged while a positive space-charge layer forms below it. Consequently, the energy bands at the surface bend upwards with respect to the Fermi level. The process of charge transfer continues until equilibrium is reached, as shown in Figure 16(b). In the particular case shown, the surface states at thermal equilibrium are somewhat above the Fermi level and so are only partially filled. The actual position of the surface states with respect to the Fermi level is determined by the condition that the positive charge in the space-charge region just balances the negative equilibrium charge in the surface states.[77] Thus the larger the surface state density, the higher the bending of the bands at the surface. The situation for donor-like surface states placed above the Fermi level is completely analogous.

Once a space-charge region exists at the surface in a given semiconductor, its characteristics are uniquely determined by the height of the potential barrier at the surface proper.[77] The potential Φ is defined by the equation:

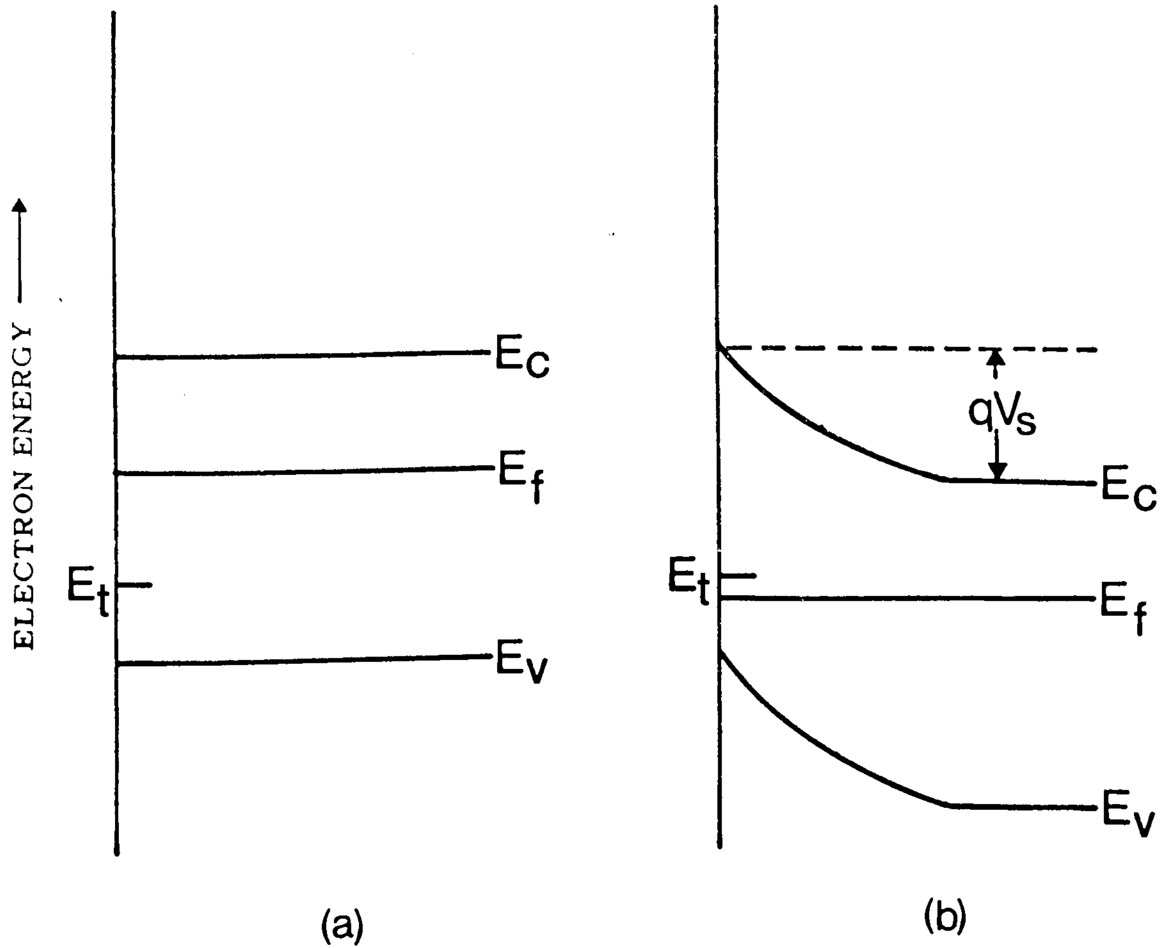

FIGURE 16: ENERGY LEVEL DIAGRAM FOR AN n-TYPE SEMICONDUCTOR WITH ~~DONOR~~-LIKE SURFACE STATES, (a) IMMEDIATELY AFTER INTRODUCTION OF THE SURFACE STATES, AND (b) AFTER THERMAL EQUILIBRIUM HAS BEEN REACHED.

$$q\Phi = E_f - E_i \tag{2-25}$$

where E_i is parallel to the valence and conduction band edges and in the bulk coincides with the intrinsic Fermi level (Figure 17). The value of Φ in the bulk is called the bulk potential Φ_b and its value at the surface, the surface potential Φ_s.[59] The potential barrier V is defined as:

$$V = \Phi - \Phi_b \tag{2-26}$$

and represents the potential at any point in the space-charge region with respect to its value in the bulk. In particular the barrier height $V_s = \Phi_s - \Phi_b$ is the total potential difference between the surface and the bulk.[77] When the majority carrier density in the space-charge region is greater than in the bulk, the space-charge region is termed an accumulation layer, $V_s = \Phi_s - \Phi_b < 0$; when $V_s = \Phi_s - \Phi_b > 0$, we have an inversion layer. Figure 17(a) illustrates the various parameters used to characterize the space-charge region for a p-type semiconductor with an accumulation layer, and in (b), with an inversion layer.

In studies on thick p-i-n silicon detectors, Llacer[70,71] and Monteith[86] found that the leakage current due to surface effects results in two main sources of noise: a) surface generation of carriers with characteristics similar to shot noise, and b) surface breakdown which has its onset at higher biases than source a). Llacer[70,71] has proposed a model for the origin of leakage current due to surface generation in silicon p-i-n diodes in which an n-type surface inversion layer extends from the boundary of the n-region in the bulk across the surface of the i-region to the boundary of the p-region of the bulk. The highest fields between the surface and the bulk are at the junction of the n-type inversion layer and p-type bulk

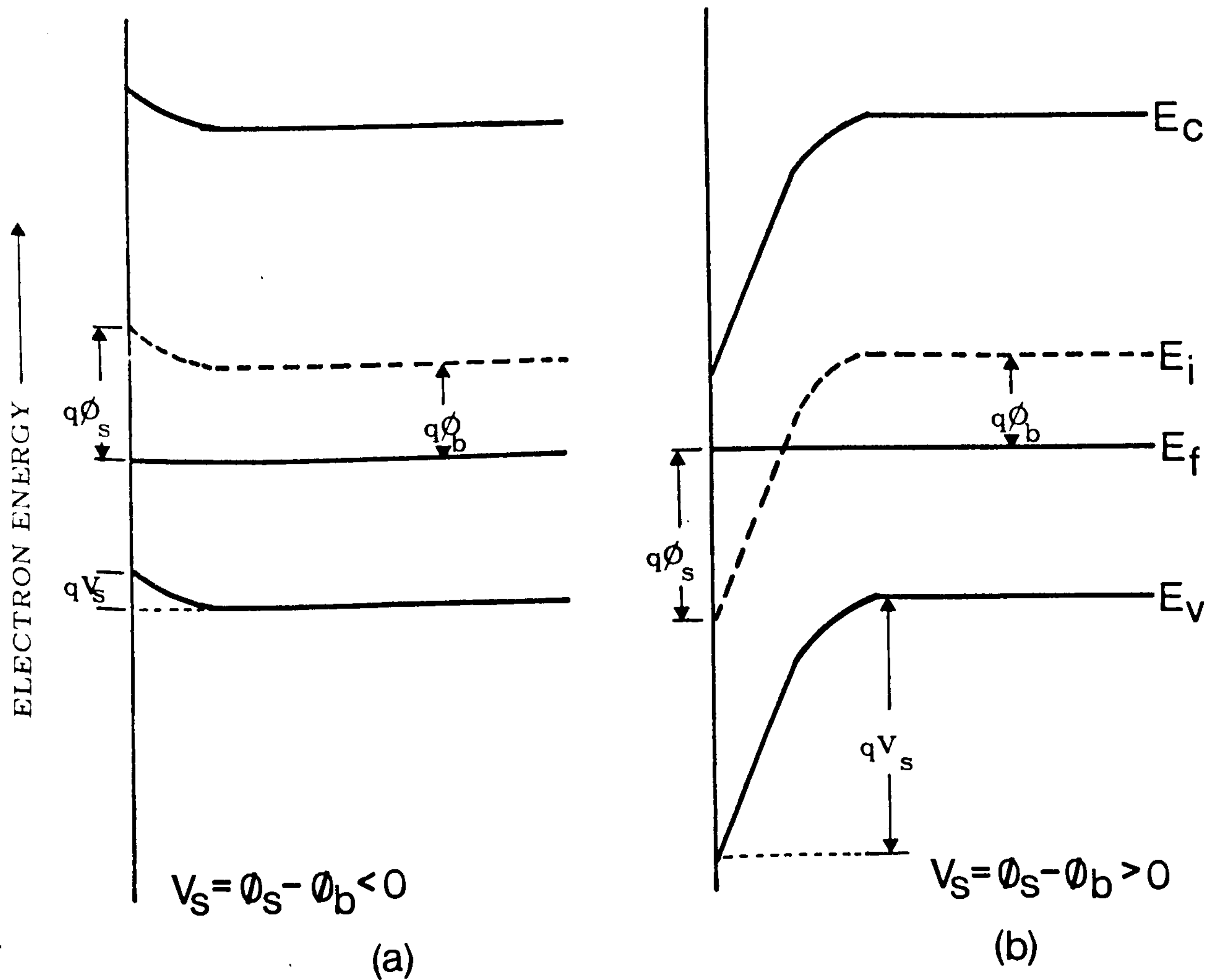

FIGURE 17: ENERGY LEVEL DIAGRAM INDICATING THE VARIOUS ENERGY PARAMETERS USED TO CHARACTERIZE THE SPACE-CHARGE REGION FOR A p-TYPE SEMICONDUCTOR WITH (a) AN ACCUMULATION LAYER, AND (b) AN INVERSION LAYER.

material. This may be illustrated schematically in Figure 18, in which a plot of potential vs distance through the bulk of a p-i-n diode is shown. The dotted lines plot the surface potential vs distance when the n-type surface inversion layer exists; the large potential drop near the surface of the p-region is shown and is expected to result in low breakdown voltage.[70,71]

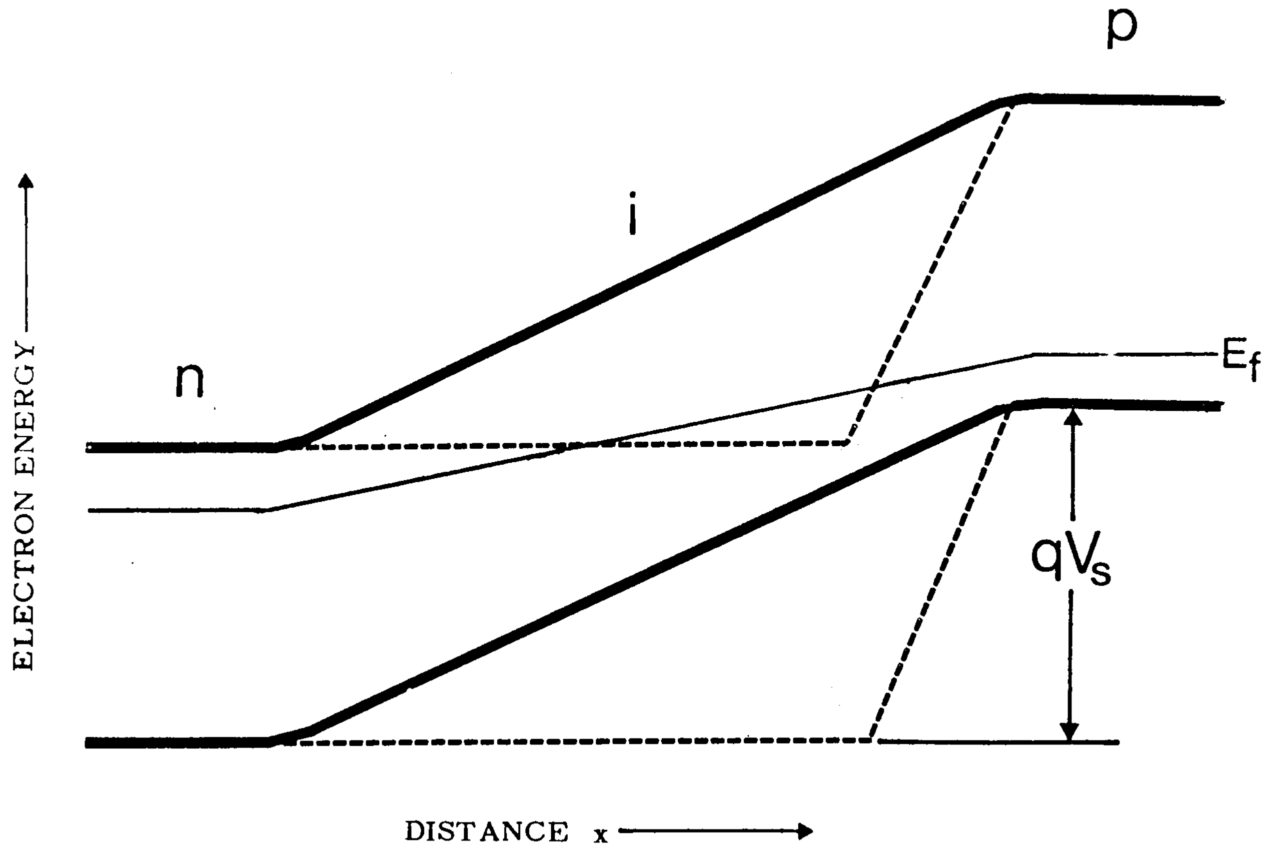

FIGURE 18: ELECTRON ENERGY vs DISTANCE x THROUGH A p-i-n JUNCTION DEVICE. DASHED LINES REPRESENT THE ELECTRON POTENTIAL AT THE SURFACE DUE TO THE PRESENCE OF AN n-TYPE INVERSION LAYER.

Part Two

Fabrication of Lithium-Drifted Germanium Radiation Detectors: Experiment

CHAPTER III

EXPERIMENTAL TECHNIQUE

3. During the course of the present work, planar Ge(Li) detectors of from less than 1 cm^3 to 8 cm^3 in active volume were fabricated. Two fabrication techniques have been used which differed essentially in the lithium-drifting procedure: small-volume devices were made using a process based upon the method outlined by Tavendale[103,114] and large-volume (totally compensated) detectors were fabricated using the AC-drift method of Jamini.[56]

Germanium ingots from two suppliers, Sylvania[112] and Hoboken[52] were used, and the following table lists the specifications of each ingot (as supplied by the manufacturer).

TABLE II: Specifications of p-type Germanium Ingots

Ingot	Sylvania #597G-6	Sylvania #564G-1	Hoboken #71D
Type	Horizontal Ga	Horizontal Ga	Vertical In
Cross-section	3.5 x 2.5 cm	3.5 x 2.5 cm	3.5 - 4 cm diam.
Resistivity	11 - 16.5 Ω-cm	12.9 - 15.5 Ω-cm	35 - 37Ω -cm
Dislocations	1600-1900/cm^2	2100-2200/cm^2	800/cm^2
Lifetime	100 μsec	100 μsec	650μ sec
Orientation	(111)	(111)	(111) $\pm$ 51'
Date of Purchase	8/65	8/65	5/67

In this chapter, the Ge(Li) detector fabrication process based on Tavendale's DC-drift procedure[103,114] will be detailed, followed by a description of the AC-drift method[56] where it differs from the former process.

3.1 DC-Drift The name of this procedure is derived from the use of a DC electric field to cause thermally diffused lithium atoms to drift, in a controlled manner, into the bulk of the germanium crystal as lithium ions. In the present work, lithium diffused into one face of a germanium crystal was drifted towards the opposite face for a certain distance so that a planar device resulted having the required p-i-n configuration: an n-type region due to the presence of excess lithium (donor) atoms, an "intrinsic" region where lithium donors have compensated the acceptor impurities, and a p-type region (the original p-type material). It is also possible to fabricate so-called "coaxial" Ge(Li) detectors in which lithium is drifted from the entire outer surface of a cylindrical crystal towards the center, leaving a core of original p-type material surrounded by a cylinder of compensated material and an outer layer of n-type germanium; this detector configuration was not investigated in the present work and will not be discussed further.

3.1.1 Sawing and Lapping The germanium ingot as received from the supplier was mounted on an unglazed porcelain plate with a cement consisting of equal parts by weight of rosin and beeswax, heated to a syrupy consistency. When cooled to room temperature, the cement provided a firm yet slightly flexible bond between the ingot and mounting plate.

The ingot and mounting plate were clamped tightly in a vise which was magnetically held on the bed of a grinding machine upon which the diamond cutting-wheel[89] was mounted. Slices of germanium of the required

thickness were cut from the single-crystal ingot with the diamond wheel rotating at approximately 3500 rpm; cuts of approximately 0.002-0.005" in depth were made at a single passage of the cutting wheel to lessen the chance of mechanical damage to the crystal. After cutting, the germanium slices were removed from the mounting plate by heating the cement until the slices could be pulled free. Excess cement was removed from the crystal with a razor blade.

In order to remove saw marks and other imperfections, the germanium crystal was lapped using a thin paste of #600 grit silicon carbide in water on a flat glass plate. A minimum amount of pressure was used on the crystal during lapping to insure a flat, even finish. Abrasive residue and germanium particles were removed from the crystal by washing in de-ionized, distilled water with ultrasonic agitation and decantation.

3.1.2 Lithium Diffusion A thin coating of a lithium-in-oil suspension[69] was applied to one face of the crystal which was then heated under an argon atmosphere to 250°C for approximately 20 minutes in order to remove the oil. The temperature was then raised to 400°C for 10 minutes resulting in a thermal diffusion of lithium atoms into the germanium to a depth of several hundred microns. The crystal was then cooled fairly rapidly (over a period of 1 - 2 hours), under argon, in order to minimize the reprecipitation of the dissolved lithium.

In the absence of acceptor impurities, lithium has a maximum solubility in germanium of $6.6 \times 10^{13}/cm^3$ at 300°K.[96] The presence of acceptors increases the room temperature solubility, due to ion pairing; however, the relationship between acceptor concentration and lithium solubility is such that it is impossible to permanently maintain enough ionized

lithium in the lattice to convert the germanium to n-type under equilibrium conditions at room temperature unless the acceptor concentration is less than about $5 \times 10^{14}/cm^3$.[49] It is, of course, possible for germanium to be supersaturated with lithium and remain n-type for fairly long periods of time even in the presence of large acceptor concentrations.[49] The time-constant associated with precipitation of super-saturated lithium in germanium is influenced by the degree of super-saturation, the time and temperature of saturation, and by the presence of certain impurities. Carter and Swalin[18] have shown that oxygen and lattice defects will accelerate lithium precipitation, while copper will retard it. They have also shown that copper (an interstitial impurity in germanium) will precipitate more readily in traps than will lithium, in effect lowering the cross-section of a trap for lithium precipitation. Thus a preliminary diffusion of copper has been suggested by some workers[18,51] to minimize precipitation effects in fabricating Ge(Li) detectors. The germanium used in the present work which had the lowest resistivity (i.e., the maximum acceptor concentration) of the three samples was Sylvania ingot #597G-6, 11-16.5Ω-cm. From available data on acceptor impurity concentration as a function of resistivity in germanium,[26,124] the acceptor concentration for a sample of 11 Ω-cm is approximately $3 \times 10^{14}/cm^3$. Thus one would not expect lithium precipitation to be a major problem in the samples used in the present work, since this concentration is below the $5 \times 10^{14}/cm^3$ limit discussed above. This probably explains the result we have obtained, in agreement with others[17,51] that a diffusion of copper prior to the lithium diffusion made no noticable difference in ease of detector fabrication.

After the crystal was at room temperature, the excess lithium still remaining on its surface was removed in 95% ethanol. The edges were

lapped to remove any lithium which might have run onto an edge during the diffusion process; the faces were also lightly lapped. Electroless nickel contacts were then applied to the crystal using the method of Sullivan and Eigler.[111]

3.1.3 Etching Following a lapping operation the surface of any sample will be damaged to some extent resulting in poor electrical characteristics;[90] therefore, the crystal must be etched in order to remove the damaged surface layer and to obtain a clean surface. (N.B. Strictly speaking, a "clean" semiconductor surface can only be obtained with considerable care and effort, e.g., by cleavage of the crystal under ultra-high vacuum or ion-bombardment. Under normal experimental conditons one obtains a "real" surface; therefore, the designation "clean" in the present work is to be taken to mean "free from whatever sullies or defiles; pure; unsoiled"[126] in order to avoid the use of the term "real clean.")

All of the acid based etchants for germanium and silicon contain at least two major components, an acid in which the oxide of the semiconductor is soluble, and an oxidizing agent capable of re-oxidizing the surface in a uniform manner. For germanium the acid is always HF and the oxidizing agent HNO_3 or, less frequently, H_2O_2. To a mixture of varying proportions of these components may be added other chemicals to control the rate of chemical attack, such as acetic acid which retards the reaction rate, or bromine to accelerate it. The chemical reactions involved (in the ideal situation) are:

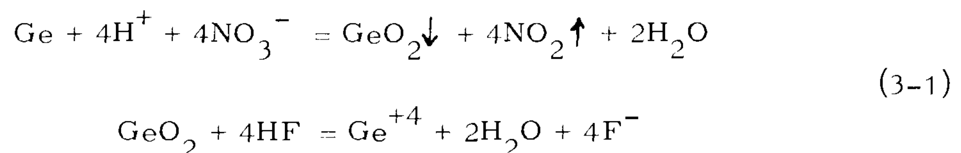

$$Ge + 4H^{+} + 4NO_3^{-} = GeO_2\downarrow + 4NO_2\uparrow + 2H_2O$$

$$GeO_2 + 4HF = Ge^{+4} + 2H_2O + 4F^{-} \qquad (3\text{-}1)$$

In the experimentally obtained surface, the oxide is undoubtedly of the form GeO_x , and the non-stoichiometric composition of the oxide layer contributes to the surface problems.

In the present work, the nickel contacts were masked with acid-resistant tape,[85] and the crystal etched in a 2:1 volume mixture of concentrated HNO_3 and 48% HF for 3 minutes with constant agitation to insure contact of fresh solution with the crystal. The etch was "quenched," i.e., diluted slowly with de-ionized distilled water (> 25 MΩ-cm resistivity), partially decanted, and diluted again until the wash is neutral to indicator paper. The tape masks were removed under water, and the crystal rinsed to remove any material left by the tape. This was followed by a 15 minute ultrasonic wash in de-ionized distilled water; the crystal was dried in a jet of dry nitrogen gas.

3.1.4 Lithium-ion Drift The process used to produce thick compensated regions in germanium is due to Pell[92] in which p-type starting material is compensated with lithium donor ions. After thermal diffusion of lithium into the p-type starting material assumed to have a uniform concentration of ionized acceptors N_A, a p-n junction is produced near the surface. Figure 19(a) shows the concentration gradient of lithium donor ions after the diffusion; impurity atom concentrations are plotted vs distance from the surface into the crystal. The p-n junction interface is at $x = c$ where the concentration of ionized acceptors N_A is equal to the concentration of ionized donors N_D.

If the junction is then reverse-biased at an elevated temperature (to increase the lithium mobility), lithium ions will, under the influence of the applied field, drift from the donor rich region $x < c$ to $x > c$. N_D cannot

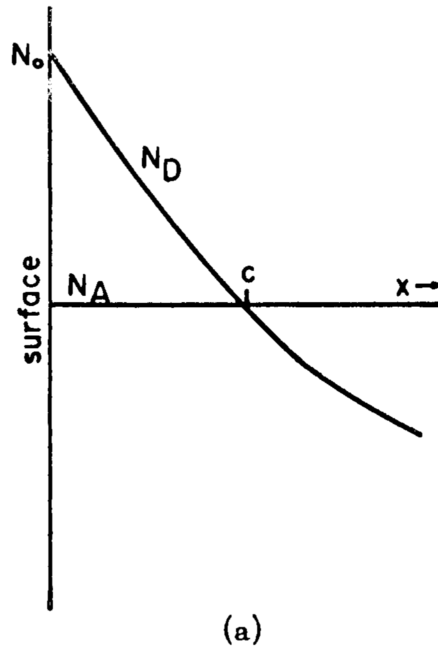

(a)

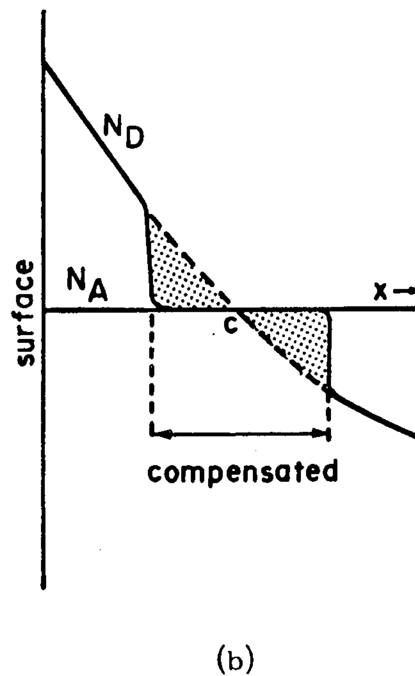

(b)

FIGURE 19: CONCENTRATION OF LITHIUM DONOR ATOMS vs DISTANCE FROM THE SURFACE OF A SEMI-CONDUCTOR CRYSTAL (a) AFTER THERMAL DIFFUSION

become less than N_A for $x < c$ because the excess acceptors in such a region would affect the space-charge so as to increase the field on the side of excess lithium ions and decrease the field on the opposite side. Thus the donor ion flow would be increased into the deficit region until the deficiency in donors disappeared. Similarly N_D cannot become greater than N_A. A Compensated region ($N_D = N_A$) is produced as shown in Figure 19(b); the applied field will be extended over the compensated region as drifting proceeds.

In the present work, the diode was clamped between the electrodes of the drifting bath as shown in Figure 20.[116] Chloroform (b.p. = 61.2°C) was used as the coolant, and all metal parts within the vessel were nickel; we had found that in alloys containing copper, e.g., phosphor-bronze, the reverse bias voltage applied to the diode caused copper to be leached out of the alloy and deposited onto the diode. The use of a liquid coolant in the drifting bath has an advantage over air or other convection cooled set-ups besides increased drift rate; liquid coolants remove heat from the crystal by nucleate boiling.[83] Thus during the drift, bubbles form about the surface of the diode. An imperfection in the p-n junction formed because of thermal or mechanical damage to the crystal may manifest itself as a "hot spot," i.e., more power is dissipated in the damaged region and denser bubbling occurs there. We have found a convenient method[103] for activating dormant hot spots so that they can be identified for subsequent removal: if a small spot of intense white light is shone on the edge of the diode while under reverse bias, the sudden increase in current due to photo-generation of carriers will cause a potential hot spot to flare up. The light source is pulsed on and off so as not to initiate breakdown of the diode due to excess current flow. This method is to be compared to that in which a

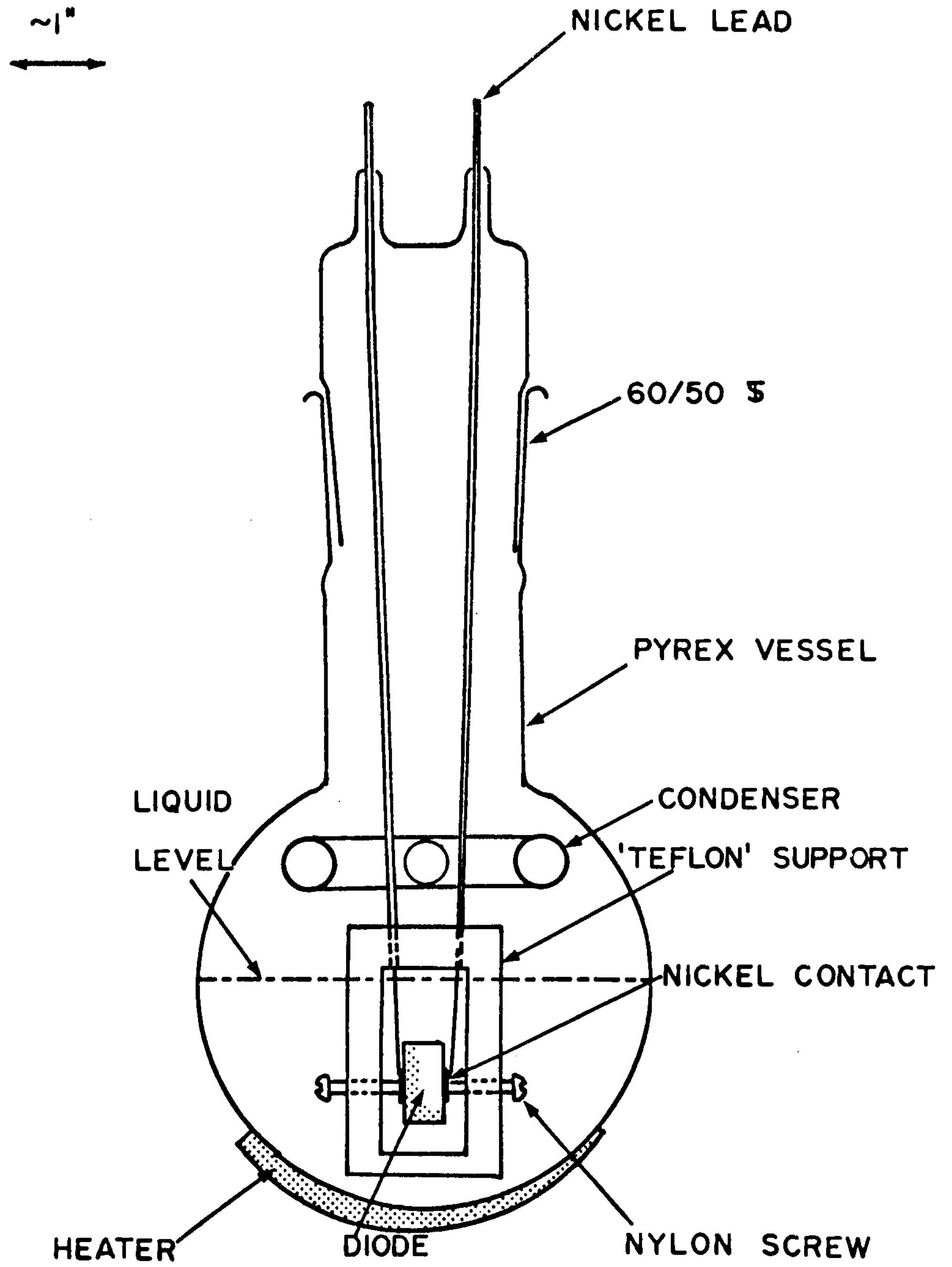

FIGURE 20: DC-DRIFTING BATH

diode is reverse-biased, cooled to $0^{o}C$, allowed to warm up in air under sufficient bias so that the frost formed on the cold crystal surfaces will melt first at a hot spot.[57]

The chloroform was heated to boiling via the external heater, and a reverse DC bias applied to the germanium crystal after it has reached thermal equilibrium with the boiling liquid. The bias was increased to as high a level as permitted by the conditions of the crystal, i.e., fairly constant current level. Since the thermal diffusion of lithium does not yield a uniform p-n junction, the initial bias level may have to be kept low until the quality of the junction has improved. As the width of the compensated region increases with time, the current drawn by the drifting diode will increase. An abrupt increase in reverse current may signify a drop in the lithium ion concentration due to diffusion to the surface[51] or precipitation to the electrically inactive elemental state, and further drift will not occur unless more lithium is thermally diffused into the crystal.

Henck, et.al.,[51] in a study of diffusion, drift rate, and precipitation of lithium in germanium found that for thermal diffusions carried out at temperatures and times similar to those used in the present work, approximately 6×10^{14} lithium atoms/cm^2 are initially introduced into the crystal. This should be sufficient to compensate germanium of greater than 10 Ω-cm resistivities to a depth in excess of 1 cm. This was found to be consistent with the results obtained with the Sylvania germanium, where a single lithium diffusion was sufficient to yield compensated depths of up to 8 mm.

The drift rates from diodes cut from both Sylvania ingots has been found to be consistent with the relationship[113,116]

$$w = (2\mu Vt/kT)^{\frac{1}{2}} \qquad (3-2)$$

where w is the compensated depth, μ the lithium mobility, V the bias voltage, t the drift time, and T the temperature at which the drift is carried out. The progress of the drift was monitored through the position of a line of chloroform decomposition products[114,116] which forms at the i-p boundary. Copper plating of the uncompensated material[16] was also used to determine the depth of the drift.

The steps following the drifting of the diode to the desired compensated depth determine the final performance of the device as a spectrometer. We will therefore outline the production of thick compensated regions in germanium by the AC-drift method of Jamini,[56] followed by a detailed discussion of the post-drift procedures which are essentially the same for germanium p-i-n diodes, irrespective of the drifting procedure used.

3.2 AC-Drift[56] In this procedure, lithium which has been thermally diffused into both faces of germanium crystal was drifted, from both faces, into the crystal via an AC bias voltage. This simultaneous drifting of what is essentially a dual-diode structure results in the production of a thick compensated region in less time than the same thickness would require using the DC-drift described above.

After a crystal of germanium of the required size was cut from the ingot (Hoboken #71D in the present work) by the procedure as previously described, lithium-in-oil was painted onto the two faces of the crystal, and the thermal diffusion was carried out under the same conditions used for devices prepared for the DC-drift. Jamini's method[56] calls for contacts to be applied to the faces using a gallium-indium eutectic mixture (76% Ga and 24% In by weight).[48] Since good ohmic contacts to germanium can be

obtained with Ga-In only if the semiconductor surface is degenerate (see earlier), it was found necessary to construct a simple four-point probe for measuring surface resistivity of the samples (see Appendix A). In applying the probe to the problem of assuring good ohmic contacts with the Ga-In eutectic, the n-surfaces of the crystal were alternately lapped and probed until a uniform resistivity of less than 0.1 Ω-cm was obtained; Cappellani, et.al.,[17] found that if the surface resistivity were greater than about 0.5 Ω-cm, excessive carrier injection will occur at the contact with Ga-In.

After the required resistivity was obtained for both faces of the crystal (additional lithium diffused into the crystal if the resistivity cannot be obtained), the crystal was etched unmasked in a 3:1 volume mixture of HF and HNO_3 to which has been added a few drops of bromine,[56] for 90 seconds. After washing in de-ionized distilled water, the crystal was dried in warm air, and the Ga-In contacts were rubbed onto the faces of the warm crystal.

The drifting bath used in the AC-method is shown in Figure 21. The liquid coolant was Freon 113 (1,1,2-trichloro-1,2,2-trifluoroethane, b.p. = 47.7°C), and the power supply was capable of delivering a maximum of 600 volts rms at 1.5 amps; provision was made for observing, on an oscilloscope, the time variation of the current/voltage of the drifting dual-diode.[56] As drifting proceeds, the need for further thermal diffusion of lithium becomes apparent when the current drawn by the crystal becomes excessive (1 amp at 100 volts).[56] In drifting a crystal to a compensated depth of 8 mm (approximately 4 mm from each face), three diffusions of lithium were required. For the material used (35-37Ω -cm), the quantity of lithium diffused into each face of the crystal should have been sufficient

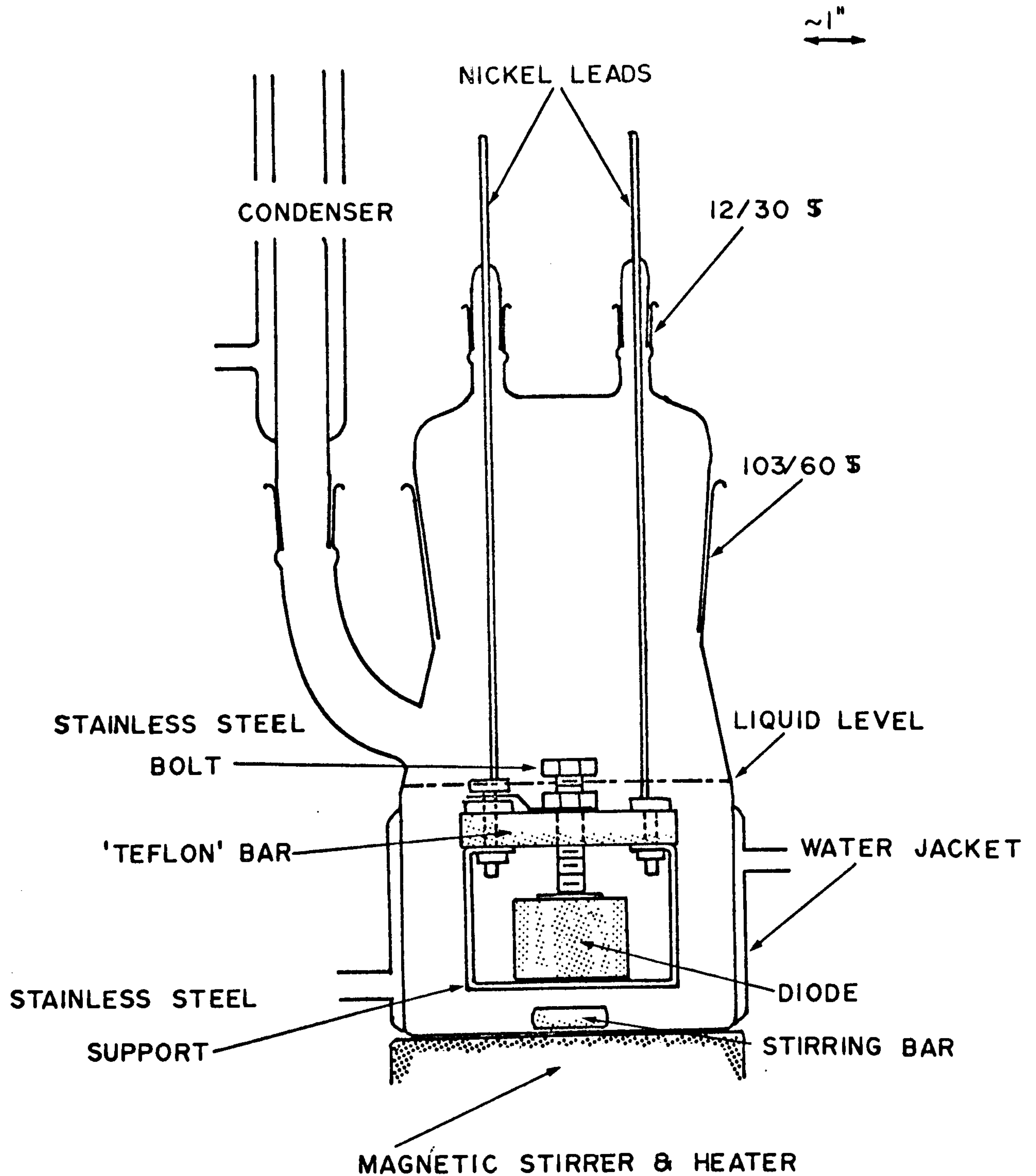

FIGURE 21: AC-DRIFTING BATH

to compensate more than 50 mm of germanium in each direction allowing for diffusion to the surface during drifting.[51] The excessive current, then, was undoubtedly due to depletion of lithium from the contacts of Ga-In eutectic rather than from loss of lithium in the bulk of the crystal itself.

During the AC-drift, lithium from the two n-surfaces will drift towards the center of the crystal compensating acceptor impurity ions so that the crystal has the configuration n-i-p-i-n, i.e., a dual-diode. The two compensated regions will eventually merge (at least partially); copper-plating[16] of the surface of the crystal will then show a thin line of uncompensated p-material remaining. One of the n-contacts was removed by lapping until the resistivity as measured by the four-point probe indicates removal of the lithium rich region. Gallium was thermally diffused into this region to obtain a p-type contact; simultaneously the n-contact on the opposite face was renewed by lithium diffusion. This simultaneous diffusion was carried out under argon at 375°C for 15 minutes. After cooling and removal of the excess diffusants, the surfaces were lapped and probed, and Ga-In eutectic was rubbed onto both faces. The crystal, now with a p-i-p-i-n configuration (the central p-type region being the original uncompensated material left after the AC-drift) was replaced in the drifting bath; the power supply with the addition of a rectifying bridge was used to reverse-bias the device so that the remaining p-type region will be compensated. Because of the p-contact may also be compensated during the process, it was found necessary to renew the contact with Ga diffusions several times. Copper-plating was used to check the progress of the merging of the compensated regions. When the process has been completed, the resulting diode has the required p-i-n configuration as was obtained using the

DC-drifting procedure; however, p-i-n diodes produced by the AC process are totally compensated, having only very thin n- and p-regions which serve as contacts. DC-drifted diodes may have considerable original p-type material remaining depending upon the length of the drift.

3.3 Post-Drift Procedures Two steps must be taken after lithium ion drifting to assure that the resulting p-i-n diode will perform optimally as a high-resolution gamma-ray spectrometer. The lithium-compensation after a high temperature drifting operation will not be as exact as required, and the surface must be treated so as to minimize the excesss noise contribution as previously discussed.

3.3.1 Clean-up Drift If, during the drift process, there were no reverse leakage current, the negative space-charge in the ion drift region due to filled acceptors would be neutralized by the positive space-charge of the drifting donors,[120] and an exact compensation of acceptors by lithium donor ions would result. At the elevated temperatures used to increase the lithium mobility, a large bulk current results, mainly from carrier generation in the compensated region;[79] under the drifting field, these carriers contribute to the net space-charge, so that inexact compensation is achieved by the lithium donors.

Inexact compensation of a p-i-n diode will contribute to the overall system noise in two ways. Firstly, the presence of uncompensated acceptors will result in increased noise due to thermal carrier generation, and secondly, the capacitance of the device will be high. Since p-i-n and p-n junctions have regions of space-charge separated by a region depleted of charge carriers, they may be thought of as parallel-plate capacitors where the capacitance C is given by:

$$C = \frac{KA}{4\pi w} \qquad (3-3)$$

where K is the dielectric constant, A the area of the junction, and w is the width of the compensated region. For germanium this becomes:

$$C = 14.4\ A/w \quad (pf) \qquad (3-4)$$

where A is in cm^2 and w in mm. The capacitance should be independent of the bias voltage V; however, in p-i-n devices C is usually found to vary as $V^{-1/3}$ after the high temperature drift.[79] Since the noise of the pre-amplifier depends upon input capacitance, the lower the detector capacitance, the lower the pre-amplifier noise.

Thus in order to improve the degree of compensation in a lithium-drifted germanium diode, a "clean-up" drift[39,83] is carried out. In this process, a larger reverse bias is applied to the device at a lower temperature than the first ion-drift; the bulk-generated space-charge is reduced, but the higher bias is required to make up for the decreased lithium mobility.

3.3.2 Surface Treatment Measurements of surface potentials by Davies and Webb[27] and Armantrout[4] have indicated either n- or p-type surface layers can be formed over the i-region after the acid etching procedure. The presence of these surface layers which result in there being a marked difference between the surface and bulk potentials lead to a low value of the reverse bias at which diode breakdown occurs; thus at the high bias levels which are normally required to insure complete charge collection in the device, the leakage current is too high to yield good detector resolution. In the work by Armantrout[4] an exhaustive study was carried out to determine the effectiveness of various chemical agents in modifying the surface potentials of Ge(Li) detectors so that the level at which breakdown occured

could be increased; the effects due to dipping the diode into methanol, trichloroethylene, nitric acid, hydrogen peroxide, water, and ammonium hydroxide were measured. The chemical treatment apparently used by many researchers has been the hydrogen peroxide dip.[17,49,76] Since it has been known that for germanium, H_2O_2 produces a p-type surface inversion layer and wet air yields an n-type surface layer,[59] the effect noted on Ge(Li) detectors can be explained as follows. The exposure of the diode to water and air during the quenching of the etch and washing steps produces an n-type surface layer on the crystal; subsequent soaking in H_2O_2 causes a reversion, or compensation if you will, of the n-type layer so that the surface potential approaches the level of the bulk potential in the i-region. The change in surface potential produced with H_2O_2 is strongly dependent upon the time of exposure to the oxidizing agent: lack of reproducibility of results has been reported.[4,17,49,76] Part of the problem, as pointed out by Webb and Davies,[27] is that, for reasons as yet unknown, some samples of germanium yield diodes with high values of bias before breakdown occurs, while other samples yield no usable diodes under the same conditions of treatment. This inconsistency in the quality of germanium ingots available will be discussed at a later time as it applies to the present work.

Recently Adams[1] studied the effects of prolonged exposure of a Ge(Li) detector to H_2O_2 and the length of exposure to moist air to the raising of the bias level at which breakdown occurs. The highest breakdown bias level was attained after the diode was soaked in H_2O_2 for 30 minutes and then allowed to dry for 45-50 minutes in air of 48-50% relative humidity.

In the present work, the post-drift procedures were as follows: the diodes were etched for 3 minutes in a 3:1 volume mixture of HNO_3 and HF, followed by a 15 second etch in a 5:1 mixture of the acids. After quenching

and washing in de-ionized distilled water, the diodes fabricated from the Sylvania ingots (which did NOT respond favorably to the chemical soakings) were dried in a jet of dry nitrogen gas and mounted in the cryostat (see Appendix B) as quickly as possible to minimize interaction with the room ambient. The samples from the Hoboken ingot, after washing, were soaked in H_2O_2 after the method of Adams[1] and mounted in the cryostat. Once the cryostat was evacuated to below about 10^{-3} mm Hg, the system was cooled ($-72^{\circ}C$ for the Sylvania samples, $-20^{\circ}C$ for the Hoboken samples) in preparation for the clean-up drift. Between 600 and 1000 volts reverse bias was applied to the diode until no further reduction in leakage current was observed (5-7 days). At this time the cryostat was cooled to $77^{\circ}K$ at which temperature the leakage current vs bias characteristic was measured.

CHAPTER IV

EXPERIMENTAL RESULTS

4. We now wish to describe the devices fabricated by the techniques detailed in the previous chapter. For the purposes of this discussion, we will first turn to an examination of theses devices as p-i-n diodes in terms of rectification characteristics, capacitance, etc., and later describe them in terms of their performance as gamma-ray spectrometers.

Germanium ingots available from various commercial sources have shown at least two variations which have made the production of Ge(Li) detectors rather difficult and unpredictable. Some samples show a drift rate for lithium[5,42] which is many orders of magnitude below that expected from the relationship given by equation 3-2, while other germanium ingots yield diodes whose rectification characteristics made them unusable as gamma-ray spectrometers.[27] The apparent decrease in the diffusion coefficient of lithium in germanium appears to be due to the presence of oxygen in the sample so that lithium ions become immobilized by the formation of a $Li\text{-}O^+$ complex.[42] The poor rectification action of some Ge(Li) diodes, large reverse currents at low biases, has not as yet been explained, and variations may be found in diodes produced from the same ingot.[22] The majority of diodes produced in the present work from the Sylvania ingots exhibited poor rectification characteristics, but drift rates were found to be in agreement with equation 3-2.

4.1 <u>Rectification Characteristics</u> Figure 22 shows a plot of the leakage current vs reverse bias characteristic (hereafter termed the I(V) characteristic) for device D-4(7) at $77^{\circ}K$ before the clean-up drift (open circles) and after a 5 day clean-up drift at $-72^{\circ}C$ and 1000 volts reverse bias (solid points).

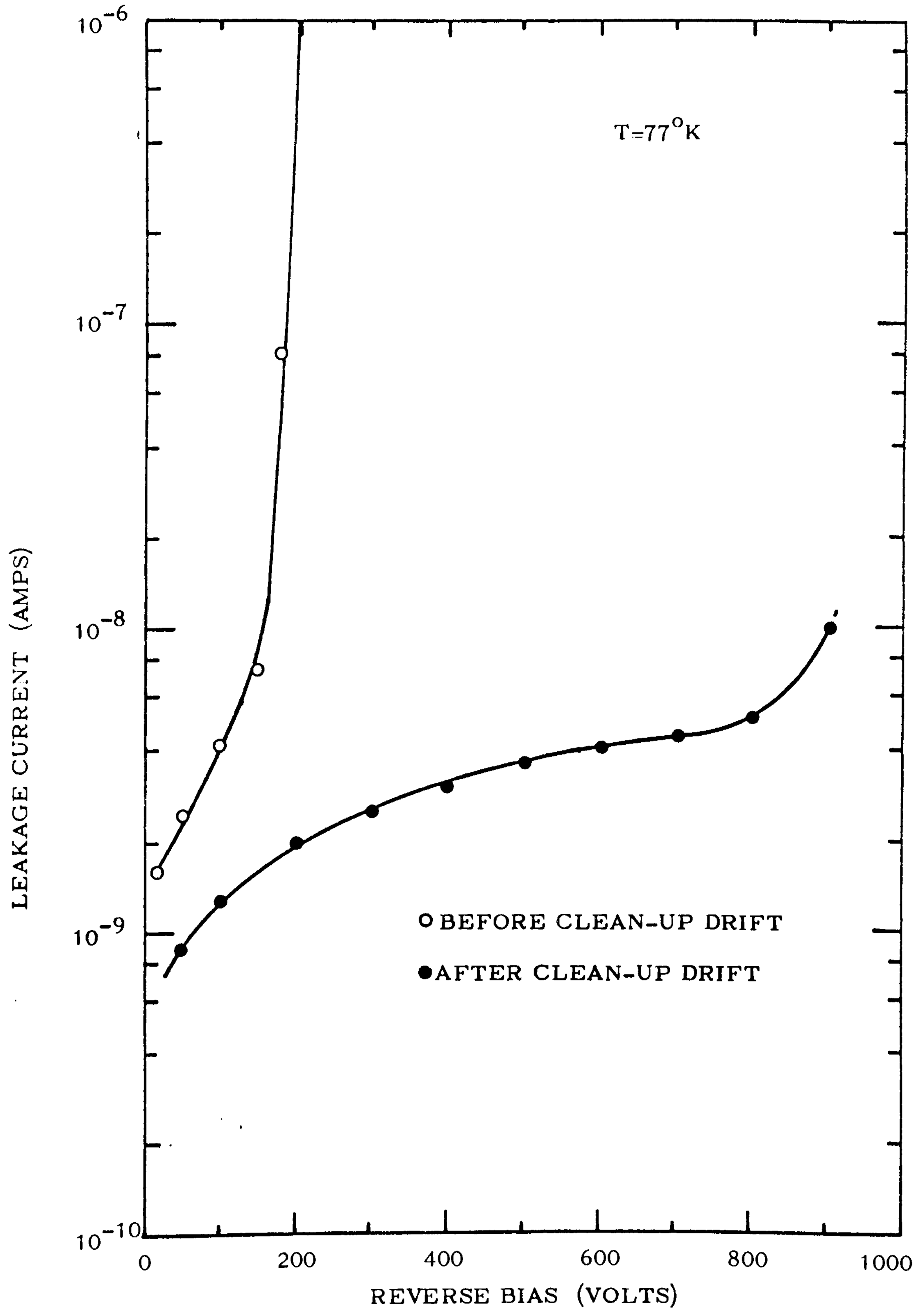

FIGURE 22: LEAKAGE CURRENT vs REVERSE BIAS FOR A p-i-n DIODE FROM SYLVANIA INGOT 597G-6.

The clean-up drift has resulted in an increase of the bias level at which breakdown occured from 150 volts to over 800 volts. This device was fabricated from a crystal cut from one end of Sylvania ingot #597G-6; devices cut from other portions of the ingot show progressively poorer I(V) characteristics approaching that shown in Figure 23 which is typical of all devices fabricated from Sylvania ingot #564G-1. As can be seen from Figure 23, the leakage current after the clean-up drift (solid points) monotonically rises with bias, the conditions of the clean-up drift being the same as above.

The leakage current response with bias as shown in Figure 23 might arise from either surface effects or clean-up drift of insufficient length so that the lithium compensation was still inexact (see earlier). Thus when the poor diode characteristic was initially encountered, measurements of device capacitance were used to determine if the lithium compensation was incomplete. Figure 24 shows results of capacitance vs reverse bias measurements for a 1.7 cm^2 x 0.5 cm device taken before a clean-up drift (open circles) and after a two-stage clean-up drift at 10°C and -72°C (solid points); the measurements were made at 77°K using a General Radio 1608-A 1 KHz impedance bridge. The initial response taken after the high temperature drifting process (before clean-up) exhibits the strong bias dependence of the capacitance indicative of inexact lithium compensation.[34,79] After the clean-up drift, the capacitance is seen to be bias independent above approximately 100 volts; in practice, it seems that a completely flat capacitance-bias response is rarely achieved for Ge(Li) diodes (see for example reference 39). Using equation 3-4 the expected capacitance for a device of the dimensions given above can be calculated;

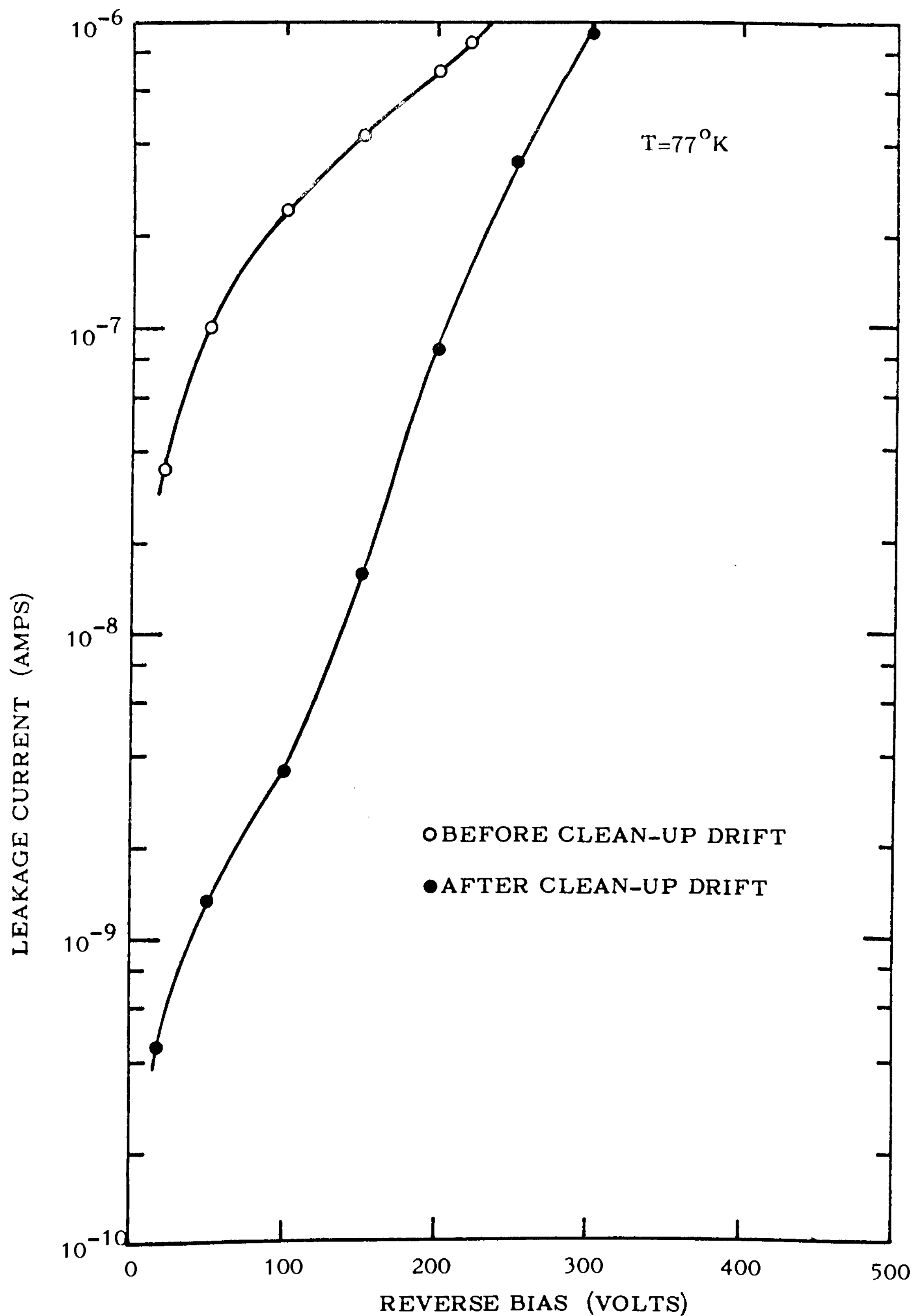

FIGURE 23: LEAKAGE CURRENT vs REVERSE BIAS FOR A p-i-n DIODE FROM SYLVANIA INGOT 564G-1.

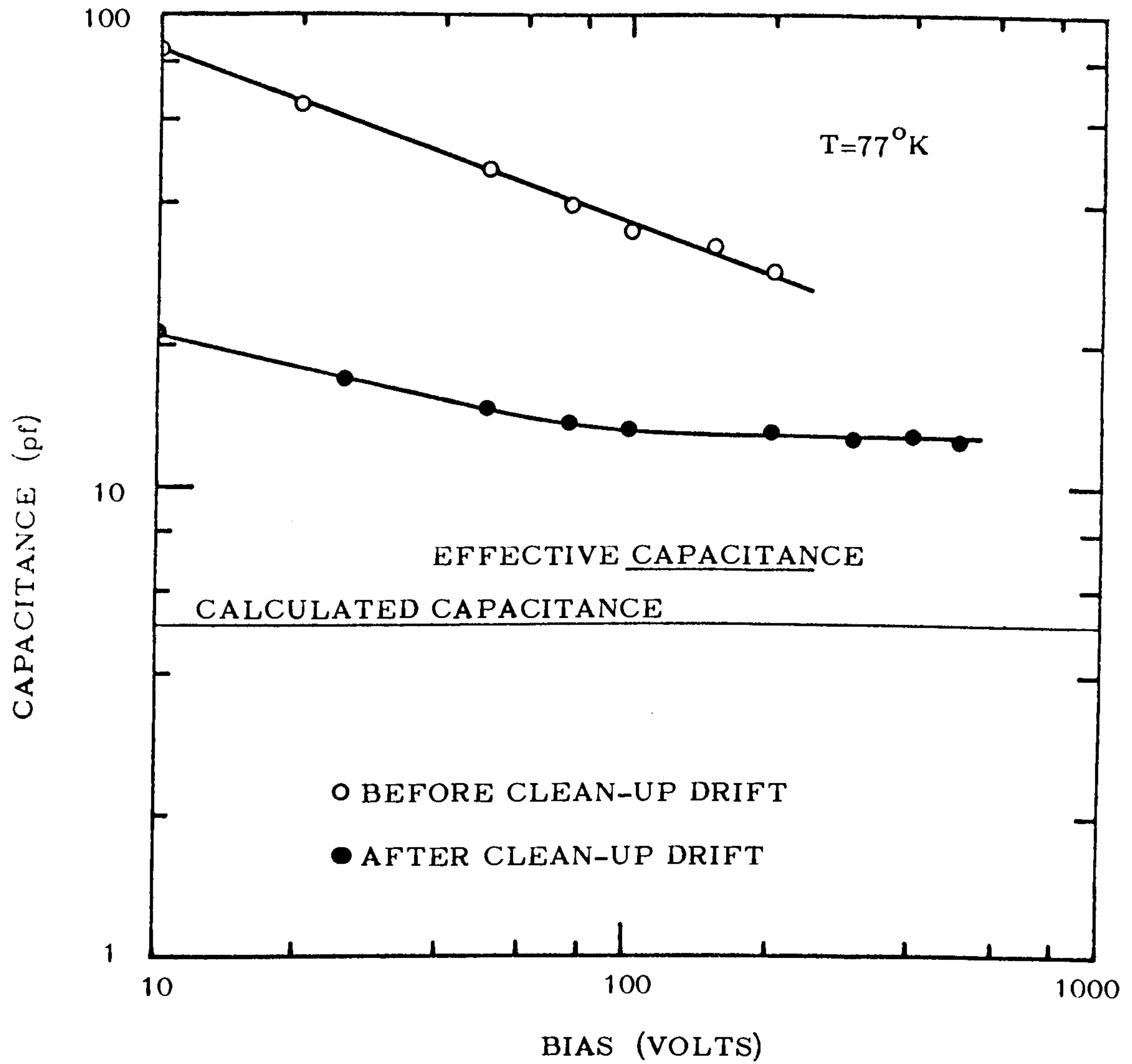

FIGURE 24: CAPACITANCE vs BIAS FOR A p-i-n DIODE

the calculated capacitance, approximately 5 pf, is smaller than that measured at 1 KHz by a factor of 2-3. Hansen and Jarrett[49] have reported a similar discrepancy for capacitance measurements made at audio frequencies, due to surface effects of the p-i-n diode. In the present work, therefore, the bridge-measured capacitance have been used only as a qualitative indicator of detector compensation. Also shown in Figure 24 is the "effective capacitance" as measured from noise vs input capacitance data supplied with the pre-amplifier (ORTEC model 118 FET); the result includes stray capacitance due to connecting wires, electrical feedthroughs, etc. and is in agreement with the calculated value. Thus if the capacitance of a device was bias independent over a wide range of bias and/or its effective capacitance was in agreement with the calculated value, it was assumed that the device had received sufficient clean-up.

The monotonically rising leakage current with reverse bias response was the next matter for concern; the effect was tried of certain surface treatments such as methanol rinses or hydrogen peroxide dips.[4] No improvement was observed after such surface treatments on any of the diodes fabricated from Sylvania ingot #564G-1. A process was successfully devised by which the leakage current could be lowered for such devices (although the slope remained essentially the same), and this procedure is described below.

4.1.1 <u>CaF_2 Compensation of Surface States in Ge(Li) Detectors</u>[106] Some results reported[46] on controlling surface potentials in evaporated CdS films using various thicknesses of CaF_2 and SiO_x layers were applied to the present problem of lowering the leakage current of Ge(Li) devices fabricated from the Sylvania ingots. It was shown in the CdS work that

by using various thicknesses of CaF_2 and SiO_x layers in combination, surface potentials in between those of CaF_2 and SiO_x alone could be obtained. Consequently, if the Ge(Li) detectors with presumably n-type surfaces were coated by vacuum-evaporating a suitable thickness of CaF_2 onto the exposed edges (this material having been shown to raise surface potentials on CdS), one would expect to obtain surface potentials for germanium near those of the bulk material; a lowering of the leakage current should follow. Furthermore, following such a treatment, in which a material coating is applied to the diode surface, the device should be fairly insensitive to further exposure to the ambient, and its behavior should be reproducible.

After the diode (fabricated by the process described earlier) had been given the final etch and water wash, it was mounted in the cryostat, and the leakage current and resolution for various standard gamma-rays were measured at $77^{o}K$. The detector was then warmed to room temperature under vacuum over a period of 3 to 4 hours and then brought up to atmospheric pressure with nitrogen gas. It was removed from the cryostat on a detachable mount (see Figure 25(a)) and inserted in the vacuum evaporation system. Figure 25(b) shows schematically the detector and mount in position for the CaF_2 treatment. The mounting permits rotation of the rectangular detector for treatment of each of the four edges. A quartz crystal and frequency monitor were used to determine the thickness of the deposited material (to within 10%), the change in frequency of the crystal being proportional to the mass deposited onto it. Rates of CaF_2 evaporation were typically 20 to 200 A^{o} per second. After treatment, the diode was remounted in the cryostat, cooled to $77^{o}K$, and tested as before.

O-RING SEAL
MICRODOT CONNECTOR
MINIATURE PLUG
COPPER COLD FINGER
Ge(Li) DETECTOR
INDIUM FOIL
ALUMINUM MOUNT
TAPPED TO RECEIVE SHAFT
MOUNT UNSCREWS HERE
~ 1"

(a)

TO FREQUENCY METER AND RECORDER
DETECTOR AND MOUNT
SUPPORT
TEFLON BUSHING
QUARTZ CRYSTAL FREQUENCY MONITOR
FLEXIBLE SHAFT
CaF_2

(b)

FIGURE 25

Tavendale[115] has reported that thermal recycling of some Ge(Li) detectors from 77°K to room temperature for 5 minutes resulted in improved performance, and particularly an increase in the bias at which breakdown occured. In this work, the times involved from warm-up to room temperature to cooling to 77°K after the CaF_2 treatment were such that the diode was at room temperature from 10 to 12 hours. The following experimental results, however, indicate that the effects observed with CaF_2 on germanium were similar to the effects noted in the CdS work, and are presumed to be largely due to the CaF_2 treatment.

Figure 26 shows the I(V) characteristic of a 3 cm^2 x 0.2 cm thick Ge(Li) detector before and after 2000 A° of CaF_2 was evaporated onto the etched junction edges. This thickness is seen to produce a substantial increase in reverse leakage current; this is attributed to the formation of a heavy p-type surface inversion layer on the detector as such potential shifts were noted in the CdS work for layers of this thickness.

Figure 27 gives the results for the deposition of a 200 A° layer of CaF_2 on a 2 cm^2 x 0.35 cm thick detector. The leakage current is considerably lower after the treatment for reverse bias voltages of less than 120 volts. The higher leakage current observed above this bias is probably indicative of a somewhat p-type surface so that at higher bias voltages excess current is still observed.

Data obtained after a 150 A° CaF_2-coating on a 1.7 cm^2 x 0.5 cm thick Ge(Li) detector is shown in Figure 28. This treatment has resulted in a lowering of the leakage current over almost the entire bias range measured; apparently 150 A° of CaF_2 produced a surface potential nearly equal to the bulk potential for this detector. The resolution obtained

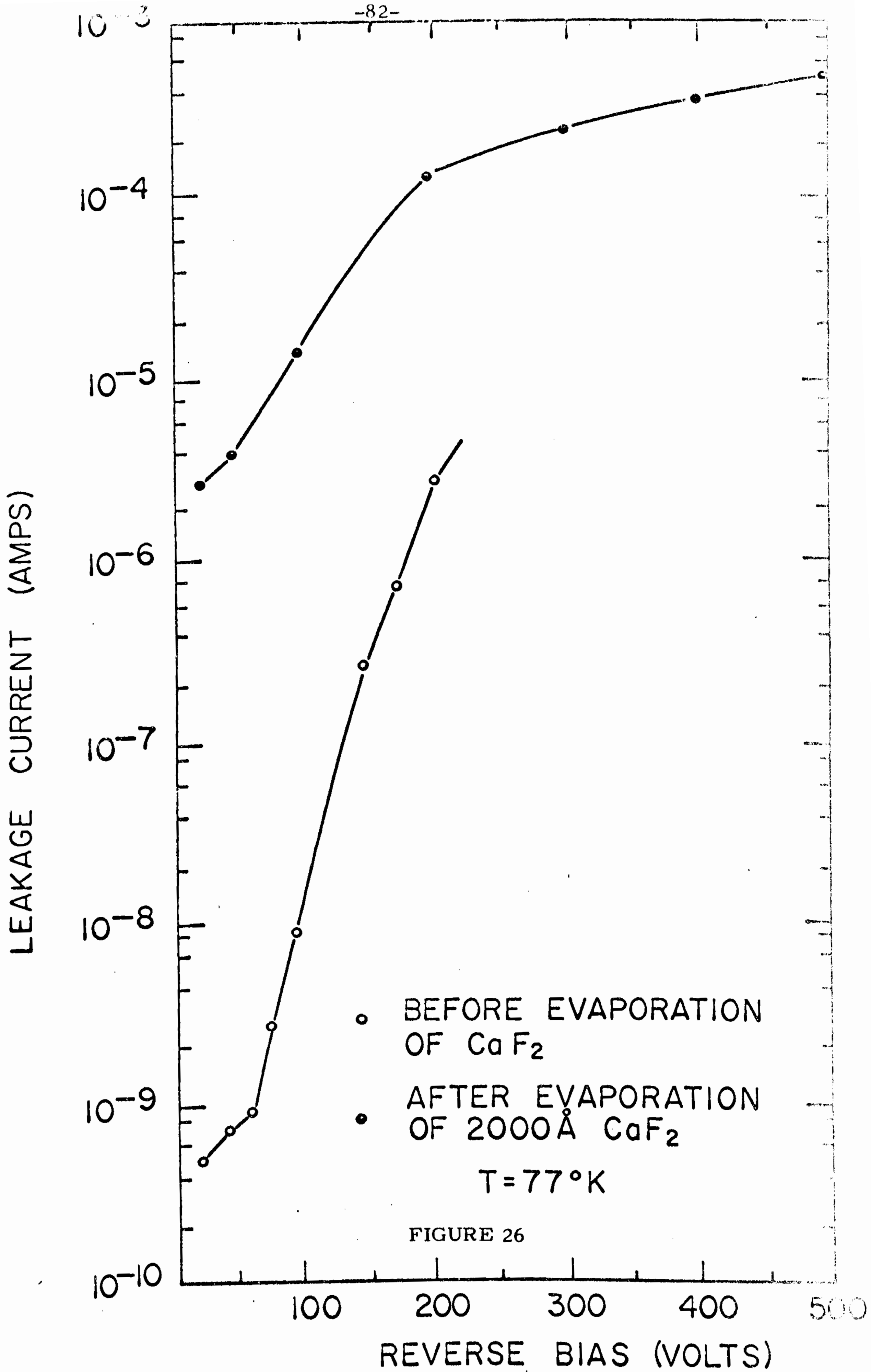

FIGURE 26

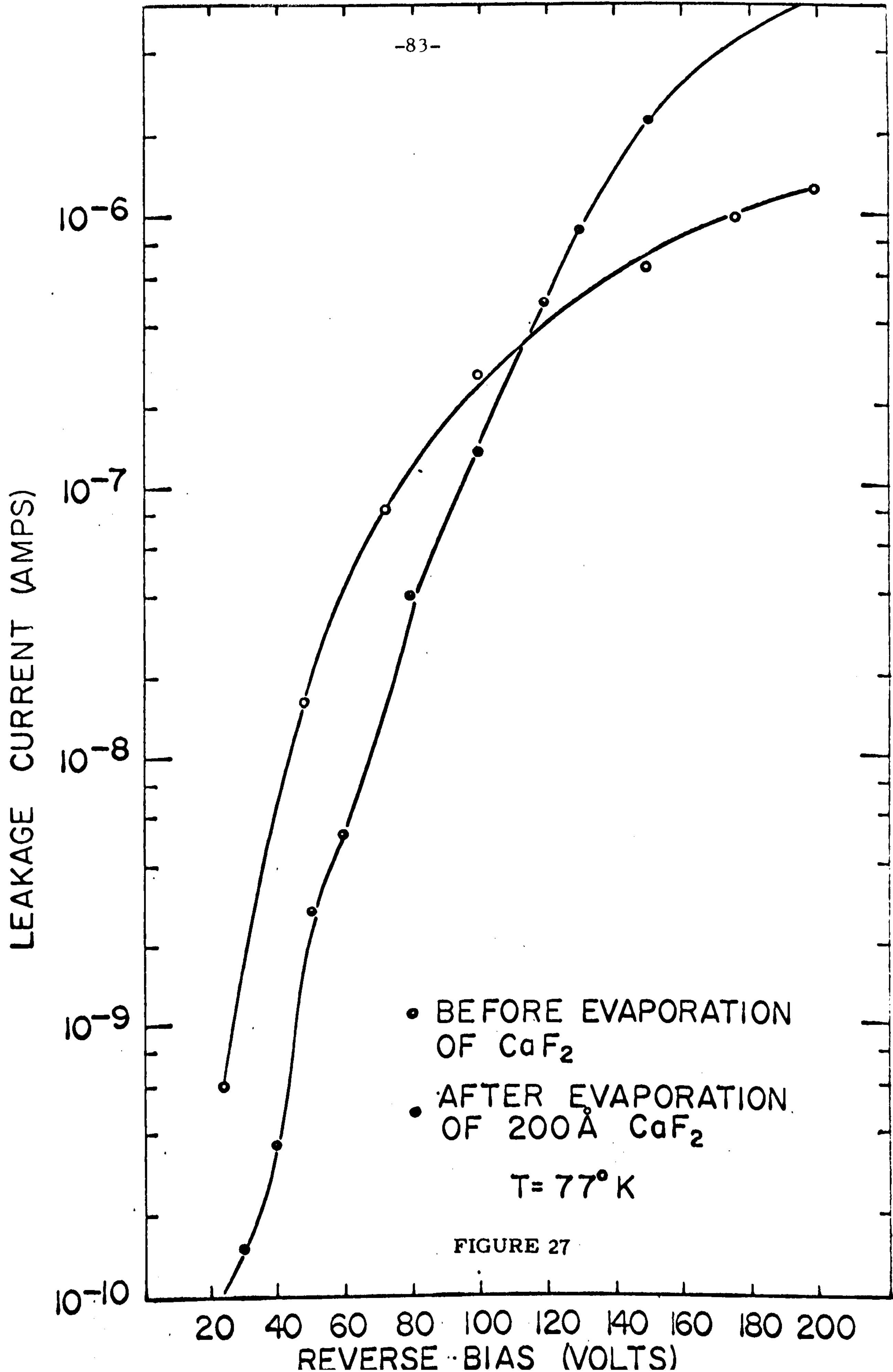

FIGURE 27

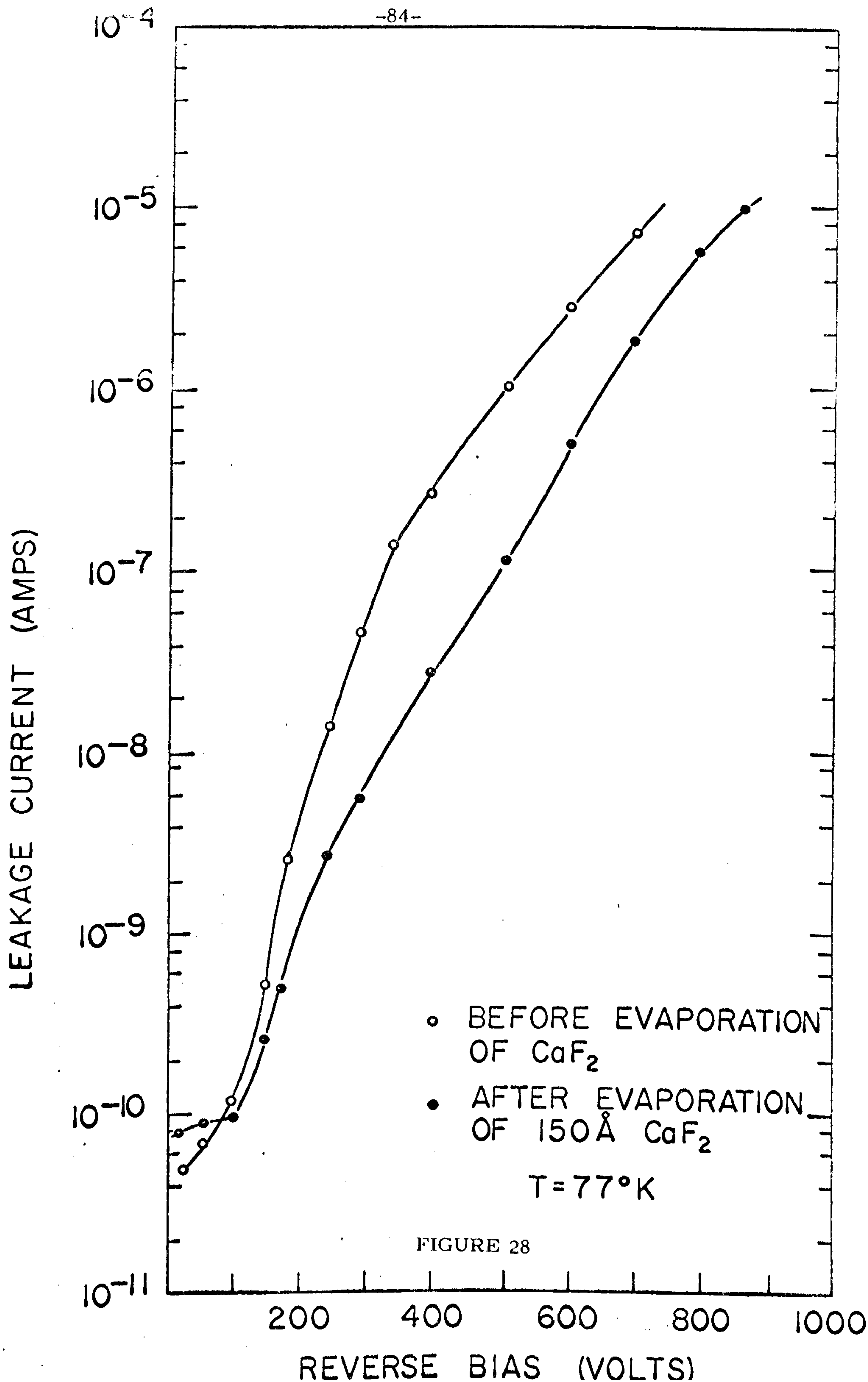

FIGURE 28

with this detector after the CaF_2 treatment showed a 10% improvement over the untreated device; use of an ORTEC model 118 FET preamplifier operated at room temperature and a Tennelec TC-200 main amplifier operated in the single-RC clipping mode with 1.6 microsecond time constants yielded resolutions with this detector of 1.79 keV FWHM at 122 keV, and 2.76 keV FWHM at 1173 keV under 150 volts detector bias (Figures 29 and 30, respectively).

Evaporation of a 50 A^o coating of CaF_2 on a 3 cm^2 x 0.2 cm thick detector yielded essentially no change in the observed I(V) characteristic; apparently this thickness of CaF_2 is inadequate to reverse the surface potential, which is again consistent with the CdS results.[46] The detector coated with 50 A^o of CaF_2 was accidently exposed to the atmosphere for a few seconds while at 77^oK; when pumped down to 10^{-6} Torr, the reverse leakage current was found to be essentially unchanged as compared to before the exposure. In order to test further the possible edge-protection properties of the CaF_2 treatment, the detector was exposed to the atmosphere for 30 minutes while at 77^oK. During this period, the leakage current was observed to increase by a factor of from 10 to 100 over 20 to 1000 volts, probably due to conduction through the ice layer which formed over the detector between the positive and ground contacts. However, after the detector was warmed to room temperature under vacuum and cooled once more to 77^oK, no significant increase in the leakage current was found as compared to data taken before exposure, e.g., 4.4 vs 3.2 x 10^{-9} amps at 100 volts, 5.8 vs 5.6 x 10^{-7} amps at 300 volts, and 8.6 vs 8.7 x 10^{-6} amps at 600 volts.

We have had opportunity to observe the long-term stability of the CaF_2-

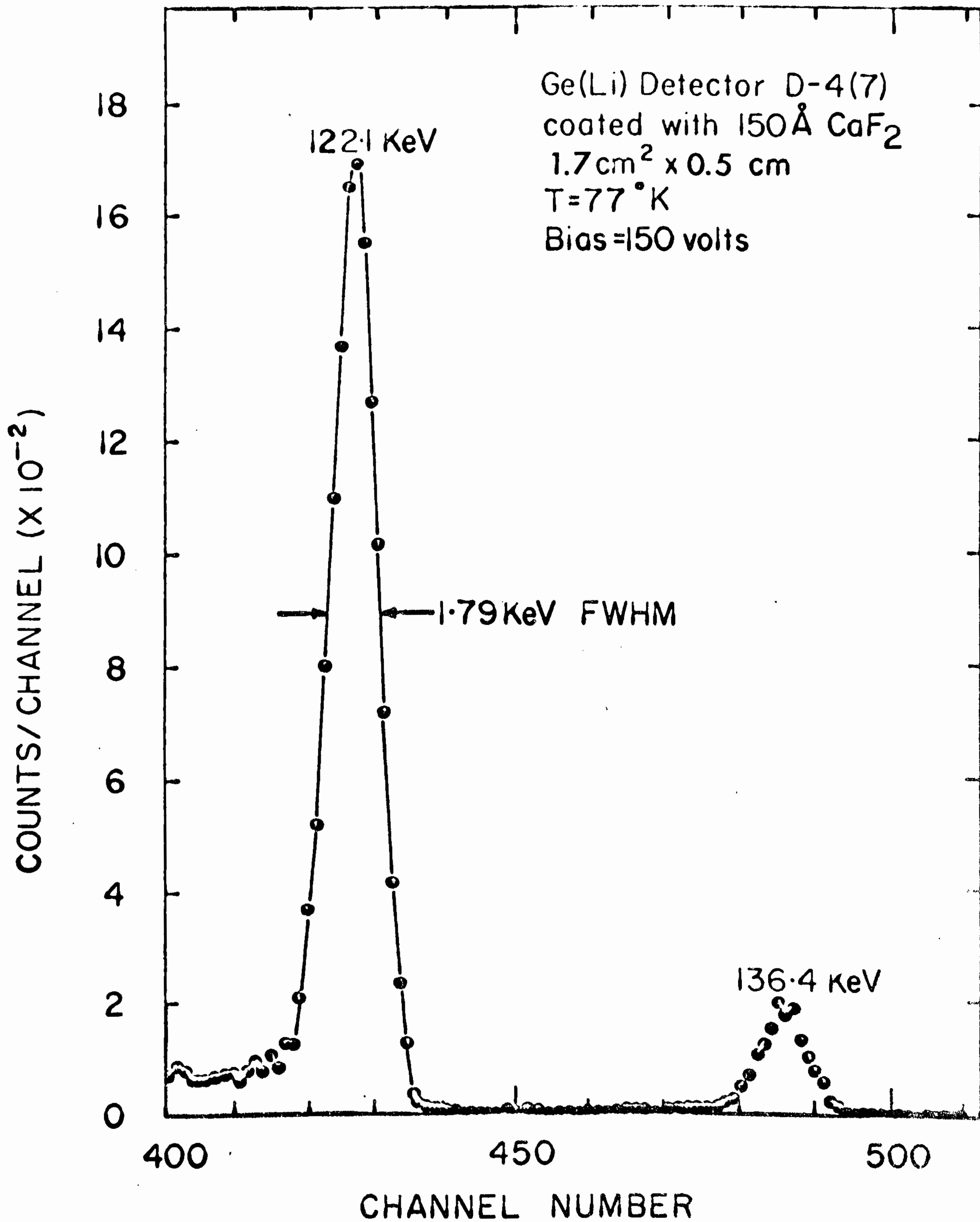

FIGURE 29

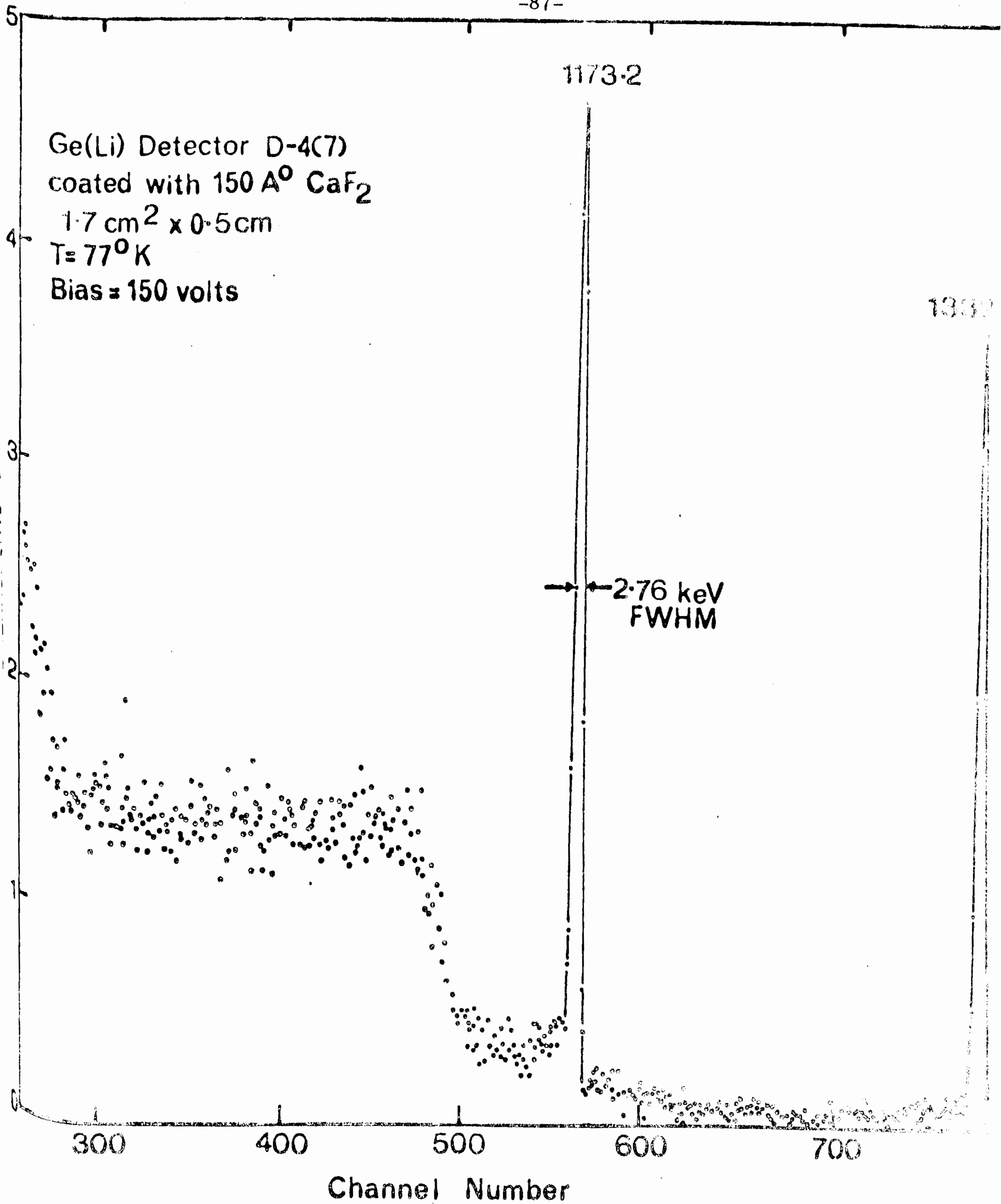

FIGURE 30

coating after exposure to the atmosphere in the case of the detector coated with 150 A^o of the material. Due to a defect in the cryostat, this detector has been exposed for a total period of approximately 90 minutes to the ambient while at 77^oK; over a 6 month period, the resolution obtained at 122 keV has deteriorated to approximately 3 keV FWHM. The hygroscopic nature of CaF_2 is probably responsible for this degradation. The results obtained, however, point to the possible use of such coatings both for adjusting surface potentials and surface protection of Ge(Li) detectors. The use of MgF_2-coatings, such as used on photographic lenses, should be both rugged and insensitive to the ambient.

The CaF_2 coating procedure, while it did cause a lowering in reverse leakage current, did not result in raising the bias level at which breakdown occurred in the devices fabricated from the Sylvania ingots (monotonically increasing leakage current vs bias characteristics were still observed). Thus, whereas the capacitance measurements tended to show that the excess leakage current was not due to inexact lithium compensation, the results of the surface treatment study seemed to indicate that the condition of the surface was not completely responsible for the observed I(V) characteristic either. One difference consistently observed between diodes fabricated from ingot #564G-1 (where all devices exhibited an I(V) characteristic like that shown in Figure 23) and ingot #597G-6 (which yielded one device whose characteristic is shown in Figure 22, while the I(V) characteristic of others became progressively like those of ingot #564G-1 as slices were cut from the ingot) was in the lithium ion drifting step. Comparison of four diodes from each ingot of approximately equal volumes show that diodes from ingot #564G-1 drew 50-70 $mA/cm^3/V$ during the high temperature drift, while diodes from the other ingot drew only 1-2 $mA/cm^3/V$. Thus it

is conceivable that some unknown variation in the bulk material is reponsible for the measured I(V) characteristic of the completed detectors at 77°K.

4.2 <u>Spectrometer Performance</u> In fabricating Ge(Li) detectors, one strives to obtain devices which have low enough leakage current to minimize the detector noise at bias values high enough to collect the radiation-induced charge efficiently. Diodes fabricated from Sylvania ingot #564G-1 were unusual in that while most devices previously reported in the literature have required at least 300 volts bias to operate satisfactorily, the detectors in the present work yielded satisfactory resolution (5-7 keV FWHM at 662 keV) at average bias voltages of only 70 volts.[104]

Figure 31 shows results obtained from the best diode fabricated from the ingot; at 70 volts reverse bias, this detector of approximately 1.5 cm^3 active volume yielded 3.6 keV FWHM for the Co^{57} 122 keV gamma-ray. The associated electronic equipment consisted of an ORTEC model 118 FET preamplifier (with the FET at room temperature), a Tennelec TC-200 main amplifier with 0.8 microsecond integrating and differentiating time constants, and a Nuclear Data ND-160 multiparameter pulse-height analyzer. As the inset shows, this detector has its edges bevelled to an angle of approximately 40°. Figure 32 shows a portion of the Co^{60} gamma-ray singles spectrum obtained with this detector at 70 and 35 volts bias. As indicated, a resolution of 4.3 keV FWHM was obtained for the 1173 keV peak at 70 volts bias, while at 35 volts a considerable amount of "tailing" on the low energy side of the peak was observed indicating poor charge collection due to carrier trapping. At 20 volts bias, the two Co^{60} full-energy peaks cannot be resolved above the background continuum.

A comparison of results obtained with two Ge(Li) detectors of comparable

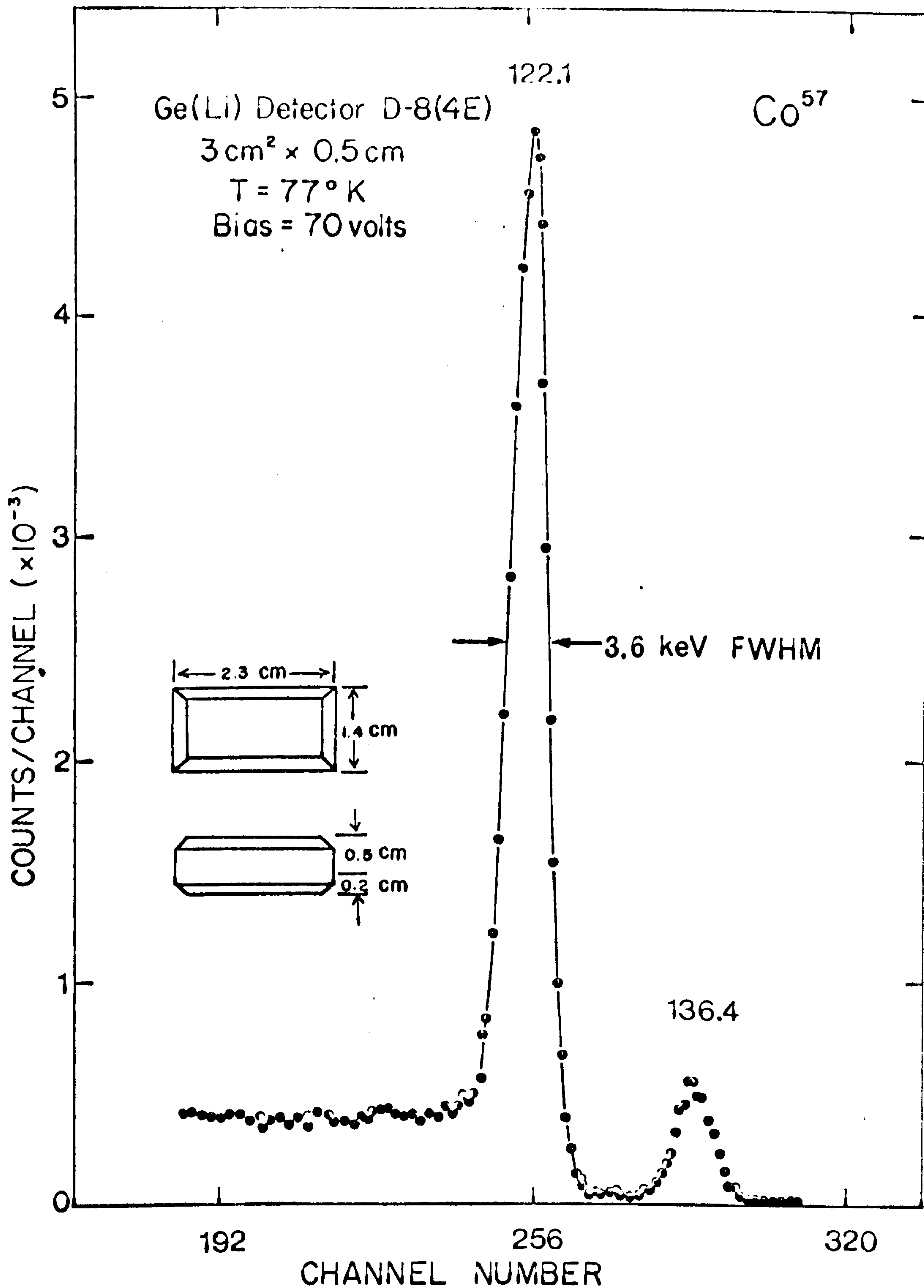

FIGURE 31

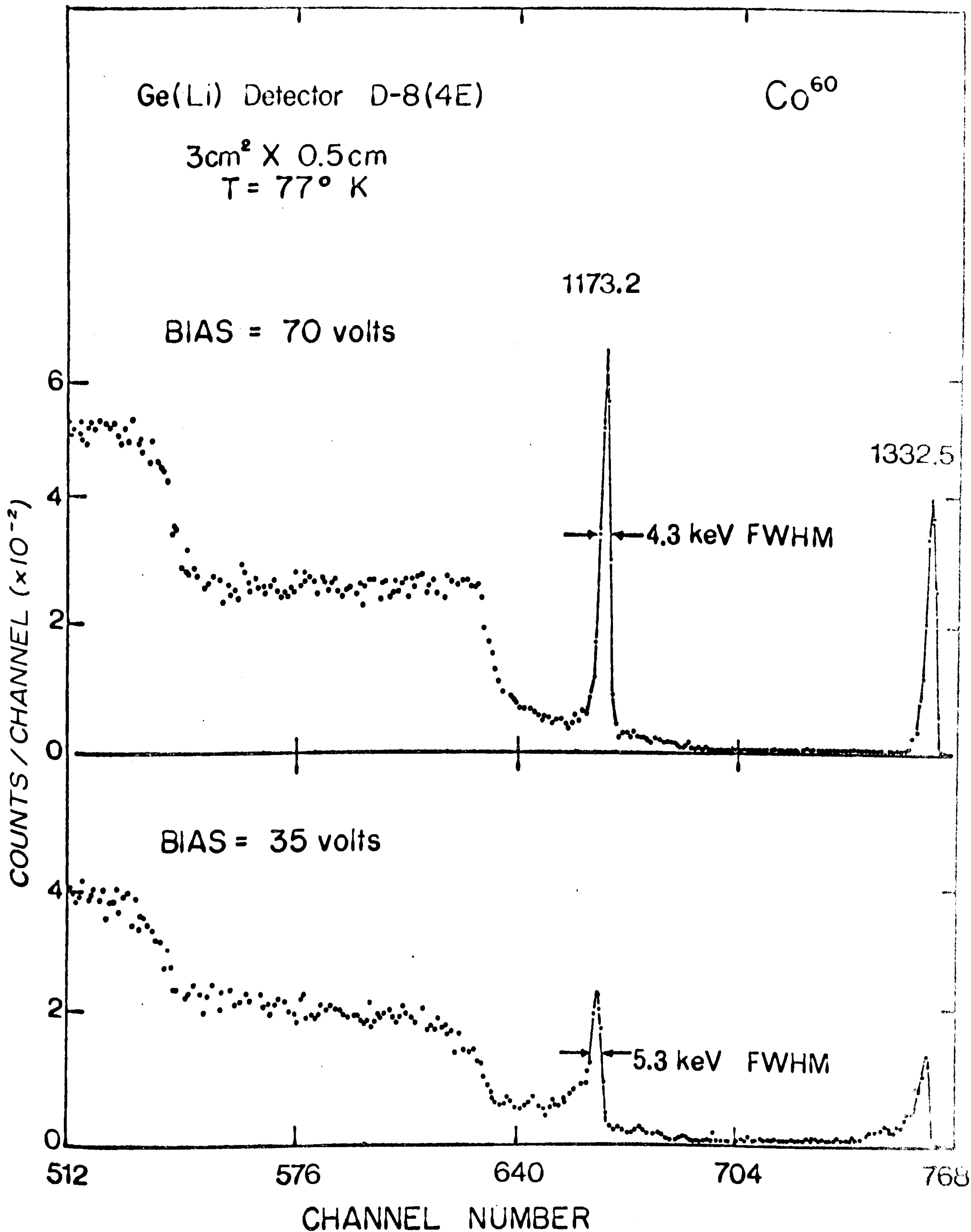

FIGURE 32

capacitances (approximately 12 pf) and leakage currents, showed that the detector with the bevelled edges had superior resolution over the detector with rectangular geometry by a factor of almost 2. Figure 33 shows the equipotential lines obtained by plotting the field on a conducting-paper model of the device with bevelled edges, assuming the full potential drop occurs across the i-region. Since the configuration of the collection field in this diode would be such that the field near the surface is weaker than in the center, the superiority of the bevelled-edge device might be attributed to the minimization of the effect of surface trapping centers. Llacer[71] has reported the use of various geometrical configurations in controlling surface leakage current in Si(Li) detectors.

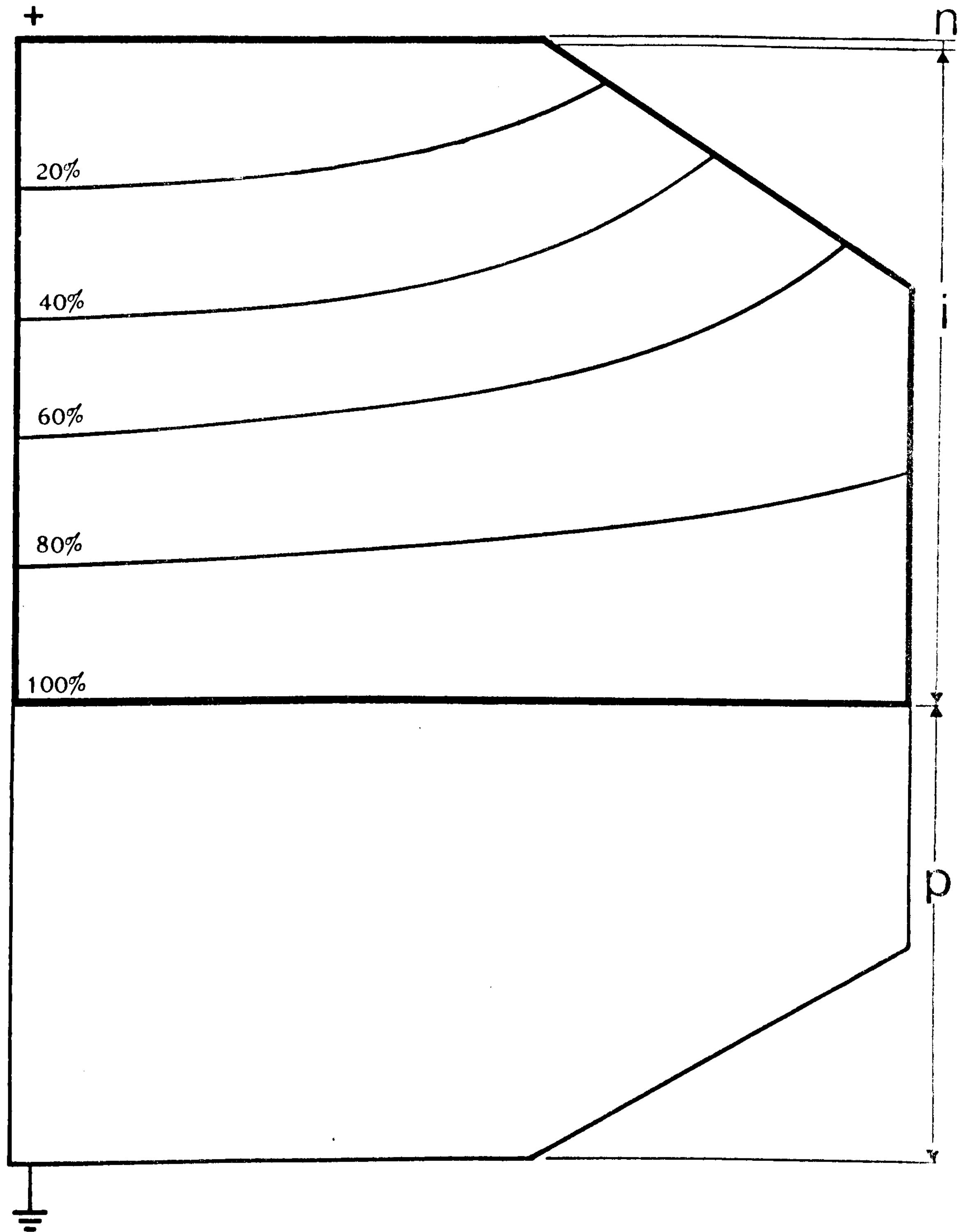

FIGURE 33: PLOT OF EQUIPOTENTIAL LINES FOR ELECTRIC FIELD ACROSS i-REGION OF Ge(Li) DETECTOR WITH BEVELLED EDGES.

CHAPTER V

OPERATING CHARACTERISTICS of Ge(Li) DETECTORS

5. We can summarize the principles of the operation of a Ge(Li) detector with the aid of Figure 34 which shows a schematic representation of the cross-section of a planar p-i-n diode. Also shown are representations of the various possible gamma-ray interactions with the detector: (a) is a low energy gamma-ray which undergoes a photoelectric interaction in the detector, losing all its energy in the production of the photoelectron and an x-ray both of which are absorbed in the crystal, thus contributing to a full-energy peak in the pulse-height spectrum; (b) represents a gamma-ray which loses all its energy within the detector by a series of Compton interactions and a final photoelectric interaction, also contributing to a full-energy peak; (c) is a gamma-ray which undergoes a few Compton interactions within the crystal while the last Compton-scattered photon escapes; thus this gamma-ray (c) results in an event in the Compton escape continuum; gamma-ray (d) interacts with the detector in a pair-production event, the subsequent 511-keV quanta from annihilation of the positron escaping the detector, so that an event contributing to a double-escape peak is registered.

5.1 <u>Ge(Li) Detector Response</u> The response of a Ge(Li) detector to gamma-rays is shown in Figure 35, a pulse height spectrum of gamma-rays from the decay of Na^{24} obtained with an 8 cm^3 detector fabricated in the present work. An ORTEC model 118A FET pre-amplifier operating at room temperature, a Tennelec TC-200 main amplifier with 0.8 integrating and

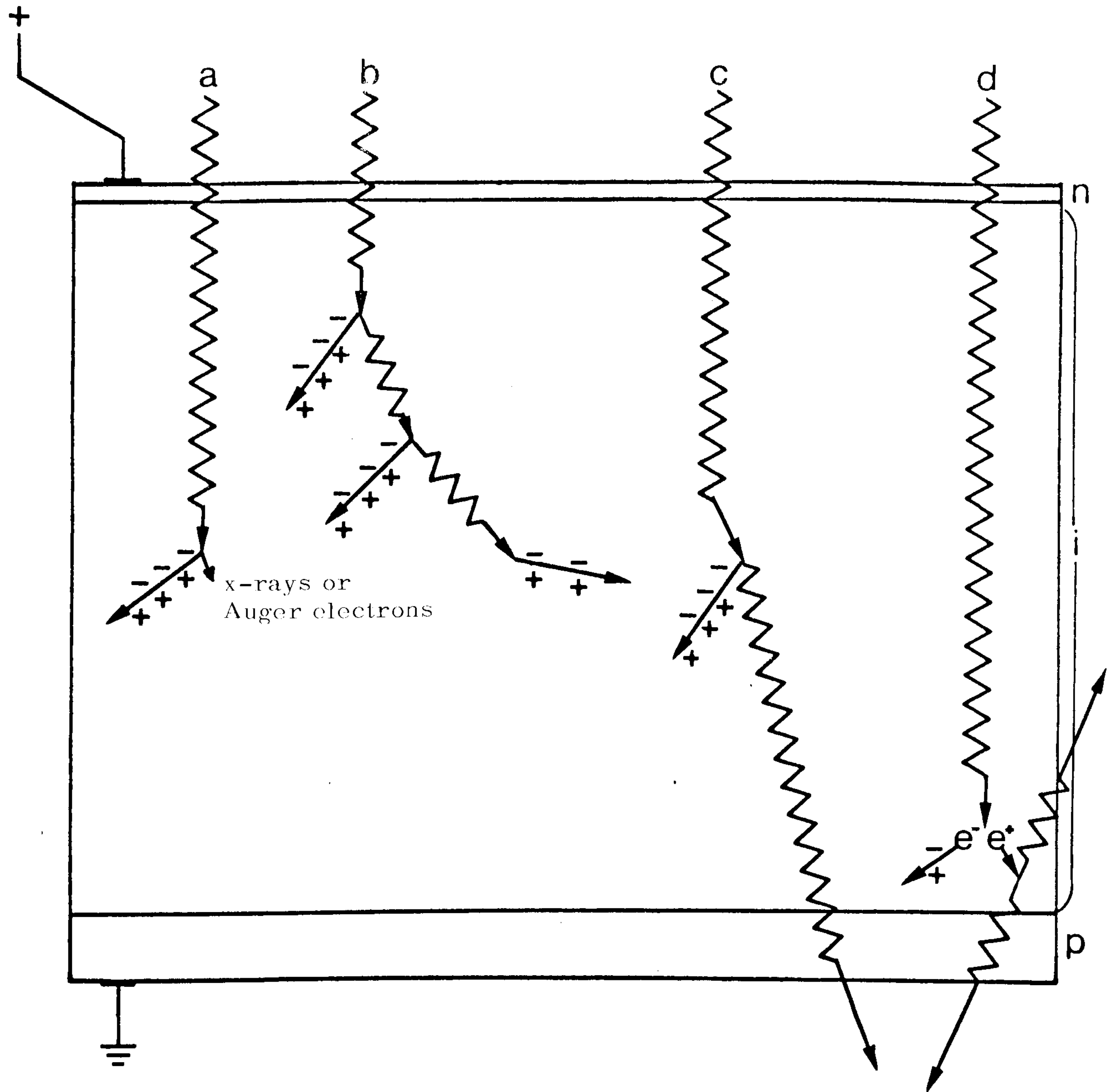

FIGURE 34: CROSS SECTION OF A Ge(Li) DETECTOR SHOWING THE INTERACTION OF GAMMA-RAYS WITH THE DETECTOR:

(a) PHOTOELECTRIC INTERACTION

(b) COMPTON INTERACTION WITH TOTAL ENERGY DEPOSITED IN THE DETECTOR

(c) COMPTON INTERACTION WITH ESCAPE OF A COMPTON-SCATTERED PHOTON

(d) PAIR-PRODUCTION WITH ESCAPE OF THE TWO ANNIHILATION QUANTA.

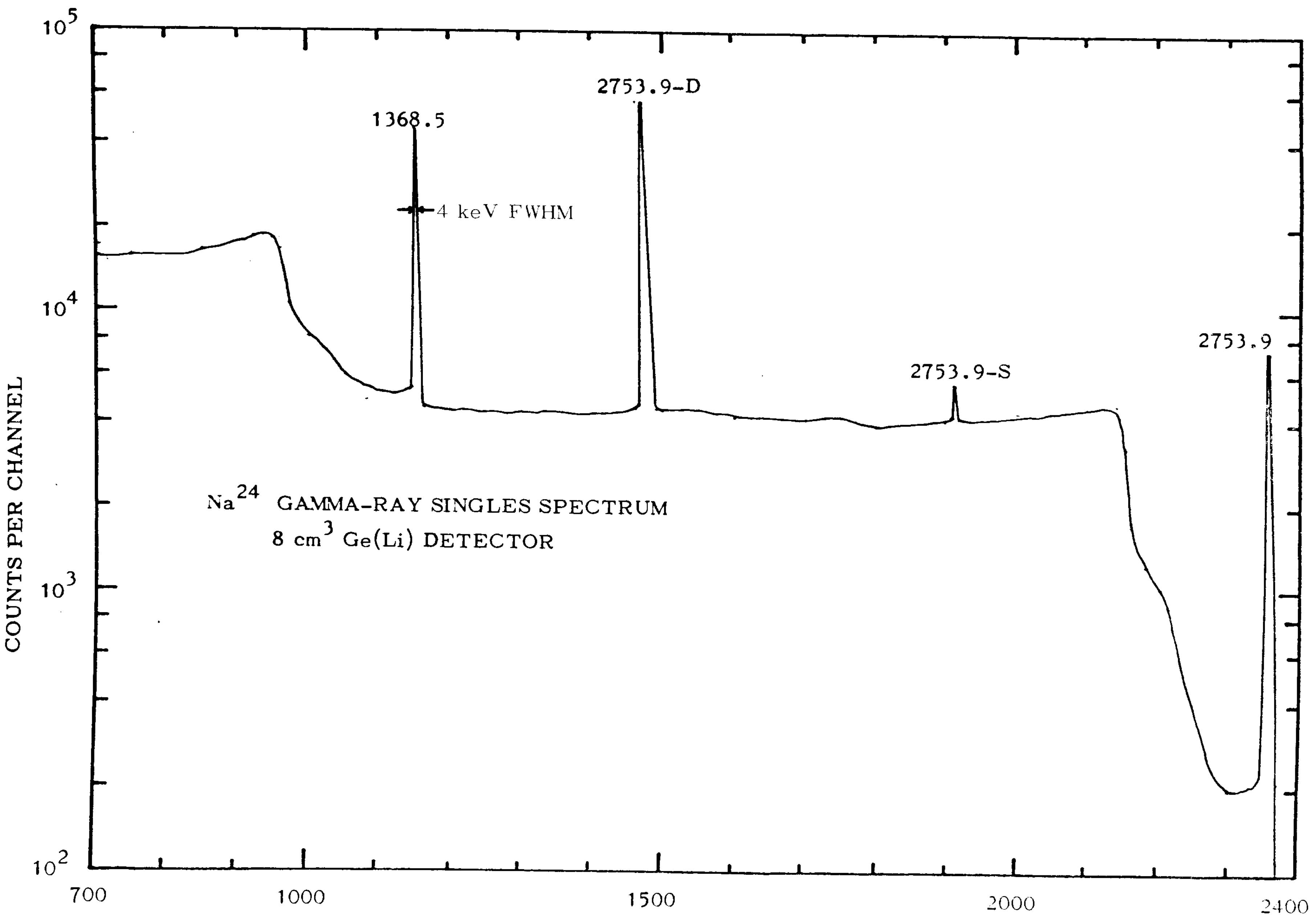

FIGURE 35

1.6 microsecond differentiating time constants, and a Victoreen SCIPP 104TP pulse-height analyzer were used to record the spectrum in 3200 channels. Prominent features of the spectrum include the full energy peaks at 1368.5 and 2753.9 keV corresponding to the gamma-rays from decay of Na^{24}, the double- and single-escape peaks of the 2753.9 keV gamma-ray at energies of 2753.9 - $2m_oc^2$ and 2753.9 - m_oc^2, respectively, and the so-called Compton "knees" located below each full energy peak.

Since gamma-rays of the above energies interact with germanium predominantly by Compton scattering (see Figure 11), the full energy peaks at 1368.5 and 2753.9 keV originate mainly from the absorption in the detector of electrons produced in the multiple Compton interactions, i.e., gamma-rays which deposit all their energy in the detector irrespective of the number of interactions register events in the full energy peak. The escape-peaks originate from pair-producing interactions in which either one or two quanta of annihilation escape from the sensitive volume of the detector. Because of the statistics of charge production and collection, full energy and escape-peaks are not registered as lines but as Gaussian-distributions ; amplifier noise also contributes to the peak width.

The minimum energy for a Compton-scattered photon as seen from equation 2-4 for $\theta = 180^o$ is $E'_\gamma = \frac{1}{2}m_oc^2$; thus the maximum energy of the corresponding Compton electron is $E_e = E_\gamma - \frac{1}{2}m_oc^2$ from equation 2-5. Theoretically, then, one would expect the detector response for those Compton interactions in which some of the Compton-scattered photons escape the detector to show no events in the energy region between E_γ and $E_\gamma - \frac{1}{2}m_oc^2$ (E_γ - 205.5 keV) and a continuous distribution below this energy, a peak occuring in the distribution at the energy corresponding to maximum energy of the Compton electron.[54] The actual distribution seen in a Ge(Li) pulse-height spectrum is smeared somewhat at the Compton

peak ("knee") due to charge production and collection statistics and becomes less sharp as the energy increases (see Figure 35). With increasing photon energy, the probability of the Compton electron escaping the detector increases, and, depending on detector volume, the Compton "knee" gradually disappears into the background continuum.[62]

5.2 Detector Efficiency The use of Ge(Li) detectors as gamma-ray spectrometers requires a knowledge of the efficiency for detection of full-energy events. The detection efficiency for double-and single-escape events is also useful in identifying such peaks with respect to the corresponding full-energy peak.

In the present work, a constant geometry source mount has been devised (see Figure 36) so that radioactive sources could be counted at reproducible distances from the detector. Using this arrangement, the largest geometrical solid angles which could be obtained with the smallest (0.85 cm^3) and largest (8 cm^3) detectors used were 0.6% and 8%, respectively.

5.2.1 Full-Energy Peak Efficiency The full-energy peak detection efficiency for several Ge(Li) detectors has been determined using gamma-rays from standard sources of Co^{60} calibrated with a 3 x 3" NaI(Tl) detector and total counting efficiency and peak-to-total ratio data for scintillation detectors due to Heath.[50] The areas of peaks obtained in the Ge(Li) spectra were determined by summing the number of counts in each channel defining the peak and subtracting a linearly interpolated background. The shapes of the efficiency curves were checked by calculating relative gamma-ray intensities for a Co^{56} source.

Figure 37 shows intrinsic full-energy detection efficiency data for detectors of various sensitive volumes. The two curves for which

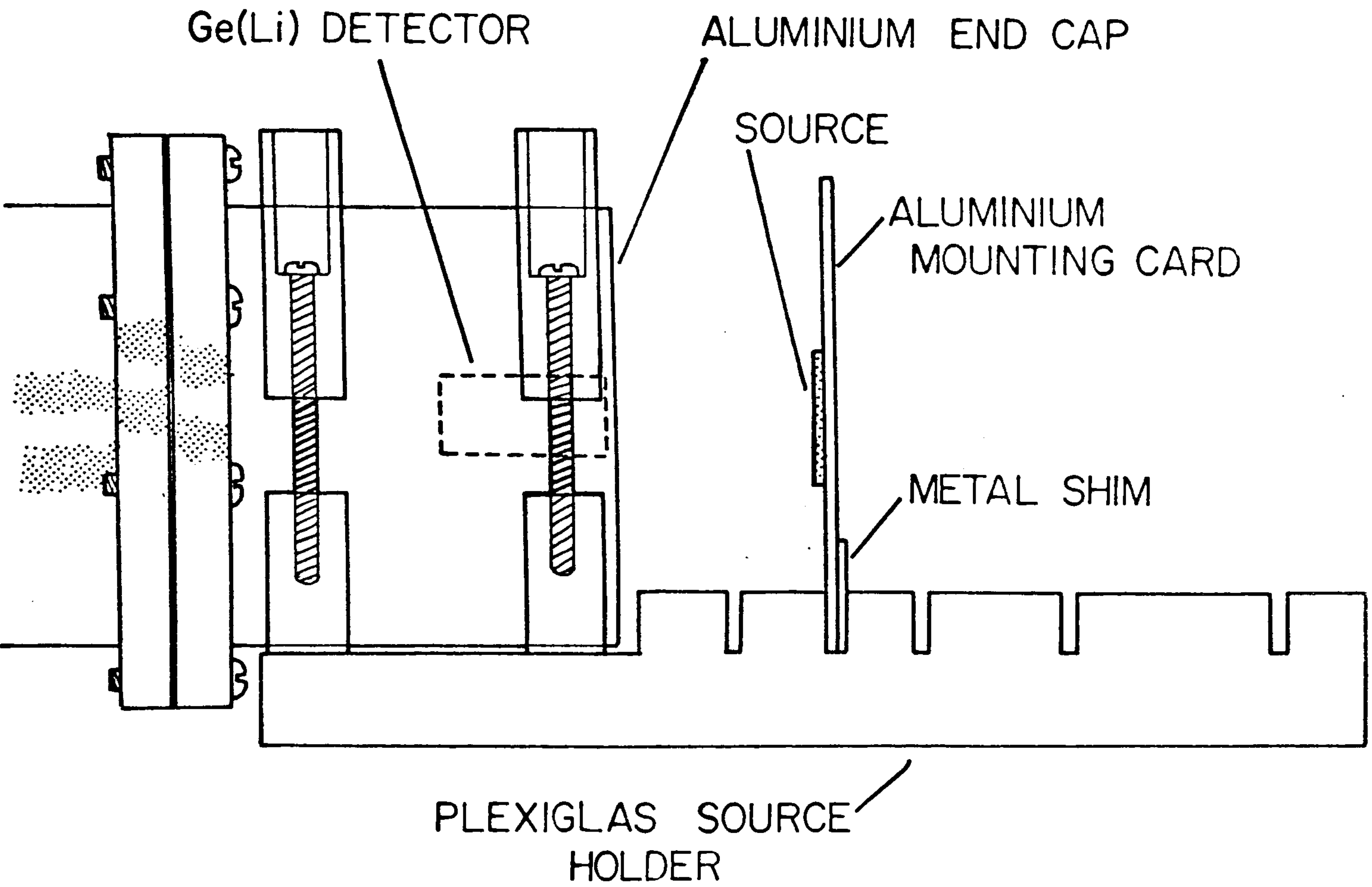

FIGURE 36: CONSTANT GEOMETRY SOURCE HOLDER

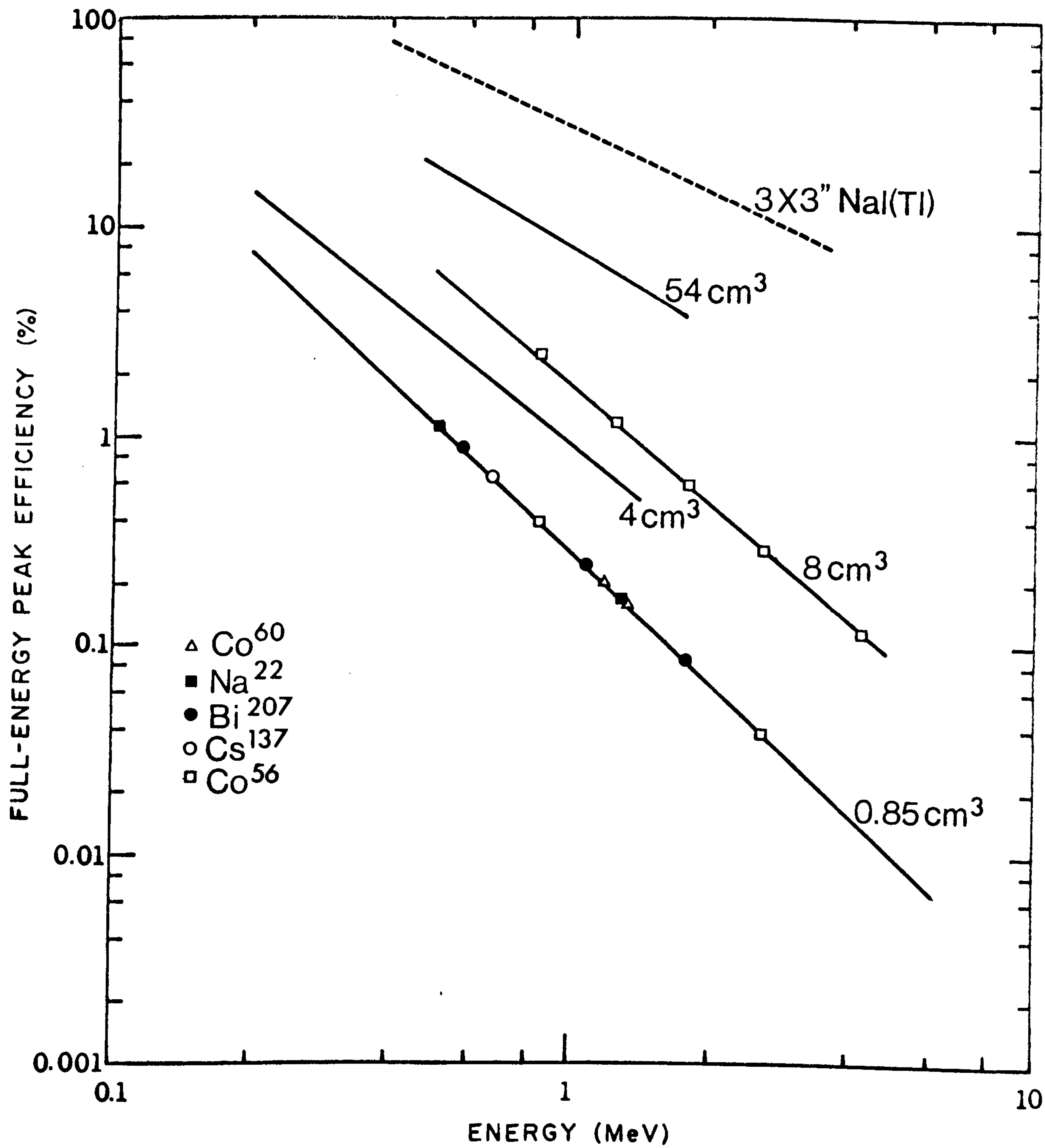

FIGURE 37

experimental points are shown (detector volumes of 0.85 and 8 cm^3) are from the present work; the linear relationship between the logarithms of efficiency and gamma-ray energy as observed by Easterday, et.al.,[38] is seen to hold at least to 3500 keV, which was the limit of the gamma-ray energy used in the Co^{56} measurements. The full-energy efficiency for a 3 x 3" NaI(Tl) detector is shown for comparison with the Ge(Li) detectors.

An interesting result obtained during the course of this work is shown in Figure 38 in which are plotted full-energy efficiency data for three Ge(Li) detectors. The solid points and curve were obtained for a 1.7 cm^2 x 0.5 cm detector used in this laboratory, the squares are from the Monte-Carlo calculations of de Castro Faria, et.al.,[35] for a 1.8 cm diameter x 0.35 cm thick right circular cylindrical detector, and the triangles represent data of Ewan and Tavendale[39] for a 2.5 cm^2 x 0.35 cm device. The efficiencies are virtually indistinguishable, and it is interesting to note that the three detectors have almost identical volumes, 0.85 cm^3, 0.9 cm^3, and 0.88 cm^3, respectively. (The data also show the decrease in efficiency below 100 keV due to absorption of low energy gamma-rays by the end-cap of the cryostat and the 200-500 micron thick lithium-diffused dead layer).

Further evidence for the dependence of the full-energy efficiency on detector volume is shown in Figure 39; data for 18 Ge(Li) detectors taken from previously published work are shown plotted as full-energy efficiency at 1 MeV vs detector volume. Even though these detectors are of various shapes, rectangular or cylindrical, and of planar or coaxial configuration, there is seen to be a strong correlation between efficiency and detector volume, at least below 20 cm^3. Also shown are data from the Monte-Carlo

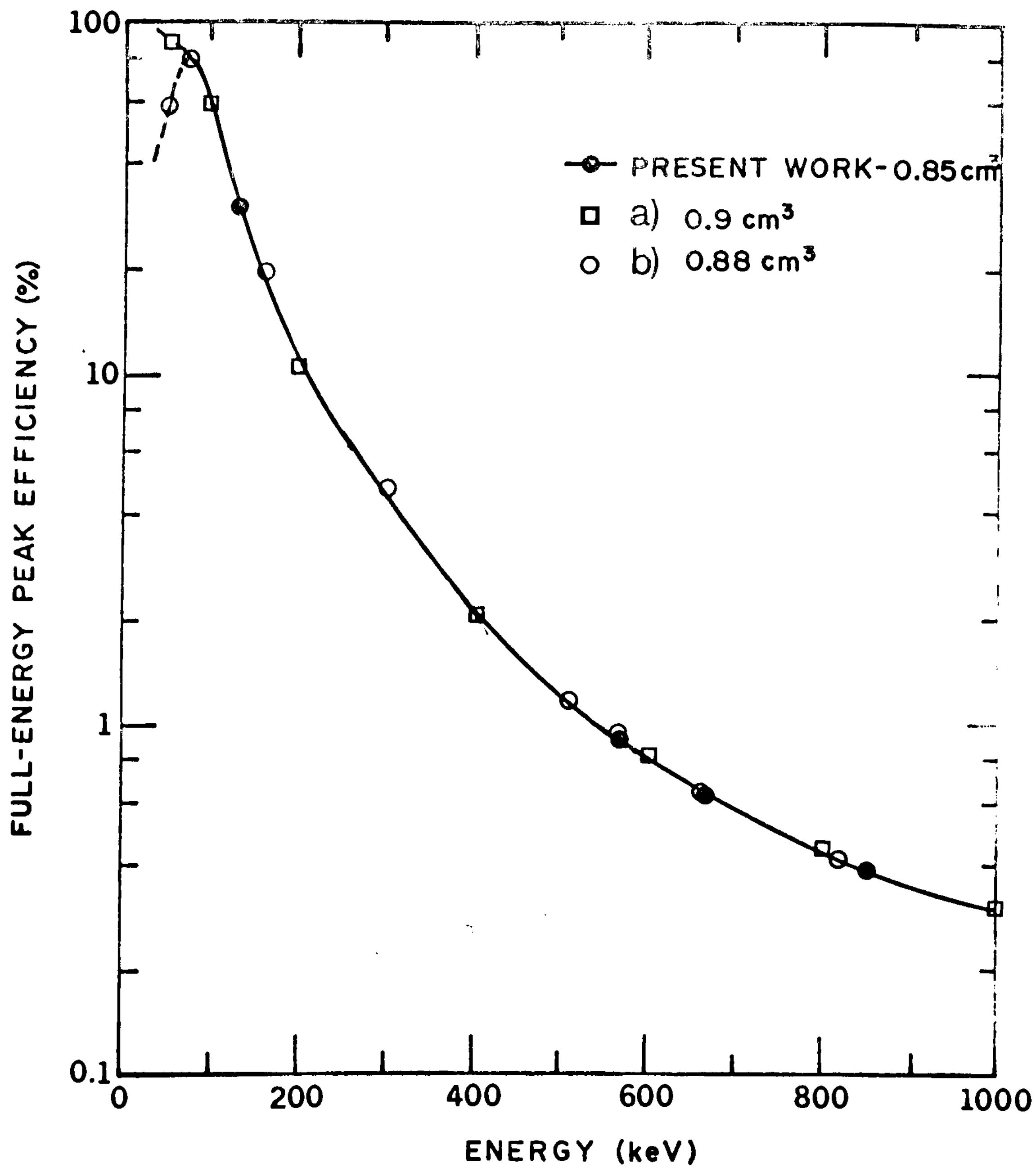

FIGURE 38

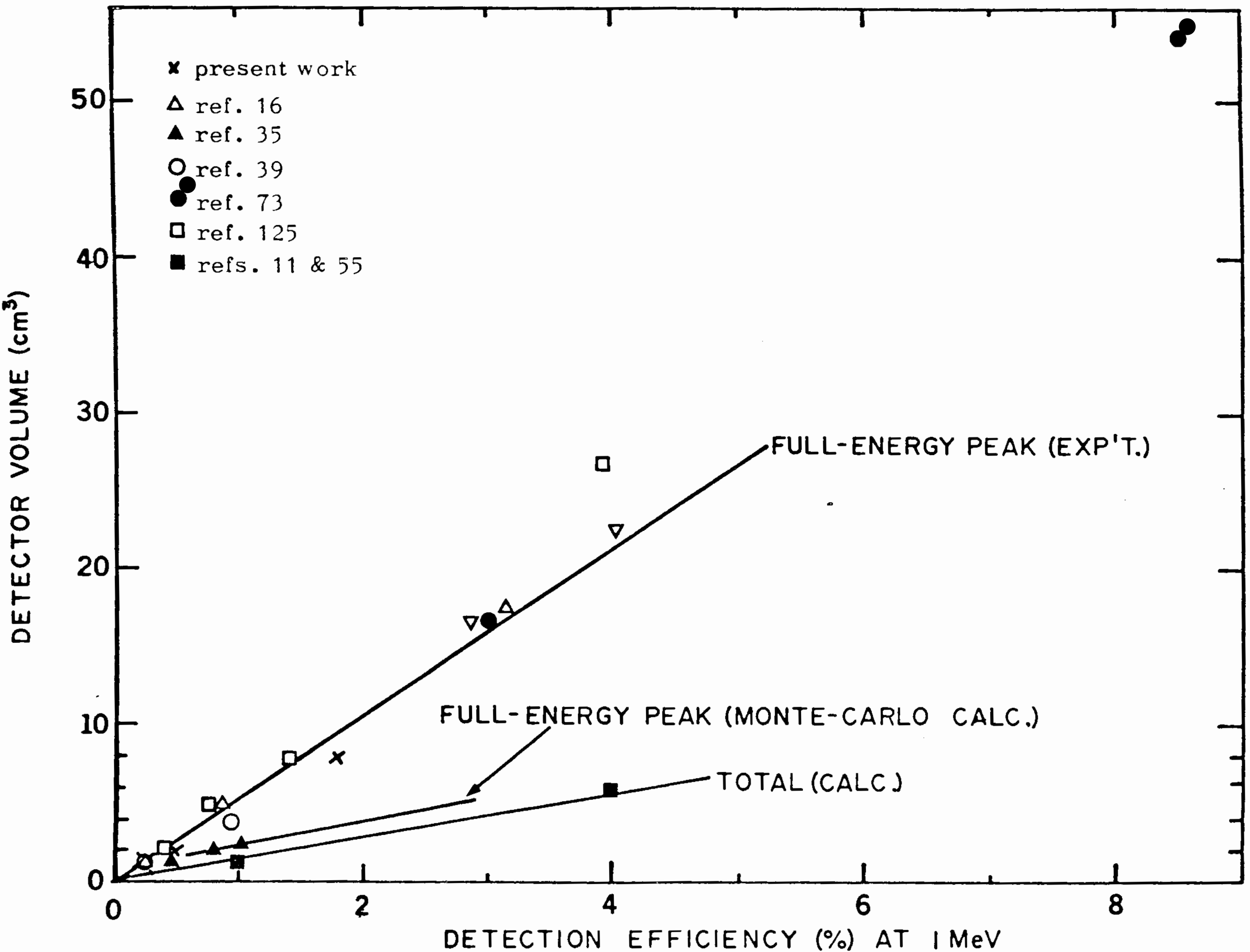

FIGURE 39

calculations of de Castro Faria, et.al.,[35] which do not follow the experimentally obtained points with increasing volume. Further data are shown for computations made for the total counting efficiency for square-planar detectors[55] and cylindrical devices[11]; both these data and the experimental points pass through the origin (where a detector with zero volume has zero efficiency), whereas the Monte-Carlo efficiencies do not. Furthermore, the Monte-Carlo data exhibit the same slope as the total counting efficiency data. This might indicate some error in accounting for full-energy-to-total counting factors in the Monte-Carlo computation.

5.2.2 Escape-Peak Efficiency The size and shape of a Ge(Li) detector determines the amount of reabsorption of annihilation quanta in the detector after a pair-producing interaction by a high energy gamma-ray. In general, the smaller the detector volume, the more enhanced are the intensities of escape events in a pulse-height spectrum; however, the ratio of detector dimensions also has direct bearing on escape-peak intensity. Mann, et.al.,[76] has shown that an increase in the surface-to-volume ratio of cylindrical detectors led to an enhancement of escape-peak intensities. If one dimension of a detector is much smaller than other dimensions, the above result obtains.

Figure 40 shows data for two detectors used in the present work and one used by Freedman, et.al.;[43] the ratios of the double-escape to full-energy peak areas and double-escape to single-escape peak areas are plotted against gamma-ray energy. The intensity of double-escape events is enhanced in the 8 cm^3 detector over the 2.3 cm^3 device due to the fact that the larger device has one dimension smaller than the others. The ratio of double-escape to single-escape areas is observed to be constant.[43,62]

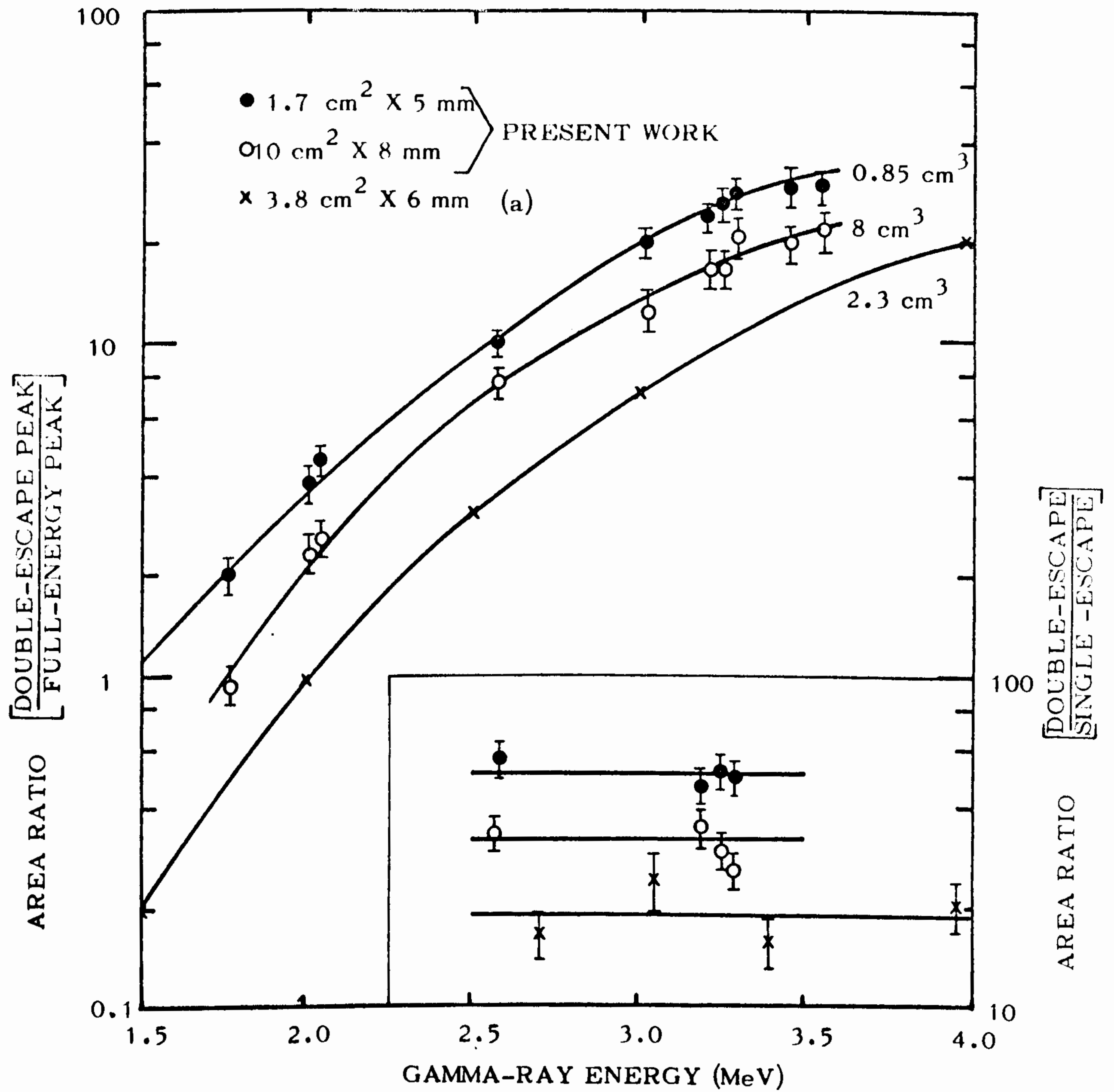

FIGURE 40

The ratios of escape- and full-energy peak areas are extremely useful relationships in nuclear spectroscopic applications. Along with the energy relationships between escape- and full-energy peaks, the area ratios for a particular detector serve as a means for confirming the intensity relationships between corresponding full-energy peaks. The intensity of the full-energy peak can be obtained from the area of the double-escape peak, for example, by the relationship:

$$I = (A_{DE}/R)/\eta_{FE} \qquad (5\text{-}1)$$

where I is the intensity of the full-energy peak, η_{FE} is full-energy detection efficiency, A_{DE} is the double-escape peak area, and R the ratio of double-escape to full-energy peak area.

5.3 Resolution and Fano Factor We recall that when monoenergetic radiation is brought to rest in a detecting medium, the standard deviation in the number of ionizations per incident particle is not equal to the square root of that number due to the correlation in the processes resulting from the constraint that each particle must lose exactly its initial kinetic energy in the medium.[41] The observed energy resolution of gamma-ray peaks in pulse-height spectra in keV at full peak width at half the maximum height is

$$\mathrm{FWHM} = 2.355\sqrt{E\epsilon F}. \qquad (2\text{-}10)$$

In order to compare resolution obtained with any specific Ge(Li) detector with the intrinsic resolution obtainable with such devices, one requires a value of the Fano factor F for germanium. Experimental determinations of F are extremely difficult using Ge(Li) detectors. Since the Fano factor is associated only with the charge production process, and

measurements obtained with Ge(Li) detectors are also influenced by the charge collection process, all of the effects which contribute to the line broadening due to the latter process must be accounted for; otherwise the experimental estimate of the Fano factor will be too large. Mann and collaborators[74,75] have considered the following factors which can contribute to the line width:

a) electronic noise of the detector/pre-amplifier system, which may dominate at low gamma-ray energies;

b) electronic drift, i.e., gain instabilities in the amplifier, analyzer, etc.;

c) gain shifts due to high count rate;

d) statistics of carrier recombination;

e) statistics of carrier trapping; and,

f) risetime, i.e., the statistics of the collection time of generated electron-hole pairs.

Factors d), e), and f) will, in general, depend upon the applied electric field in a systematic manner. Variations in the detector field will also affect a) through changes in detector capacitance and leakage current.

5.3.1 Method for Determining Fano Factor The procedure used in attempting to evaluate the Fano factor was essentially that of Mann, et. al.[75] Pulse-height spectra were obtained with 0.85 cm^3 CaF_2-coated Ge(Li) detector and the associated electronics described earlier, using Co^{57}, Ba^{133}, and Co^{60}. In order to obtain a measure of the noise contribution of the electronic systems, a test pulse from a Berkely Nucleonics Corporation RP-2 pulse generator was fed to the pre-amplifier during the counting period; the test pulse is subject to all line broadening effects of the system except the effects due to charge production and collection in the detector.

Thus the intrinsic line width due to the detector alone can be obtained from a subtraction in quadrature of the test pulse line width from the gamma-ray line width:

$$N_d^2 = N_t^2 - N_s^2 \tag{5-2}$$

where N_d is the noise contribution of the detector in keV, N_t is the noise contribution of the total system in keV, i.e., the measured resolution (FWHM) of the gamma-ray peak, and N_s is the noise contribution of the electronics alone, i.e., the resolution (FWHM) of the test pulse peak. Short counting periods and low count rates were used in order to minimize gain shifts as previously outlined, although gain shifts had not been observed in other experiments for counting periods of up to 48 hours.

5.3.2 Experimental Results Figure 41 shows the results obtained for 4-6 runs at each bias setting for the 122 keV peak of Co^{57}; N_d^2 in keV (FWHM) as obtained from equation 5-2 is plotted against the reciprocal field 1/E $(kV/cm)^{-1}$. As Mann, et.al.,[74,75] observed there is a reduction in the detector resolution as the field is increased until a plateau is reached where negligible reduction in N_d^2 is obtained with increasing collection field. In this region a value of $F = 0.11 \pm 0.05$ was obtained, using equation 2-10 and $\epsilon = 2.98$ eV.[3] Figure 42 shows data obtained with the 0.85 cm^3 detector for the 1173-keV gamma-ray of Co^{60} and also results at 122 keV for the 8 cm^3 detector; the variance-to-yield ratio is plotted vs reciprocal field strength. Some of the results of Mann, et.al.,[75] are also presented for comparison.

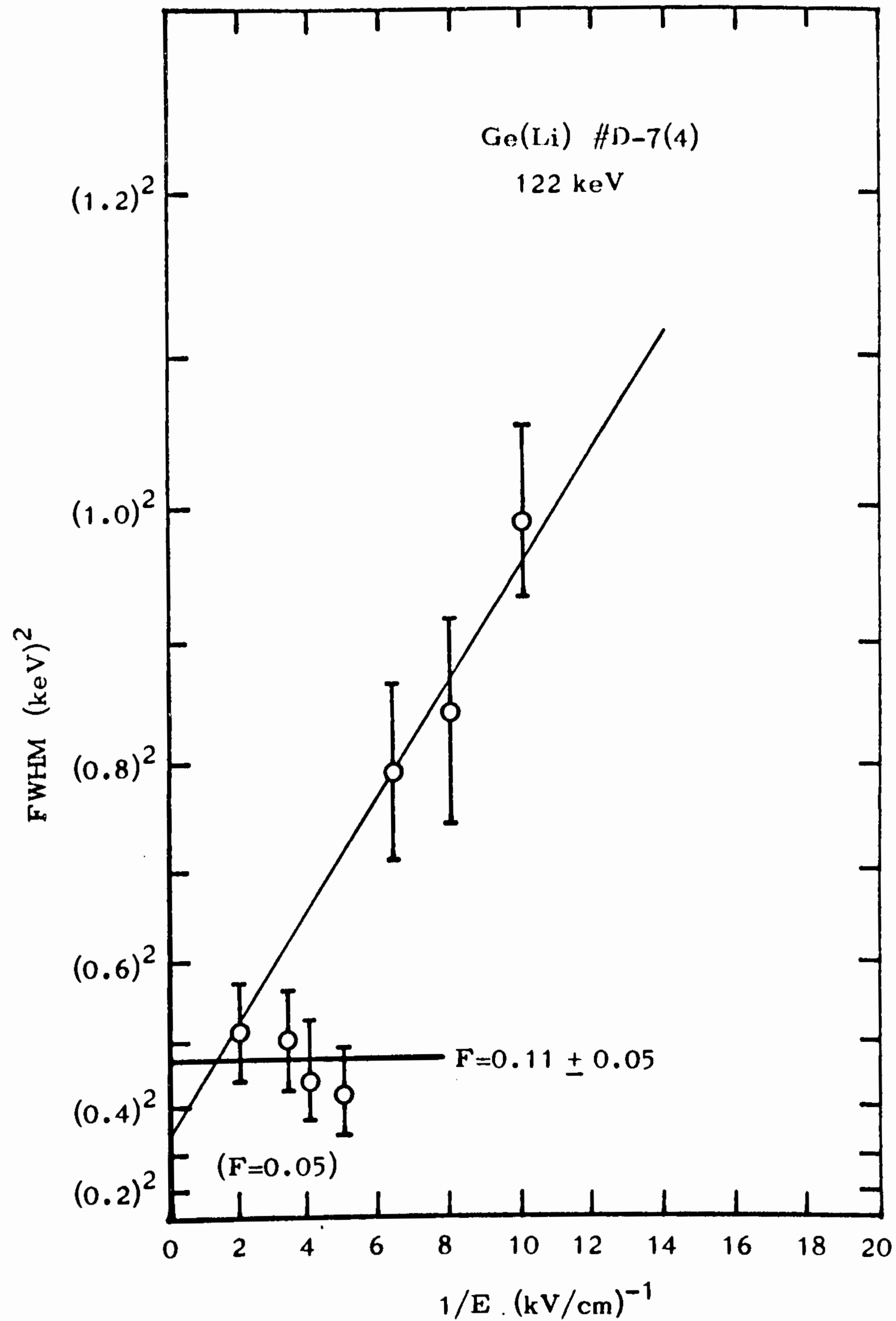

FIGURE 41

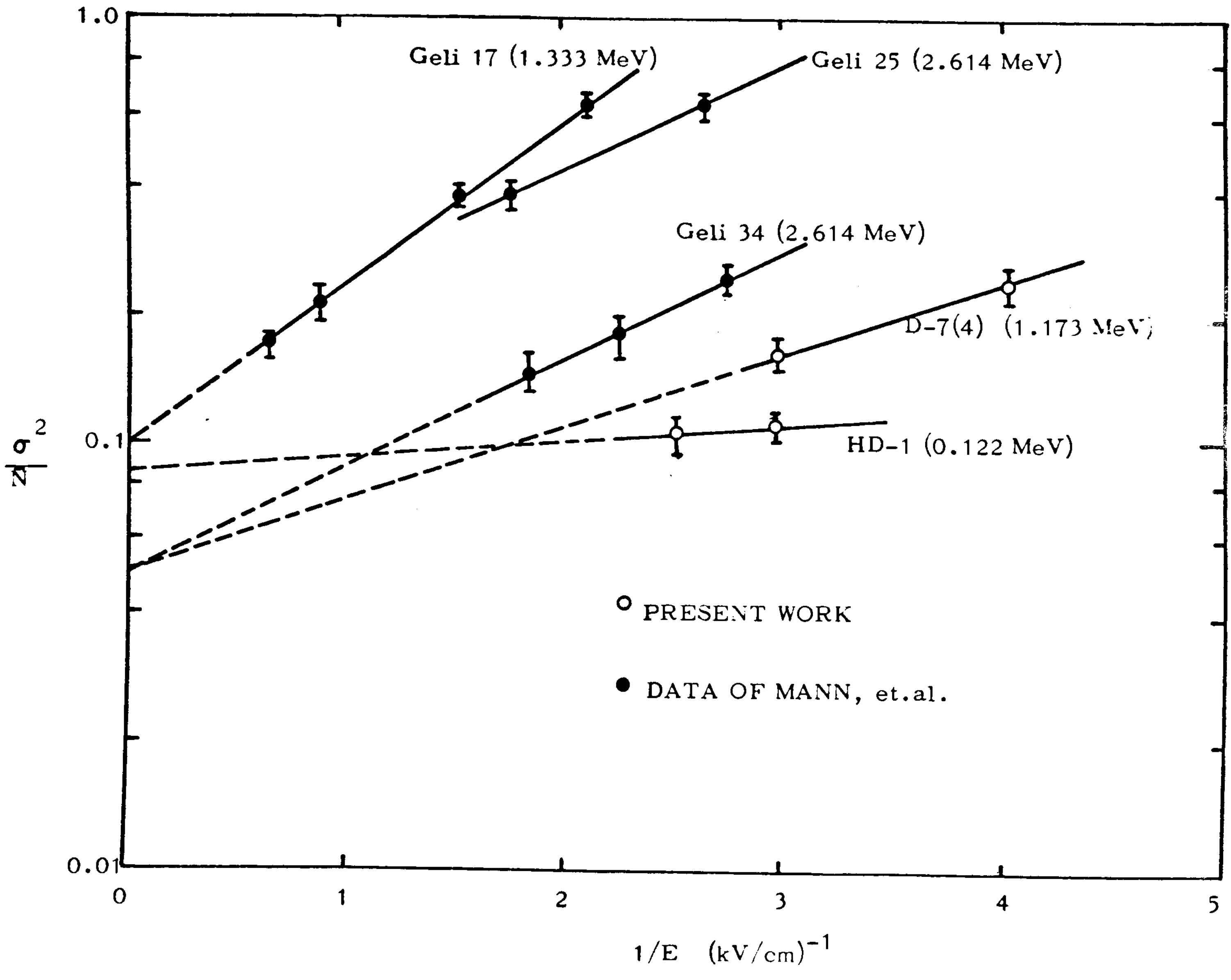

FIGURE 42

5.3.3 Discussion of Results From data like those shown in Figure 41, Mann, et.al.,[75] have inferred that in order to obtain a measure of the "intrinsic" Fano factor for germanium, one must extrapolate the data of Figure 42 to infinite field strength. This yields $0.05 \leq F \leq 0.1$ for the combined data shown in Figure 42.[75]

The extrapolation of the data to infinite field, it would seem, implies that there is some sort of intrinsic trapping in the detector so that complete charge collection can not be experimentally achieved, but rather some constant fraction of the charge is collected resulting in the plateau region as shown in Figure 41 for increasing electric field. It is the present contention, however, that while there is a limiting value of the charge collection efficiency obtained with increasing field, the value is near 100% over a wide range of collection fields; thus extrapolation to infinite field would not result in a value of the Fano factor very much different from that obtained from data such as in Figure 41.

Let us examine the behavior of the collection efficiency η with increasing field; Figure 14 presents η as a function of λ / w where $\lambda = \mu \tau E$ (equation 2-15). For a given Ge(Li) detector, the carrier mobility μ and lifetime τ are constant, thus λ is a function of E alone, w being constant for a given detector. From Figure 14 it can be seen that as E increases, η remains fairly constant then increases rapidly to a point (80%) and then approaches 100% collection efficiency asymtotically. Armantrout[6] has measured directly the charge collection efficiency and its dependence on collection field for a Ge(Li) detector and gamma-rays from Co^{57} and Co^{60} to yield the same result. The results of the present work and those of Mann, et.al.,[74,75] which show that at low gamma-ray energies a plateau is reached in the behavior of the variance-to-yield ratio with

increasing field, while as gamma-ray energy is increased the plateau appears only at high fields or not at all (Figure 42), can be explained as follows:

In the region where the collection efficiency increases rapidly with field, the variance-to-yield ratio will decrease in the same manner with increasing field. Where the collection efficiency levels off and approaches 100%, the ratio of variance-to-yield should approach a constant value, i.e., the plateau region of Figure 41. We must allow that for a given detector, the charge collection efficiency may not approach 100% but rather to some maximum value because of some inherent trapping in the device at the fields permitted by noise considerations. Since it is known[15] that higher energy gamma-peaks are more noticeably broadened due to incomplete charge than are low energy peaks (since a smaller fraction of the peak width of the former is due to pre-amplifier noise), this might explain the observations of the variance-to-yield ratio with field at higher gamma-ray energies (Figure 42). The behavior of the collection efficiency with mean free carrier path λ might also explain the different slopes of variance-to-yield vs reciprocal field observed for different detectors (Figure 42); λ is dependent upon the carrier mobility μ. Armantrout[5] has shown that differences in lithium drift-rate for different germanium samples could be correlated to differences in the electron mobility measured at 77°K; therefore, the different slopes observed might be due to variations in μ for each detector.

We now come to a portion of the data of Mann, et.al.,[75] in which measurements of the variance-to-yield ratio with the same detector for two different gamma-ray energies yielded $F = 0.13$ at 122 keV and $F = 0.20$ at 1173 and 1332 keV; both values of F were obtained from

the region where little change in the ratio of variance-to-yield was observed with increasing field. The higher energy gamma-rays will interact with the detector mainly by Compton scattering (see Figure 11); since the full-energy peak efficiency for a Ge(Li) detector is larger than that predicted from the absorption cross-section of germanium for higher energy gamma-rays,[39] some portion of the full-energy events in the spectrum must arise from the summing of multiple Compton scattering events. In a series of Compton interactions generated by a single incident gamma-ray, each primary (Compton electron) will have unavailable for the production of charge the energy corresponding to the minimum energy required to produce an ion pair E_i. Thus we may speculate that less of the incident gamma-ray energy goes into electron-hole pair production for Compton interactions which sum in the detector to yield a full-energy event in the pulse-height spectrum as compared to a photo-electric (single primary)* absorption at the same energy. With a slightly larger fraction of energy lost to the lattice in the interaction of high energy gamma-rays with the detector, the variance-to-yield ratio is increased (and thus the Fano factor) so that there appears to be an increase in the value of the Fano factor with increasing gamma-ray energy.

5.3.4 Conclusion In order to obtain a measurement of the Fano factor from Ge(Li) experiments, one must extrapolate the variation of the ratio of variance-to-yield with field to infinite field; however, we conclude that a linear extrapolation as shown in Figure 42 (semilog scale)[75] is invalid because of the behavior of the charge collection efficiency with increasing field. It appears that the most meaningful measurements of F will be obtained at low gamma-ray energies where the photoelectric interaction will dominate,

*Although a photoelectric event is multiple, most of the gamma-ray energy goes to the photoelectron.

and trapping contributions to the resolution minimized.

At 122 keV we obtain $F = 0.11 \pm 0.05$ for the 0.85 cm^3 detector, and 0.11 ± 0.04 (average of the two points) for the 8 cm^3 device. At this gamma-ray energy, Mann, et.al.,[75] obtained the value $F = 0.13 \pm 0.02$ using $\epsilon = 2.8$ eV; with $\epsilon = 2.98$ eV, $F = 0.12$ in agreement with the results of this work. Since the experimental work was not carried out with infinite collection fields on the detectors, these results represent an upper limit of F; however, because of the behavior of the collection efficiency with field, the value of the "intrinsic" Fano factor should not be much different from the above results. We also recall at this point, the calculation of Klein[61] for germanium at 77°K, $F = 0.11$.

Part Three

Experimental Application of Ge(Li) Detectors:

Nuclear Decay Studies

CHAPTER VI

SPECTROSCOPIC TECHNIQUES

6. Ge(Li) detector systems represent one of the best available compromises in terms of energy resolution, efficiency, and speed of data aquisition over other types of gamma-ray spectrometers.[53] The use of Ge(Li) detectors in nuclear spectroscopic applications enables the experimenter to obtain better resolution and more accurate energy determination than is possible with the more efficient NaI(Tl) scintillators; at the same time Ge(Li) detectors require less source activity than do the higher resolution spectrometers, such as the external conversion $\pi\sqrt{2}$ spectrometer, and permit simultaneous collection of data over the whole spectrum under study. This is not to say that the Ge(Li) spectrometer will replace all other types of devices in nuclear spectroscopy, but rather that the Ge(Li) detector has its place in filling the gap between the high efficiency, low resolution scintillators and the low efficiency, high resolution magnetic spectrometers.

In this part are presented certain nuclear decay studies undertaken using various Ge(Li) detectors fabricated during the course of the present work. The studies are presented mainly for their contribution to existing knowledge about the decay of the nuclei studied, but comparison can be drawn with previously published work using other gamma-ray spectrometry systems.

6.1 Single Detector Measurements Pulse-height spectra obtained using a single Ge(Li) detector, i.e., the "singles spectra," yield upon proper evaluation, accurate values for the energies and intensities of the

gamma-rays emanating from the source under study. The uncertainties associated with gamma-ray energy measurements depend upon the accuracy achieved in locating peak positions, non-linearities in the pulse-height to energy response of the system, and electronic drifts.[53] While the uncertainty in locating centers of peaks naturally depends upon factors such as counting statistics and peak shape, errors associated with this measurement can be minimized by using a conversion gain setting on the analyzer (number of keV per channel) so that many channels cover the peak. For example, if a conversion gain of 1 keV/channel is used in an experiment, an error of one channel in locating the center of a peak would lead to an error of approximately 1 keV in the energy determination.

At present, because there are few accurately measured gamma-ray energy standards which are convenient to use, the linearity of the Ge(Li) detector is relied upon heavily to yield accurate energy calibrations. Ewan and Tavendale[39] showed that the energy response of Ge(Li) detectors is linear from 0 to 2600 keV to within $\pm$ 0.3%, the accuracy of the pulse generator used for comparison; recently Levy and Ritter[67] have determined that the detectors are linear in energy response to less than 0.046% at energies up to 10 MeV. Non-linearities observed in the system are due in part to the associated electronics and must be suitably accounted for in order to obtain accurate results.

6.1.1 Location of Peak Positions In the present work, the channel number corresponding to the center of a peak was determined using a method of weighted averages of the form:

$$\bar{x} = \frac{\Sigma\, g_i x_i}{\Sigma g_i} \tag{6-1}$$

where $\bar{x}$ is the center of the peak (channel number), and the weighting factors g_i are the number of counts per channel in channel x_i. The error in determining the peak center channel number by this method is estimated to be between 0.2 and 0.4 channels, providing that many* channels cover each peak, a condition easily achieved using the SCIPP 104TP analyzer at conversion gains of less than 1 keV/channel over the range of 3200 channels. Freedman, et.al.,[43] claim comparable accuracies using a method of visual inspection of peaks containing 3-4 channels.

6.1.2 Energy Calibration and Computation The non-linearities in the amplifier and analyzer were not accounted for explicitly; the pulse-height vs energy response was fitted to a polynomial of the form:

$$E = A + Bx + Cx^2 + Dx^3 + \ldots \quad (6\text{-}2)$$

where E is the gamma-ray energy, x is the channel number, and A, B, C, and D are the parameters to be fitted. The non-linearity of the system may also be determined explicitly using a pulse generator (see for example ref. 43). In this method, two pulses of different amplitude are used to determine a straight line for the amplitude vs channel number response of the analyzer. The deviation (in number of channels) from this line of pulse amplitudes inside and outside the range of the two standard pulses is then determined. A plot of deviation in channel number vs channel number is obtained, and this correction is applied to each peak location. The linearity of the pulse generator determines the accuracy of this method.

In the present work, the source under study was counted simultaneously with suitable standard gamma-ray energy sources (see Appendix C); from the mixed spectra, energies of the most intense gamma-rays of the unknown

*greater than 3 or 4

source could be determined free of the ambiguities due to count rate variations. In subsequent measurements from which the standard gamma-ray sources were omitted, energy calibration of the weaker lines in the subject spectra was achieved relative to the more prominent ones previously calibrated.

The parameters to be determined in equation 6-2 were obtained by means of a least-squares fitting procedure to the calibration points, i.e., standard gamma-ray energy vs peak center channel number. The FORTRAN IV computer program which performs the fit to polynomials of degree 2 through 10 as specified, also computes the energies corresponding to channel numbers of peaks from the subject spectrum using equation 6-2 (see Appendix D). Table III shows the output of data for a Ge^{66} spectrum run on the SCIPP 104TP analyzer covering 3200 channels. The constants for the quadratic equation used in calibrating this run (a second degree polynomial was used in the majority of runs), A, B, and C are shown along with the energies E and channel numbers X of the standard gamma-rays. E CALC is the calculated value of the standard gamma-ray energy using the constants A, B, and C; the largest difference between a standard gamma-ray energy E and the computed value E CALC is approximately 0.2 keV. It can be seen that with B = 0.4 keV/channel, an error of ± 1 channel in locating the center of a peak yields a possible error of 0.4 keV in the energy. The coefficient C of the x^2 term in equation 6-2, i.e., the correction to a linear fit, is approximately 7×10^{-7} which amounts to a correction of about 6 keV at channel number x = 3000. For the Nuclear Data ND-160 analyzer used in some of the experiments, the maximum correction corresponds to about 10 keV at channel 1000, whereas Freedman, et.al.,[43] report corrections of 30 keV using the pulser technique to explicitly determine deviations from linearity. Table III also shows part of the data obtained for the gamma-rays of Ge^{66}.

TABLE III

DFO-7-SC1PP41K GE 66 X10 11.250.511.00 150V

0.287798595E 01 A

0.382637918E 00 B

0.721529432E-06 C

X	E	E CALC	
188.000	74.970	74.839	Pb K_{α_1} x-ray
214.000	84.800	84.796	Pb K'_{β_1} x-rays
311.500	121.970	122.140	Co^{57}
1324.500	511.006	510.948	Na^{22}
1477.000	569.630	569.608	Bi^{207}
1716.000	661.595	661.609	Cs^{137}
2758.000	1063.580	1063.681	Bi^{207}
3041.000	1173.226	1173.152	Co^{60}

CHANNEL NO.	E GAMMA	
109.000	44.594	
163.500	65.459	
236.500	93.412	(Ga^{67})
277.500	109.116	
467.500	181.919	

6.1.3 Gamma-Ray Intensity Determination Using the methods described earlier for calibrating the Ge(Li) detectors and determining areas of gamma-ray peaks, the gamma-ray intensities were calculated in the usual manner:

$$I(\%) = (A_i/\eta_i) \times 100 \qquad (6\text{-}3)$$

where I is the intensity, and A_i and η_i are the area and efficiency for the full-energy peak of gamma-ray i.

Freedman, et.al.,[44] reported difficulty in obtaining reproducible intensity measurements using Ge(Li) detectors, concluding that more accurate results could be obtained by experienced workers using NaI(Tl) detectors; Hollander,[53] however, is of the opinion that errors encountered in determining intensities with Ge(Li) detectors arise from using sources incorrectly calibrated by other spectrometers. Thus a major contribution to nuclear theory might be a re-evaluation of gamma-ray intensities by Ge(Li) spectrometers.[53] In the present work, problems in obtaining reproducible intensity measurements with several different Ge(Li) detectors were not encountered.

6.2 Measurement of Coincidences Between Two Gamma-Rays Coincidence measurements have been carried out to establish gamma-ray cascade relationships in the decay of Co^{56} using the two-parameter ("two-dimensional") technique exclusively. The equipment used has included a 3 x 3" NaI(Tl) detector with an ORTEC model 113 preamplifier and model 410 linear amplifier, the 0.85 cm^3 Ge(Li) detector with an ORTEC model 118 FET preamplifier and model 410 linear amplifiers, a Cosmic Radiations model 801 coincidence unit, and a Nuclear Data ND-160 multiparameter pulse-height analyzer equipped with an ND-160DG digital gates unit. Both timing

signals (fed to the Cosmic model 801 coincidence unit) and linear signals (fed to the multiparameter analyzer) were taken from the model 410 amplifiers operated in the double-RC clipping mode. Fast gamma-gamma coincidence signals from the coincidence unit initiated analysis of the linear signal from both detectors and amplifiers, following suitable attenuation and stretching.[19] A schematic of the equipment used is shown in Figure 43.

The analyzer was operated in the 256 x 16 mode, i.e., by digital address selection a portion of the spectrum seen by the Ge(Li) detector was stored in 256 channels in coincidence with 16 channels of the NaI(Tl) detector spectrum. Thus sixteen 256-channel Ge(Li) gamma-gamma coincidence spectra were obtained; these spectra contained contributions from both true and random coincidence events. Therefore a second identical set of experiments was performed with 400 nsec of delay introduced in the timing signal of one of the detectors. The spectra recorded under these circumstances corresponded to random coincidence events. The length of time chosen to store the random coincidence events must be such as to correct for the decay of the source during the original experiment from time $t = 0$ to $t = t_1$. Thus the random coincidence events were stored from time $t = t_1$ to $t = t_2$, where t_2 is found from the following relationship:[40]

$$t_2 = -\frac{1}{2\lambda} \ln[2e^{-\lambda t_1} - 1] \qquad (6\text{-}4)$$

where λ is the decay constant of the source under study. The condition $2\lambda t_1 < \ln 2$ must be satisfied so that t_2 will be a real number. Further details of the gamma-gamma coincidence analysis are given in the discussion of the results of the study of Co^{56} decay.

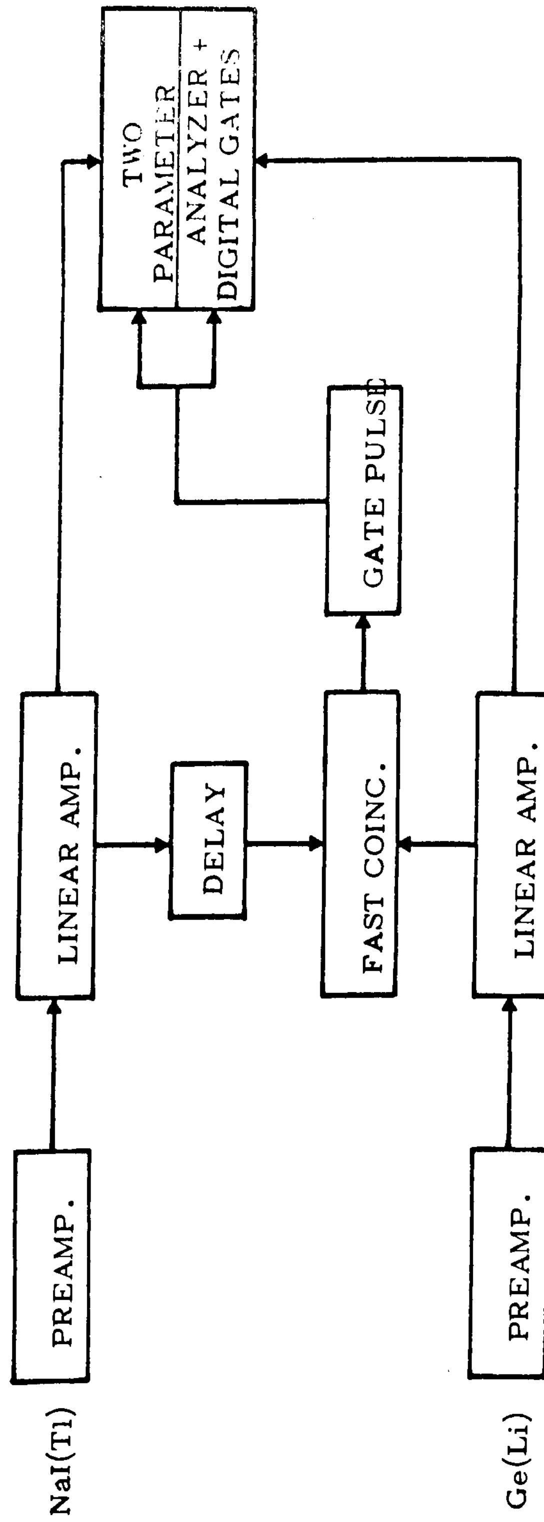

FIGURE 43

CHAPTER VII

NUCLEAR DECAY STUDIES

7. Several studies on the gamma-rays originating from the decay of certain nuclei have been made using Ge(Li) detectors. Of the studies undertaken, the decay of Co^{56} and Mn^{56} to levels in Fe^{56}, the decay of Ge^{66} to levels in Ga^{66}, and the preliminary results of the decay of Ga^{68} to levels in Zn^{68} are presented herein.

7.1 The Decay of Co^{56} and Mn^{56} [105] The study of the properties of the excited states in Fe^{56} is of interest from several points of view. One is the importance of the gamma-rays from the decay of Co^{56} as high energy standards in gamma-ray spectroscopy; another is the current understanding of the level density of nuclei in the low energy region.

The level structure of Fe^{56} has been extensively studied through nuclear reaction spectroscopy[8,13,58,72,98] and through studies of Co^{56} and Mn^{56} radioactivity.[7,9,37,93,95] The present work was begun to apply Ge(Li) detectors to the latter kind of study. During the course of this work, the results of Auble, et.al.,[7] and Dolan, et.al.,[37] appeared, displaying excellent agreement with the results of the present study obtained thus far. The present work was, however, continued since the detectors which had been used in it were of higher resolution than those used previously and offered the possibility of detecting expected but as yet unobserved transitions in Fe^{56}. Also the previous studies of gamma-gamma coincidences were relatively crude; improved coincidence studies were expected to permit the identification of gamma-ray cascades and confirmation of the placing of certain of the excited states required by previously published decay schemes.

7.1.1 Source Preparation Samples of Co^{56} were prepared through the $Fe^{56}(p,n)$ reaction by bombardment of natural iron targets with 10-MeV protons from the University of Washington cyclotron in Seattle. In samples thus obtained, the only impurity activities detected over an observation period of 18 months were 267-day Co^{57} and a small amount of 71-day Co^{58}; therefore, no chemical separation of cobalt activity was performed.

Samples of Mn^{56} activity were prepared by the irradiation of chemically pure manganese metal (100% Mn^{55}) with thermal neutrons from the Texas Nuclear Corporation model 9900 neutron generator of this laboratory. The purity of the Mn^{56} activity was determined via a half-life measurement; the decay of the radioactivity was followed with a gas-flow proportional counter (Figure 44), and the variation of activity with time analyzed by means of the CLSQ computer program due to Cumming.[25] A single decay period of 2.585 ± 0.001 hours was found, corresponding to better than 99.4% of the initial source activity; this half-life value is in agreement with literature values,[63] and confirms the purity of the Mn^{56} samples used. During the radiation measurements, sources were prepared periodically during the measurement period (approximately 72 hours) so that the counting rate was maintained within convenient limits.

7.1.2 Single Detector Measurements Four of the Ge(Li) detectors fabricated in this laboratory were used during the course of this work, the largest of which had an active volume of 8 cm^3. Most of the results reported here on the gamma-ray energy measurements were obtained with the 0.85 cm^3 detector protected from the ambient by a coating of CaF_2 (see earlier); gamma-ray relative intensity measurements reported represent weighted averages of results obtained using the four detectors. The electronic

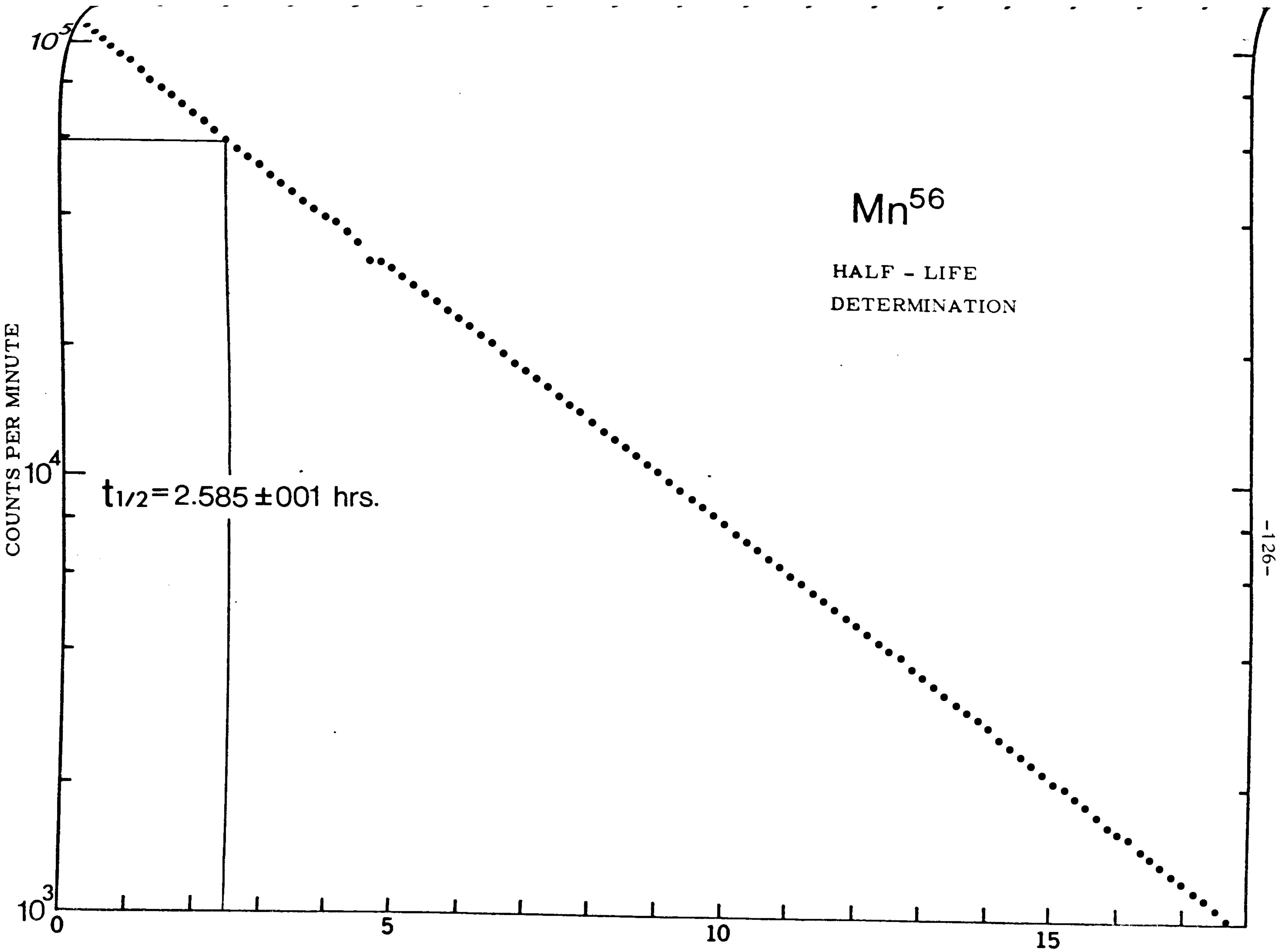

FIGURE 44

equipment which has been used was described earlier, and in addition, an ORTEC model 408 biased-amplifier was used in several of the gamma-ray singles spectra.

Figures 45 and 46 show Co^{56} single-detector gamma-ray spectra obtained by means of the biased-amplifier system. Spectra with an expanded energy scale covering energy regions of particular interest are shown in Figures 47, 48(a), and 48(b). The only peaks observed and not assigned to the decay of Co^{56} are the 122- and 136-keV peaks from the decay of Co^{57} (not shown) and the most intense gamma-ray from the decay of Co^{58} at an energy of 811 keV. In the present spectra, a previously unobserved peak at an energy of 3598.7 keV was detected; the double-escape peaks are resolved for the weak transitions of energy 1963.4, 2112.8, and 2213.0 keV which had not been observed in previous studies. The full-energy peak corresponding to the 2213.0-keV transition is also resolved from an adjacent peak; this transition had been observed previously only by MacDonald and Grace[72] by means of a triple-crystal pair spectrometer. Table IV summarizes the results of the present work for the Co^{56} gamma-ray energy and relative intensity measurements; results of previously published work obtained with Ge(Li) detectors[7] and internal conversion spectroscopy[93] are shown for comparison. The overall agreement is excellent; particularly in the relative intensity measurements, the results of Auble, et.al.,[7] and of the present work are in agreement to within 10% or better, except for the 978- and 3202-keV transitions. In no case is there disagreement outside the quoted uncertainties (standard deviations from the mean value in both studies.)

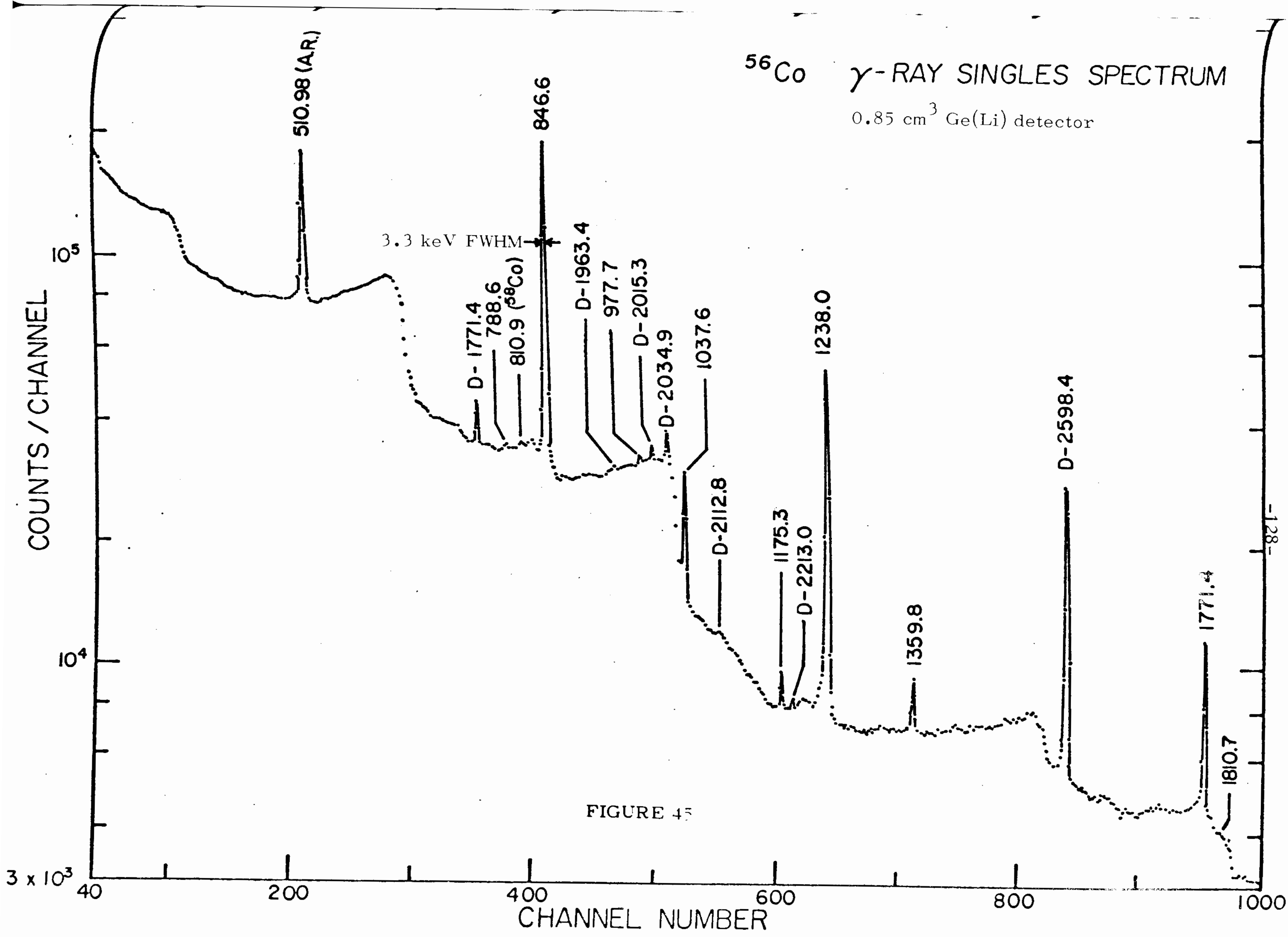

FIGURE 45

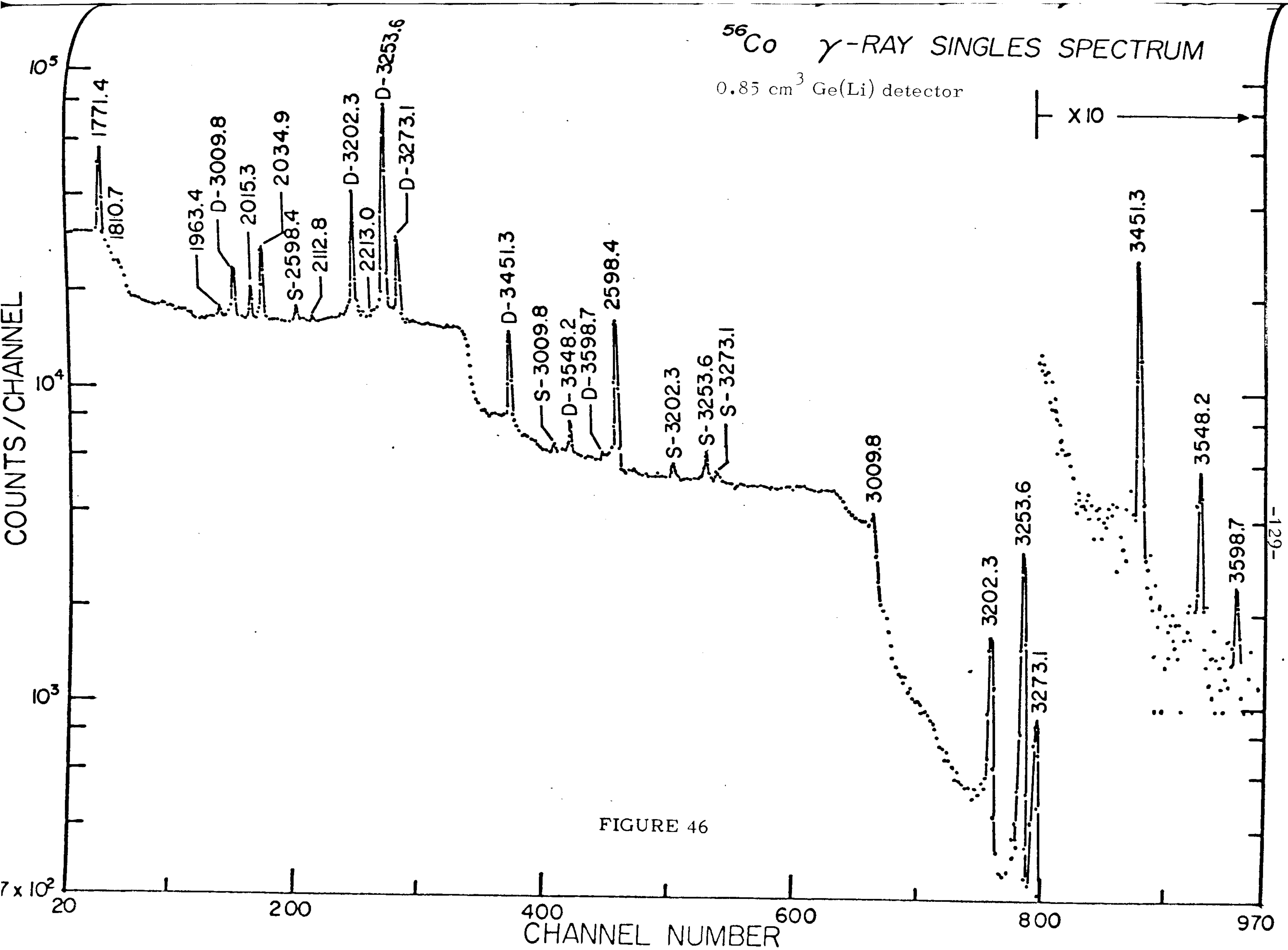

FIGURE 46

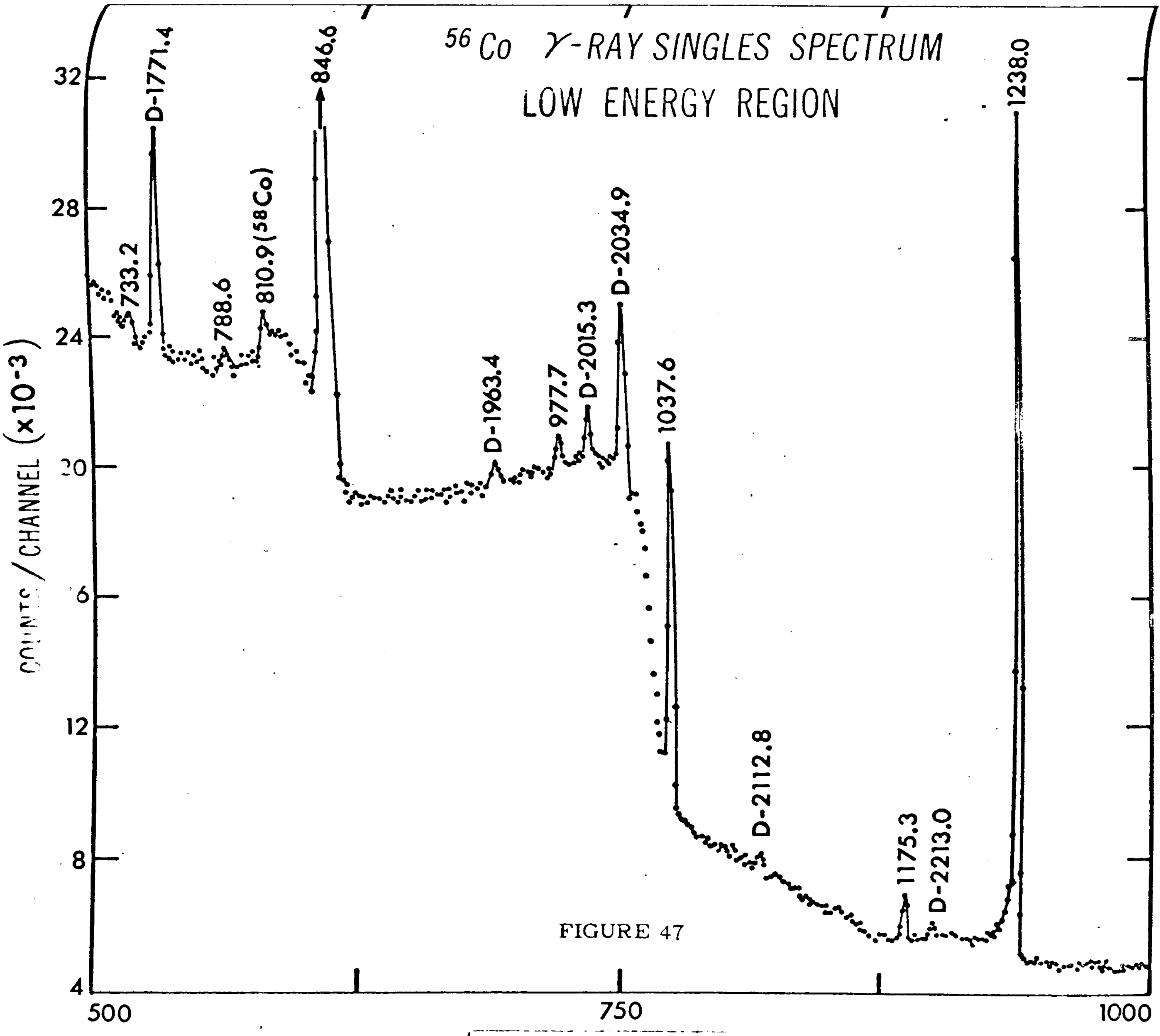

FIGURE 47

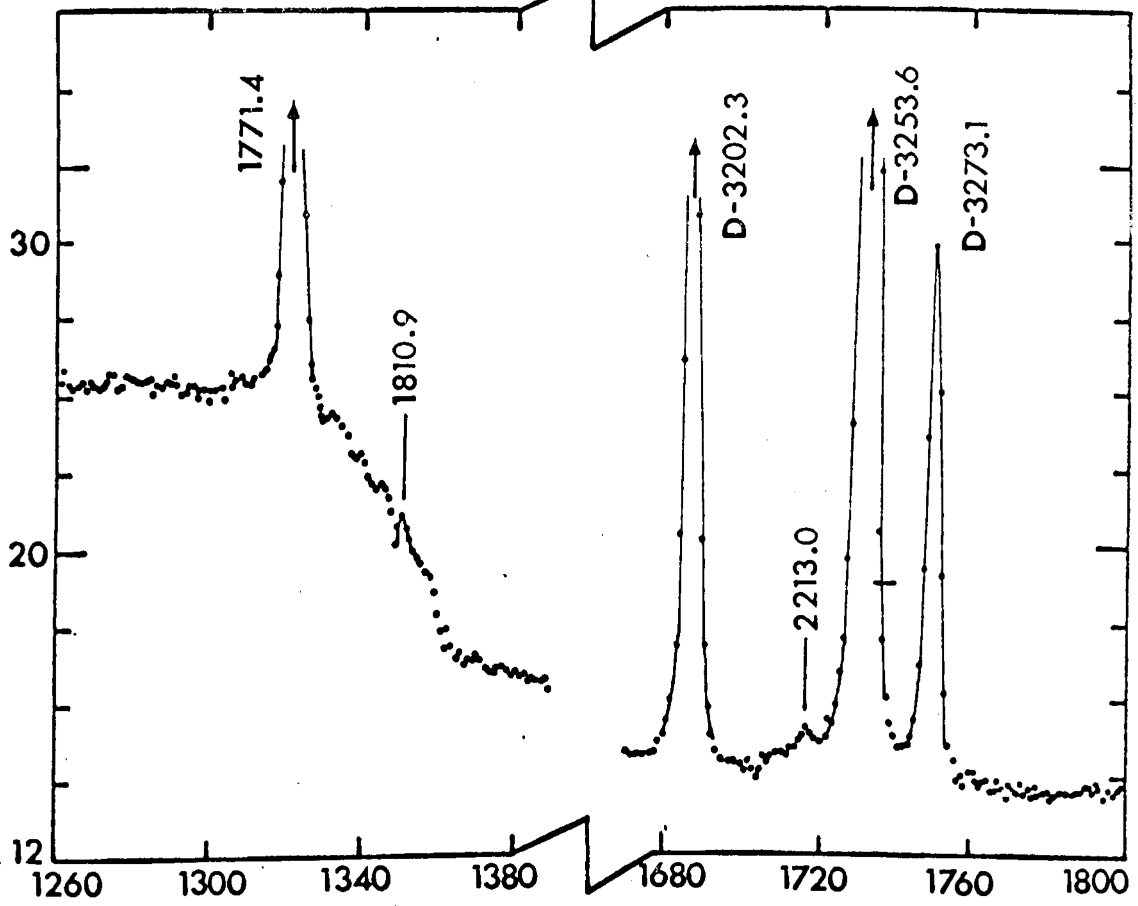

(a)

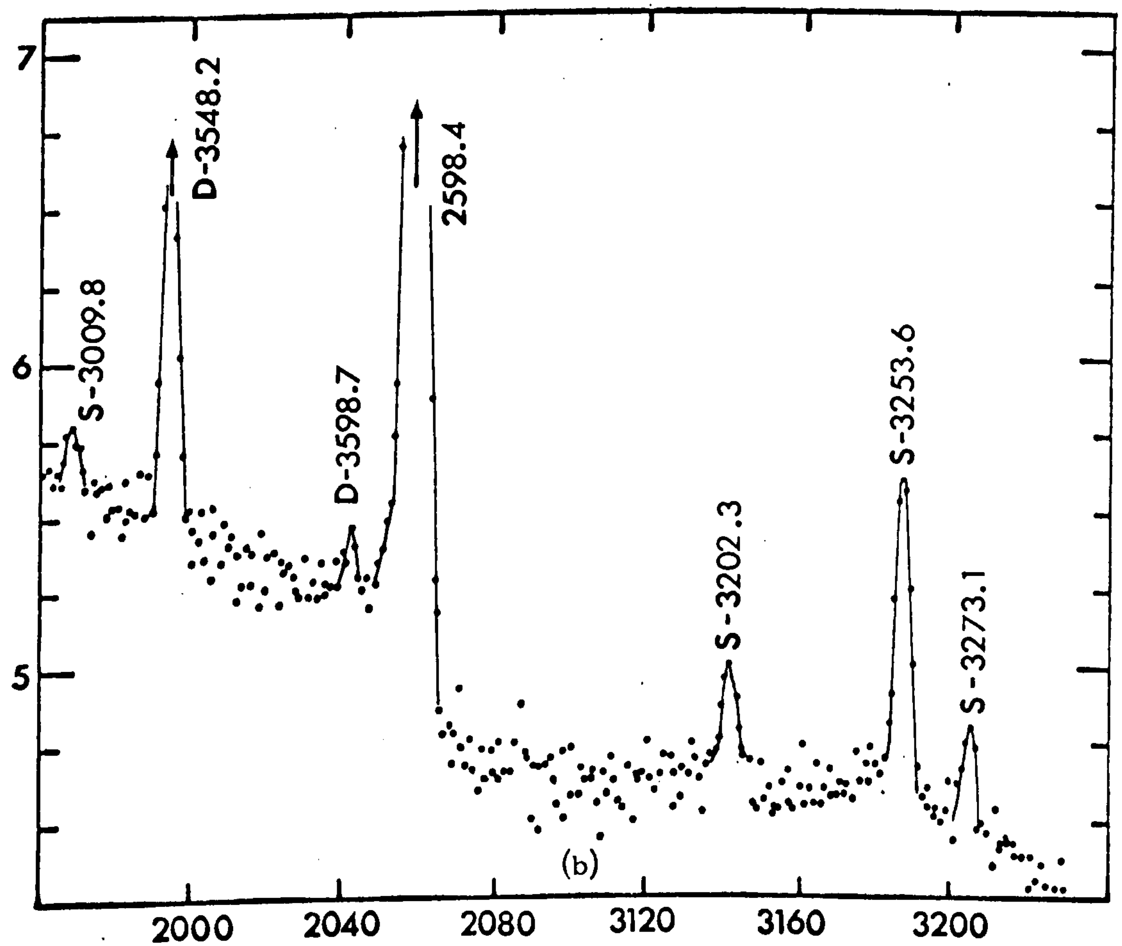

(b)

TABLE IV: Gamma-ray energy and intensity measurements on Co^{56}

Present Work		Auble, et.al.[7]		Pettersson, et.al.[93]		Dolan, et.al.[37]	
E_γ (keV)	$I_{rel}^{b)}$	E_γ (keV)	$I_{rel}^{b)}$	E_γ (keV)	$I_{rel}^{b)}$	E_γ (keV)	$I_{rel}^{b)}$
732.2±0.5	0.13±0.06	732.2 ±2.0	0.1 ±0.05	733.80 ±0.19	≈0.3		
788.6±0.5	0.2 ±0.1 a)	788.2 ±2.0	0.4 ±0.2	787.91 ±0.15	1.04±0.21		
	0.4 ±0.2						
846.6±0.5	100	846.6 ±0.5	100	846.82 ±0.09	100	846.5±0.2	100
977.7±0.5	1.01±0.3	977.8 ±1.0	1.36±0.36	977.46 ±0.14	1.73±0.35		
1037.6±0.5	12.1 ±0.8	1038.9 ±1.0	12.8 ±0.9	1038.02 ±0.11	14.1 ±1.5	1038.1±0.2	12.4±0.5
1175.3±0.5	2.2 ±0.1	1175.2 ±1.0	2.4 ±0.2	1175.25 ±0.14	2.1 ±0.6		
1238.0±0.5	70.2 ±2.5	1238.2 ±0.5	69.5 ±3.5	1238.56 ±0.14	66.8 ±4.0	1238.6 ±0.2	71.2±2.6
1359.8±0.5	4.2 ±0.4	1359.2 ±1.0	4.5 ±0.3	1360.58 ±0.14	4.0 ±0.8	1359.9 ±0.3	3.8±0.3
1771.4±0.5	16.7 ±1.0	1771.2 ±1.0	16.1 ±0.8	1771.90 ±0.22	16.2 ±1.4	1770.8 ±0.4	15.6±1.3
1810.7±0.5	0.5 ±0.3	1811 ±2	0.4 ±0.2				
1963.4±0.5	0.63±0.2	1965.4 ±1.0	0.59 ±0.09	1964.8 ±0.6	0.75±0.27		
2015.3±0.5	2.9 ±0.4	2015.3 ±1.0	2.7 ±0.2	2015.60 ±0.35	4.1 ±1.2	2015.6 ±0.7	3.8±0.7
2034.9±0.5	7.7 ±0.5	2035.2 ±0.5	7.4 ±0.6	2035.50 ±0.29	9.2 ±1.7	2034.7 ±0.3	7.8±1.0
2112.8±0.5	0.32±0.15	2113.2 ±2.0	0.29 ±0.05				
2213.0±0.5	0.2 ±0.02						
2598.4±0.5	17.0 ±0.6	2598.5 ±0.5	17.3 ±0.9	2599.7 ±0.5	17.4 ±1.5	2598.9±0.3	16.0±2.7
3009.8±0.5	1.0 ±0.1	3009.9 ±1.0	0.9 ±0.2	3010.4 ±0.8	1.3 ±0.4	3009.5±0.4	1.9±0.8
3202.3±0.5	2.8 ±0.4	3202.6 ±1.0	3.4 ±0.2	3202.3 ±0.5	3.2 ±0.5	3202.3±0.5	2.9±1.1
3253.6±0.5	7.3 ±0.5	3254.5 ±1.0	7.8 ±0.4	3254.0 ±0.5	8.5 ±0.6	3254.0±0.5	5.8±2.2
3273.1±0.5	1.5 ±0.4	3274.1 ±1.0	1.5 ±0.3	3272.8 ±0.6	1.5 ±0.4	3273.6±0.4	1.2±0.5
3451.3±0.5	0.83±0.1	3451.1 ±1.0	0.87 ±0.09	3452.5± 1.0	0.95±0.15	3452.6±0.5	0.7±0.3
3548.2±0.5	0.15±0.05	3547.6 ±2.0	0.15 ±0.03			3548.3±0.6	0.2±0.1
3598.7±0.5	0.02±0.01						

a) Corrected for contribution of 1811-D.E.

b) Intensity relative to that of 847-keV γ-ray.

Figure 49(a) and 49(b) show the gamma-ray single detector spectrum from Mn^{56} obtained in the present work. The full-energy peak due to the 3119.3-keV transition is resolved here for the first time from the adjacent Compton "knee" of the 3370.6-keV transition. Data from this study on the energy and relative intensity of the gamma-rays from Mn^{56} are presented in Table V. For comparison, previous results from the study of the decay of this nucleus by Ge(Li) detectors[7] and a bent-crystal spectrometer[95] are also presented.

TABLE V: Gamma-ray energy and intensity measurements on Mn^{56}

Present Work		Auble, et.al.[7]		Reidy and Wiedenbeck[95]
E_γ (keV)	I_{rel}	E_γ (keV)	I_{rel}	E_γ (keV)
846.7±0.5	100	846.8±0.5	100	846.79±0.09
1811.0±0.5	29.4 ±1.6	1810.9±0.5	30.0 ±3.0	1810.98±0.63
2113.0±0.5	16.0 ±0.9	2112.7±0.5	17.4 ±1.7	2110.0 ±1.6
2523.2±0.5	1.6 ±0.5	2523.6±1.0	1.1 ±0.15	
2658.0±0.5	0.66±0.06	2657.7±1.0	0.60±0.10	
2960.4±0.5	0.26±0.03	2960.8±1.0	0.31±0.06	
3119.3±0.5	0.08±0.04			
3370.6±0.5	0.20±0.04	3369.5±2.0	0.22±0.05	

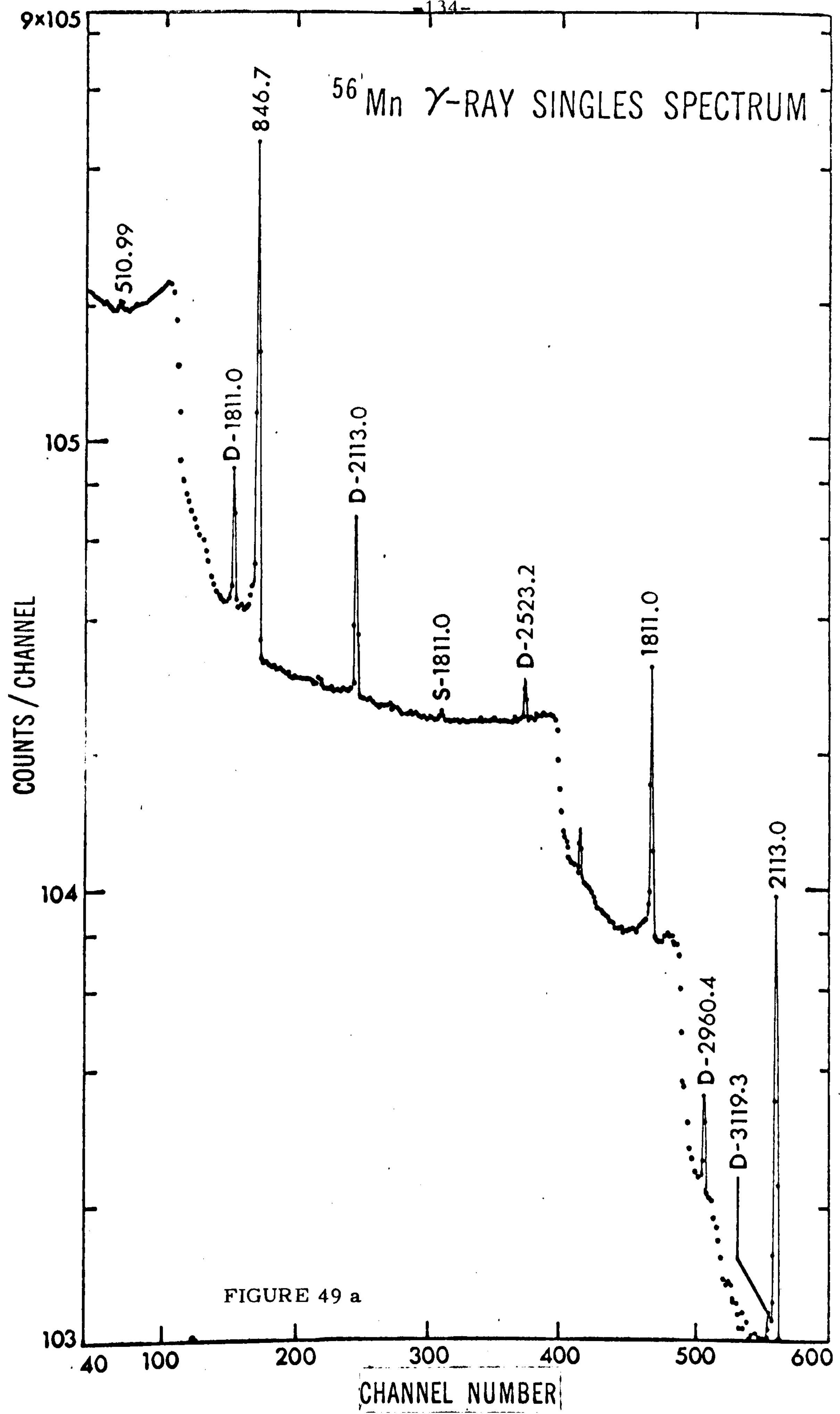

FIGURE 49 a

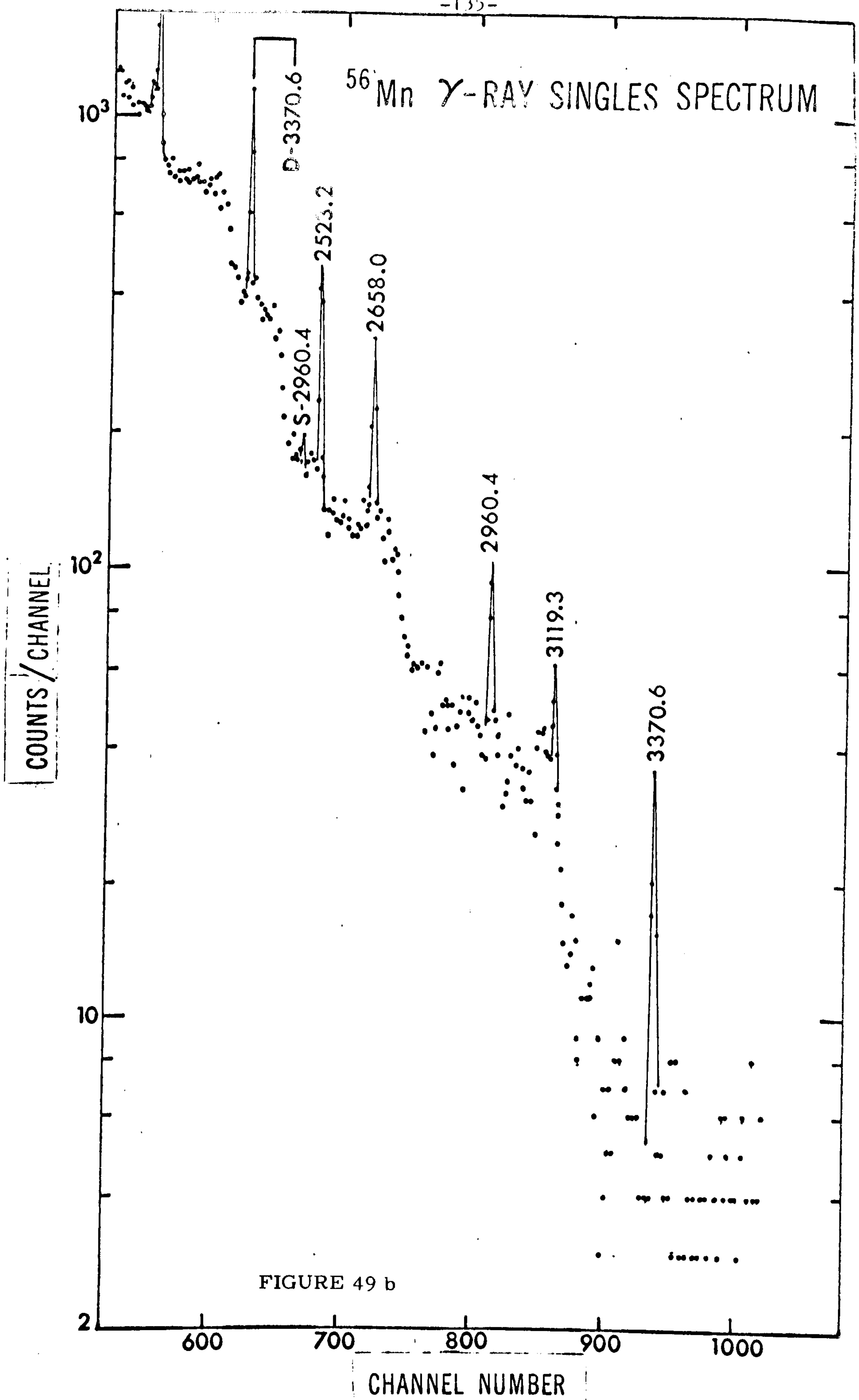

FIGURE 49 b

7.1.3 Gamma-Gamma Coincidence Studies A series of coincidence measurements were performed on the gamma-rays from Co^{56} in order to confirm the position of certain transitions in the decay scheme. The Nuclear Data ND-160 analyzer was employed in the two-parameter mode (see earlier) to record 256-channel spectra from the Ge(Li) detector in coincidence with 16-channel spectra from the NaI(Tl) detector. The settings were such that two successive 256-channel measurements (for a total of 512 channels) covered in the Ge(Li) detector an energy region from approximately 500 to 2700 keV so the highest energy transitions were observed through the corresponding double-escape peaks. The channels of the NaI(Tl) spectrum were set to embrace the full-energy peaks from the 847-, 1038-, and 1238-keV gamma-rays together with a small portion of the high energy region adjacent to the latter peak, the energy region covered by the indicated number of channels in each case determined by digital address selection.

Following the above measurements, a second identical set of experiments was performed to record spectra corresponding to random coincidence events (see earlier). When corrected for counting-time difference and source decay (equation 6-4), subtraction of the second set of spectra from the first allowed correction for random coincidence events.

Extraction of the desired gamma-gamma coincidence intensities was then achieved by comparison of the sixteen 512-channel spectra from the Ge(Li) detector, one with another. Of the 16 channels in the NaI(Tl) spectrum, some embraced both full-energy events from the gamma-rays of interest and also Compton escape events from higher energy radiations. At the same time, adjacent but higher energy channels could be selected

which gave a measure of the Compton escape contribution itself. Subtraction of Ge(Li) spectra in coincidence with the latter from those in coincidence with the former, with appropriate corrections for changes in intensity of the Compton escape continum from channel to channel, allowed Ge(Li) spectra to be obtained in coincidence with transitions in Co^{56} at energies of 847, 1038, and 1238 keV.

Figures 50 through 54 show the results thus obtained for the gamma-gamma coincidence measurements corrected for both Compton escape and random coincidence contributions. The results are further analyzed in Table VI in which the intensity of coincidences observed is classified as strong, medium, or weak.

7.1.4 Discussion The present work has produced evidence which confirms the existence of certain levels in Fe^{56} and sheds light on certain level spin assignments. In addition one level observed in the decay of Co^{56} and one in the decay of Mn^{56} are presented in the decay scheme of Figure 55 for the first time. The evidence and its interpretation which leads to new level data or confirmation of previous assignments is summarized below.

The Ground State (0+), 846.6-keV (2+), 2084.6-keV (4+), and 2657.5-keV (2+) Levels These levels were well characterized by previous studies; the present data are consistent with the previous energy, spin, and parity assignments.

The 2939-keV Level The previously reported[72] assignment of 0+ to this level on the basis of nuclear reaction studies is consistent with the present

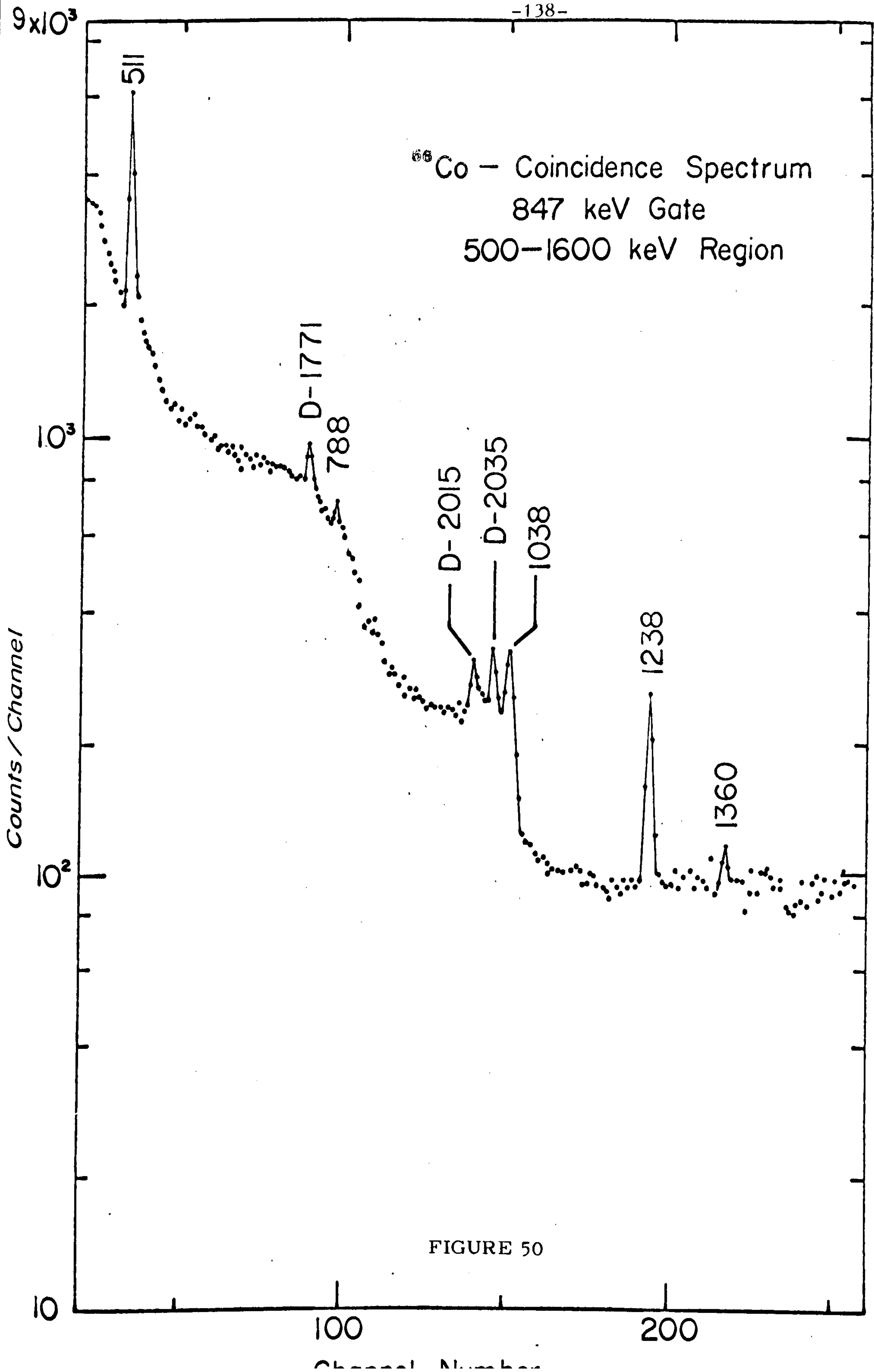

FIGURE 50

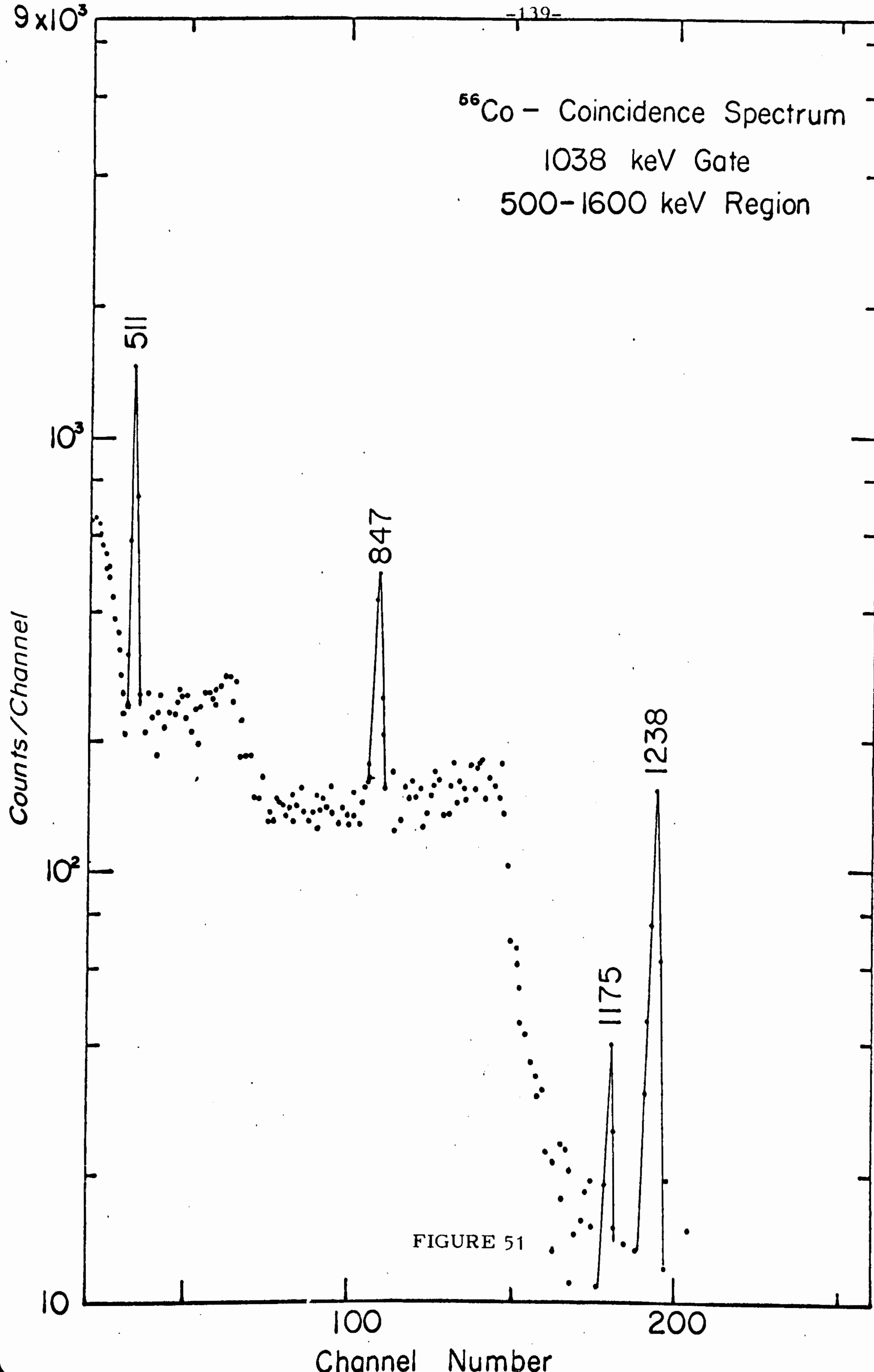

FIGURE 51

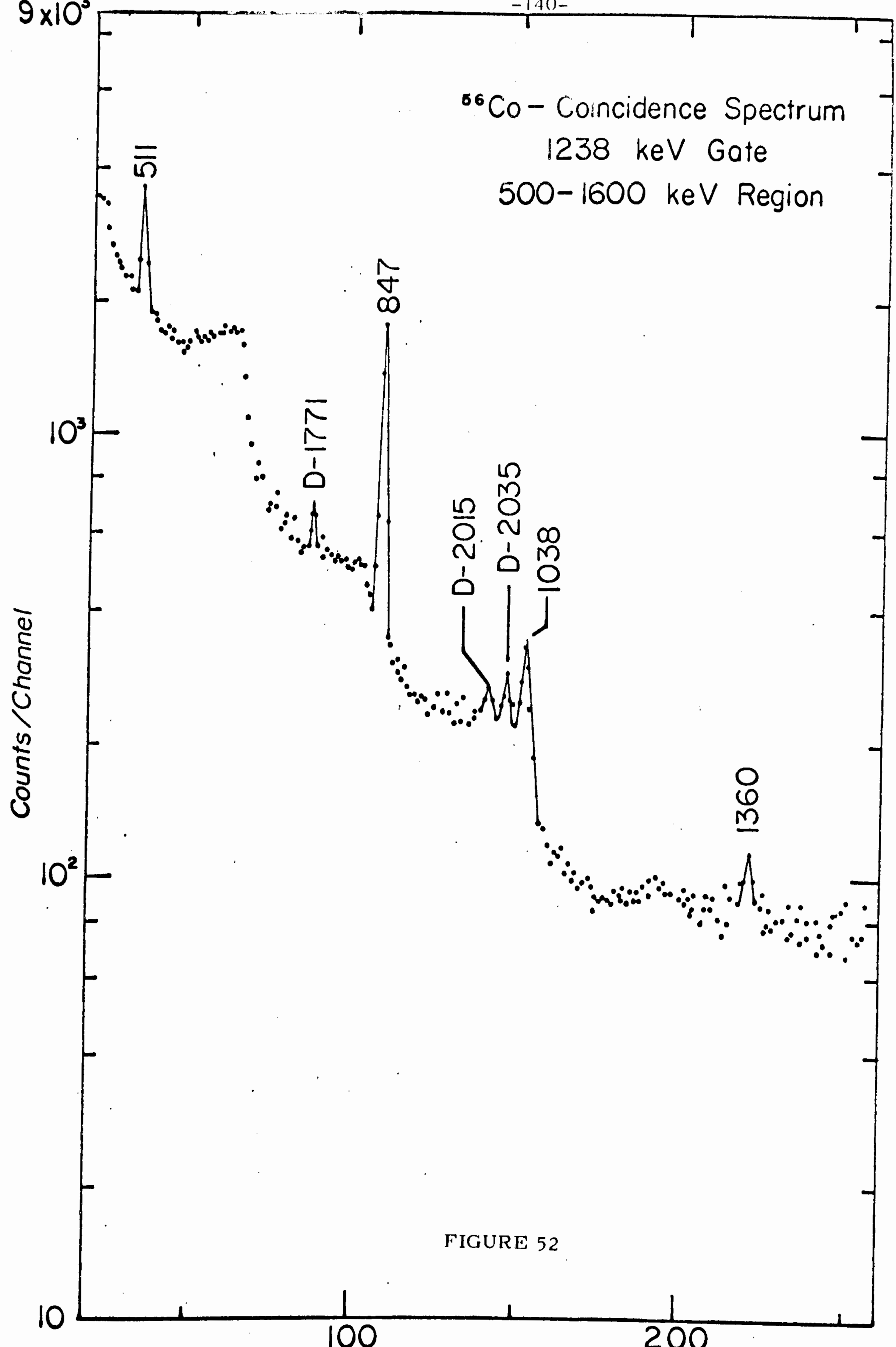

FIGURE 52

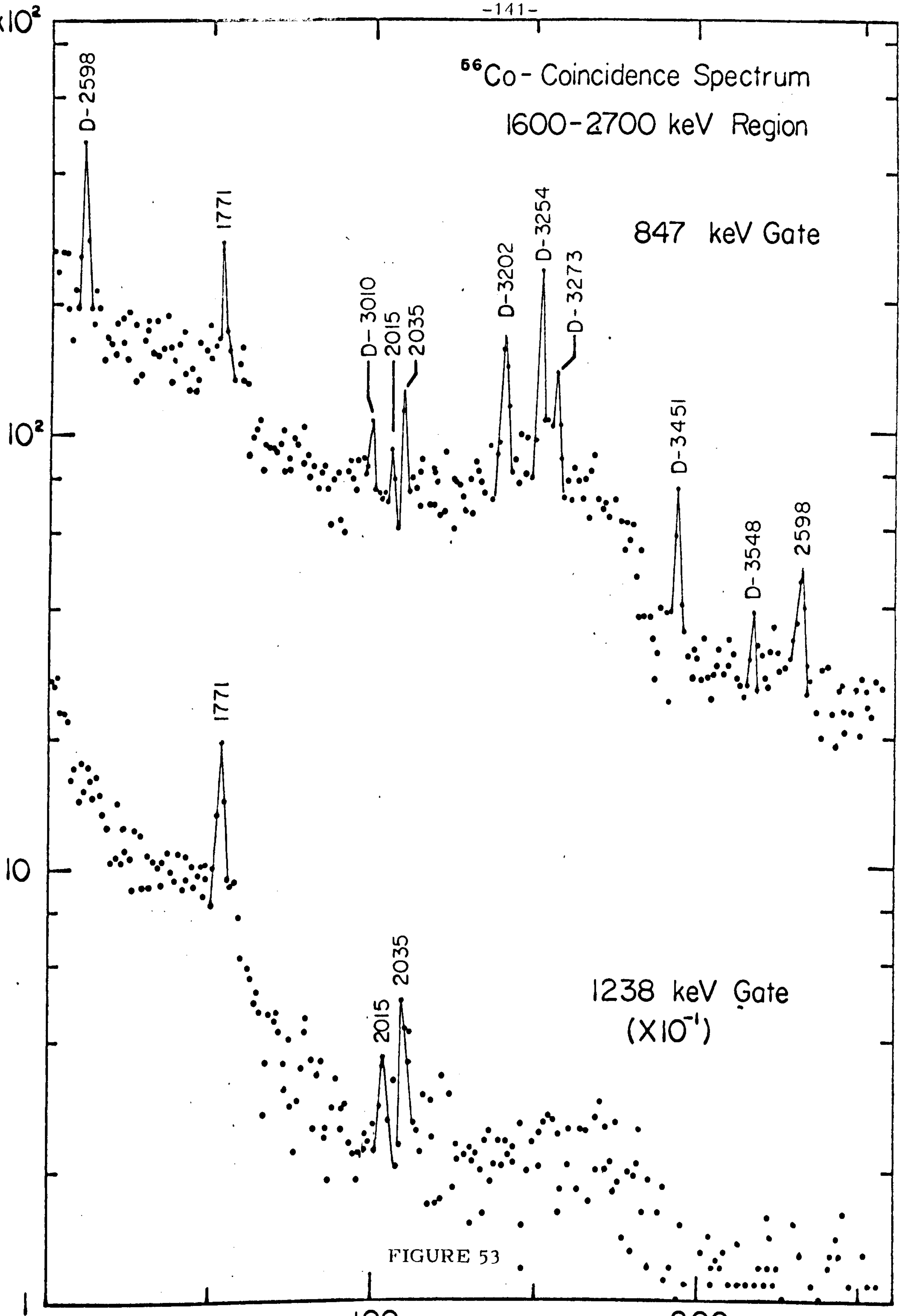

FIGURE 53

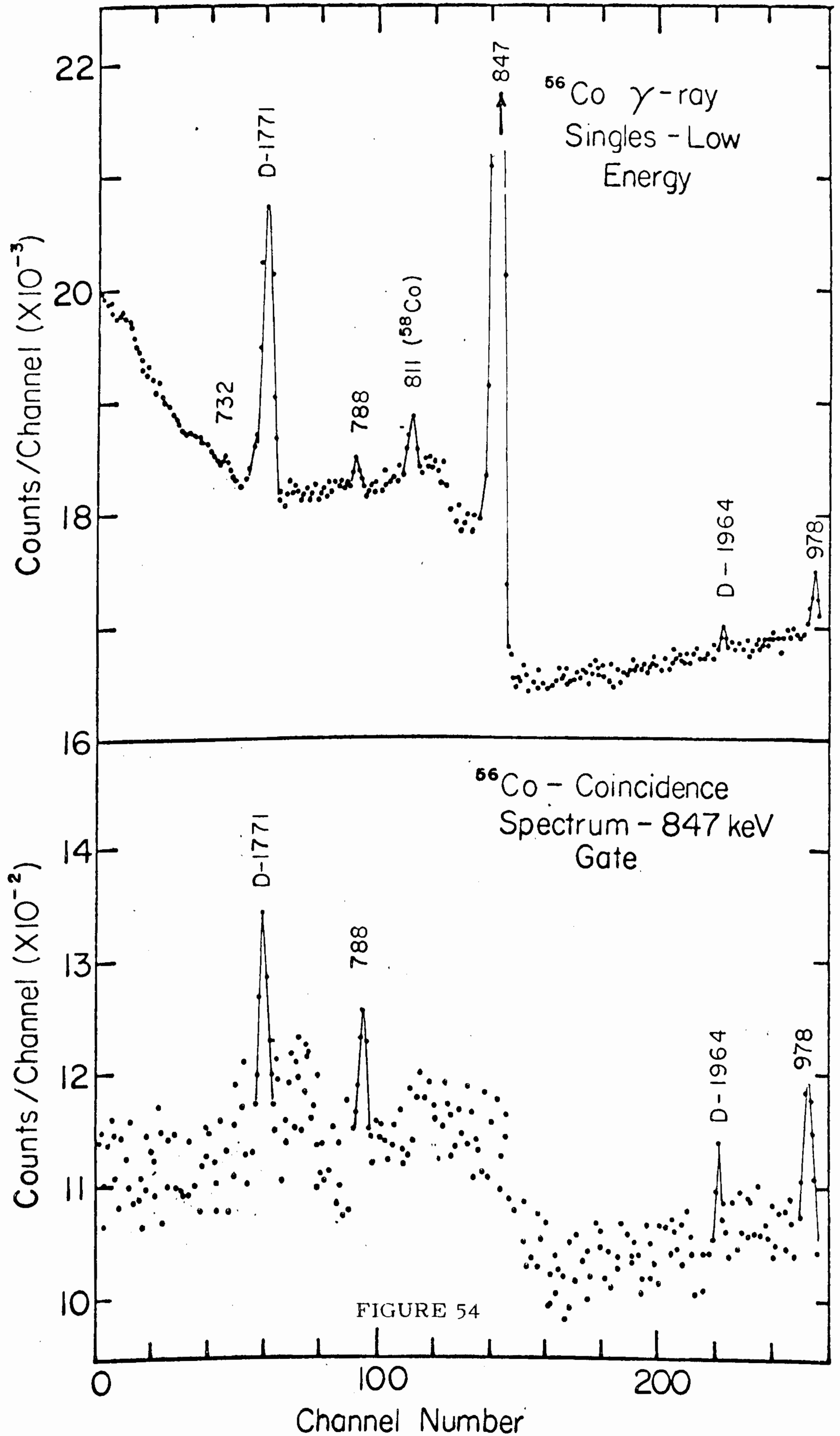

FIGURE 54

TABLE VI: Gamma-gamma coincidences in Co^{56}

Gamma-ray	in coincidence with:		
	846.6	1037.6	1238.0
Annihilation radiation	s	s	s
733.3	a)	a)	a)
788.6	w	NO	NO
846.6	NO	s	s
977.7	w	a)	a)
1037.6	s	NO	s
1175.3	a)	m	a)
1238.3	s	s	NO
1359.8	m	NO	s
1771.4	s	NO	s
1810.7	a)	-	-
1963.4	w	a)	a)
2015.3	m	NO	m
2034.9	m	NO	m
2112.8	a)	-	-
2213.0	a)	-	-
2598.4	s	NO	NO
3009.8	w	NO	NO
3202.3	m	NO	NO
3253.6	m	NO	NO
3273.1	w	NO	NO
3451.3	w	NO	NO
3548.2	w	a)	NO
3598.7	a)	a)	a)

s = stromg
m = medium
w = weak
a) = cannot be inferred from present measurements

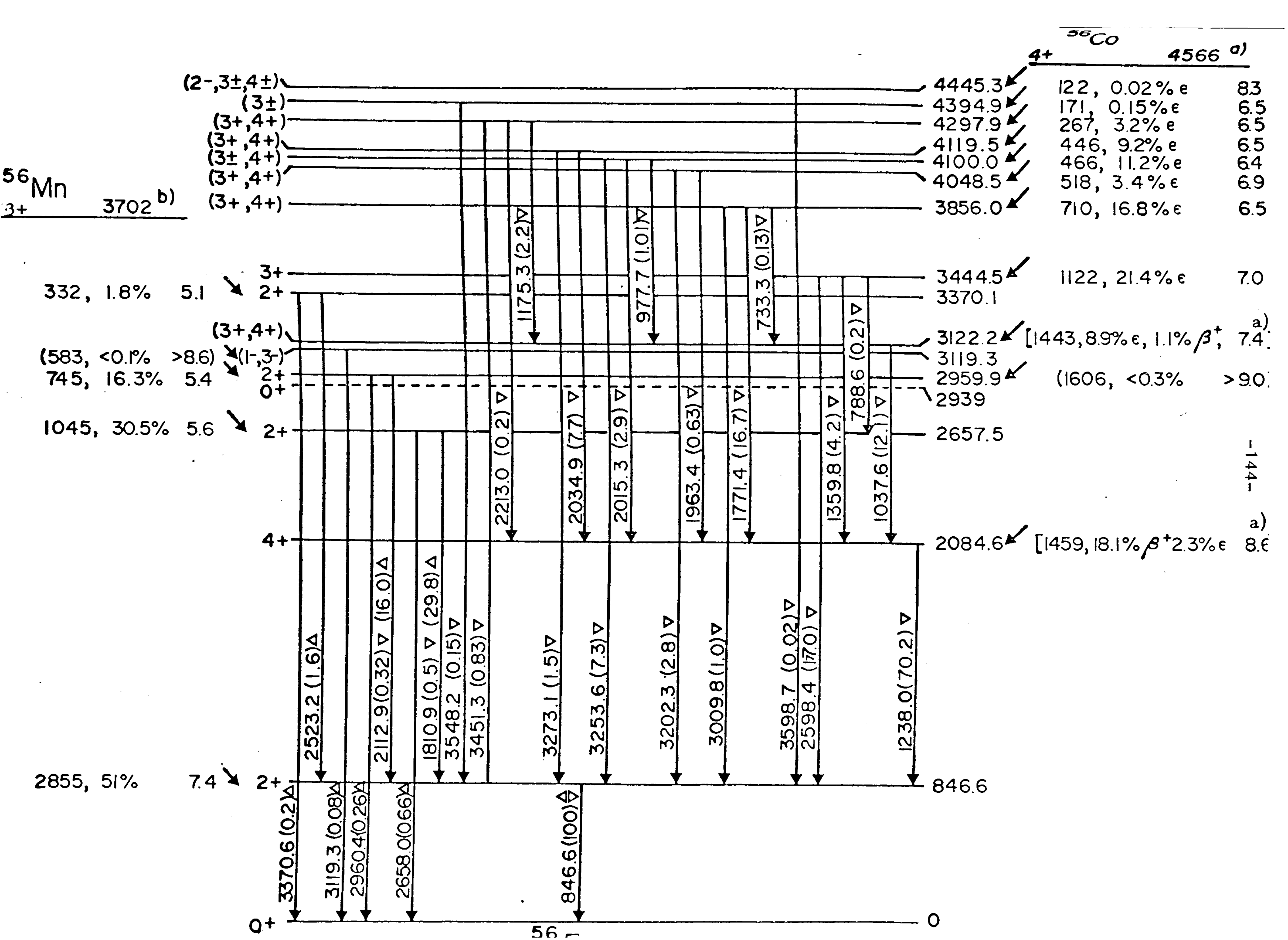

^{56}Co
4+ 4566 a)
^{56}Mn
3+ 3702 b)
(2-,3±,4±) 4445.3 122, 0.02% ε 8.3
(3±) 4394.9 171, 0.15% ε 6.5
(3+,4+) 4297.9 267, 3.2% ε 6.5
(3+,4+) 4119.5 446, 9.2% ε 6.5
(3±,4+) 4100.0 466, 11.2% ε 6.4
(3+,4+) 4048.5 518, 3.4% ε 6.9
(3+,4+) 3856.0 710, 16.8% ε 6.5
3+ 3444.5 1122, 21.4% ε 7.0
332, 1.8% 5.1 2+ 3370.1
(3+,4+) 3122.2 [1443, 8.9% ε, 1.1% β+, 7.4 a)
(583, <0.1% >8.6) (1-,3-) 3119.3
745, 16.3% 5.4 2+ 2959.9 (1606, <0.3% >9.0
0+ 2939
1045, 30.5% 5.6 2+ 2657.5
4+ 2084.6 [1459, 18.1% β+ 2.3% ε 8.6 a)
2855, 51% 7.4 2+ 846.6
0+ 0
3370.6 (0.2)
2523.2 (1.6)
3119.3 (0.08)
2960.4 (0.26)
2112.9 (0.32) (16.0)
2658.0 (0.66)
1810.9 (0.5) (29.8)
3548.2 (0.15)
3451.3 (0.83)
2213.0 (0.2)
1175.3 (2.2)
3273.1 (1.5)
846.6 (100)
2034.9 (7.7)
3253.6 (7.3)
2015.3 (2.9)
977.7 (1.01)
3202.3 (2.8)
1963.4 (0.63)
3009.8 (1.0)
1771.4 (16.7)
733.3 (0.13)
3598.7 (0.02)
2598.4 (17.0)
1359.8 (4.2)
788.6 (0.2)
1037.6 (12.1)
1238.0 (70.2)
56 Fe

failure to observe any evidence of population of it in either Mn^{56} or Co^{56} decay.

<u>The 2959.9-keV (2+) Level</u> The energy assignment of this level is confirmed by the present observation of a 2213-keV gamma-ray in both the decay of Co^{56} and the decay of Mn^{56} together with that of a 2960.4-keV gamma-ray in the latter decay (a ground state transition). This level is fed by a beta-transition with a log ft of 5.4 (evidently allowed) from Mn^{56} decay and with a beta-transition from Co^{56} with a log ft greater than 9. The previously proposed [72] assignment of 2+ is consistent with these observations. The spin assignment together with those for lower lying levels is also consistent with the present failure to observe de-excitation of the 2959.9-keV level by 875-keV and 302-keV transitions to the second and third excited states, respectively.

<u>The 3119.3-keV Level (tentatively 1-)</u> A level or multiplet at this energy has been previously proposed on the basis of nuclear reaction and radioactivity studies,[72,102] the present work is the first to report observation of a 3119.3-keV gamma-ray from radioactivity measurements. The present level scheme shows this transition as de-exciting to the ground state; there is no reason to prefer alternatives such as the placing of this transition as feeding the first excited state as the resulting level (3966 keV) has not been observed in previous work. The failure to observe population of this level from the beta decay of Co^{56} and a log ft value for the corresponding transition in Mn^{56} decay of greater than 8.6 together lead to level spin assignments of 1-, 2-, or 3- as being most probable. A value of 3- and octupole character has been assigned to a level at about this

energy by Ricci, et.al.[98] The intensity of this transition (0.08%) together with single-particle estimates of the transition probabilities for this transition, require that the E1 transition from a 3119.3 (3-) level to the 2+ first excited state be hindered by a factor of approximately 10^9 in order that it not be observed. The assignment of 1- to the 3119.3-keV level, however, is consistent with the transition to the first excited state not being observed and with the results of Shapiro, et.al.,[102] who observed decay from this level to the ground state and first excited state in $Fe^{56}(p,p'\gamma)$ reactions, indicating a probable spin of 1.

The 3122.2-keV Level (3+, 4+) Confirmation of the energy assignment of this level presently arises from the observation of a 1037.6-keV gamma-ray third in intensity in the scheme and intense gamma-gamma coincidences between the 1037.6- and 1238.0-keV transitions. This, together with the population of this level via a beta transition from Co^{56} with a log ft value of 7.4 and failure to observe such population in the decay of Mn^{56} are all consistent with previous[7] assignment of 3+ or 4+ to this level.

The 3370.1-keV Level (2+) The present study confirms the energy assignment on the basis of observation, following the decay of Mn^{56}, of gamma-rays of energy 3370- and 2523-keV; the energy difference establishes these as the ground state and first excited state transitions, respectively. The log ft for the beta transition to this level from the ground state of Mn^{56} is found to be 5.1 corresponding to an allowed transition. No feeding of this level is observed in the decay of Co^{56}; this confirms a spin for the level of 2+. This value is also consistent with the observation that the level is observed to decay to the ground and first excited states with all other possible transitions being unobserved.

The 3444.5-keV Level (3+) The energy assignment is confirmed by the present observation following the decay of Co^{56} of gamma-rays of energy 2598.4, 1359.8, and 788.6 keV. From the energy differences, it is clear that these feed, respectively, the first, second, and third excited states of Fe^{56}. Gamma-gamma coincidences observed between the 2598- and 847-keV gamma-rays, 1359- and 1238-keV gamma-rays, 788.6- and 847-keV gamma-rays confirm this deduction. The previously proposed[7,93] spin of 3+ for this level is consistent with the log ft of 7.0 observed for the beta transition from Co^{56} which feeds it, together with the observation of the three de-populating gamma-rays listed above.

The 3388-keV Level (6+) The present failure to observe population of this level[108] is consistent with previous studies of Mn^{56} and Co^{56}.[72]

The 3450- 3600-keV Levels Levels at these energies were previously reported[8,13,102] on the basis of nuclear reaction studies. In the present study, gamma-rays of energy 3451.3 keV and 3598.7 keV were observed, the former being in coincidence with the 847-keV gamma-ray. It is believed that neither is a ground state transition, and both are now assigned as de-exciting higher-lying levels to the first excited state.

The 3856.0-keV Level (3+ or 4+) The energy assignment is confirmed by the observation of a gamma-ray of energy 3009.9 keV (in coincidence with the 847-keV gamma-ray), a gamma-ray of energy 1771.4 keV (in coincidence with the 1238-keV gamma-ray), and a gamma-ray of energy 733.3 keV. Energy differences and the coincidence relationships serve to confirm that the first two of these gamma-rays feed the first and second excited states, respectively. The third evidently feeds the level at 3122.2 keV.[7]

The parent level is fed from the Co^{56} decay with a log ft of 6.5, indicating level spins of 3+, 4+, or 5+. Observation of intense feeding of the 2+ first excited state from this level suggests elimination of the 5+ possibility. Previous studies[36,93] favor a spin 3 value.

The 4048.5-keV Level (3+ or 4+) The energy assignment confirmation is based on the present observation of gamma-rays of energy 3202.3 and 1963.4 keV, both in coincidence with the 847-keV transition. This level is fed from the decay of Co^{56} by a beta transition of log ft = 6.9, suggesting spins of 3, 4, or 5+ for this level. Observation of preferential gamma-decay to the 2+ first excited state eliminates the spin 5 possibility. Observation of the two gamma-rays listed above and failure to observe other possible transitions are consistent with 3$\pm$ and 4+ spin assignments; the possibility of negative parity was discarded by Auble, et.al.[7]

The 4100.0-keV Level (3+ or 4+) The energy assignment is confirmed by the present observation of gamma-rays of energy 3253.6 keV (in coincidence with 847- and 1238-keV gamma-rays), and 977.7 keV (in coincidence with the 847-keV gamma-ray). This level is fed from the decay of Co^{56} by a beta transition of log ft = 6.4. Arguments similar to those above lead to confirmation of 3+ and 4+ as possible spin and parity assignments.

The 4119.5-keV Level (3+ or 4+) The energy assignment is confirmed by the present observation of gamma-rays of energy 3273.1 keV (in coincidence with the 847-keV gamma-ray) and 2034.9 keV (in coincidence with the 1238-keV gamma-ray). This level is fed by the decay of Co^{56} through a beta transition of log ft value 6.5; as before, a spin and parity assignment of 3+ or 4+ is confirmed.

The 4297.9-keV Level (3+ or 4+) The present confirmation of the energy of this level is by observation of gamma-rays of energy 3451.3 keV (in coincidence with the 847-keV gamma-ray), 2212.8 keV, and 1175.3 keV (in coincidence with the 1238-keV transition). This level is fed in the decay of Co^{56} by a beta transition of log ft 6.5; as before, a 3+ or 4+ spin and parity assignment is confirmed.

The 4394.8-keV Level ($3^{\pm}$) The proposal[7,37] of a level at about this energy is consistent with present observation of a gamma-ray of energy 3548.2 keV in coincidence with the 847-keV transition. The proposed level would be fed in the decay of Co^{56} by a beta transition with a log ft value of 6.5. Observation only of the transition to the first excited state among the possible de-exciting gamma-transitions would perhaps indicate against spin assignments of 4.

The 4445.3-keV Level (2−, $3^{\pm}$, or $4^{\pm}$) The present observation of a low intensity gamma-ray of energy 3598.7 keV and a similar argument to that presented for the level described above lead to the present proposal that the level at 4445.3 keV exists as seen[58] in p,p' and p, α studies. The calculated log ft for the beta transition from Co^{56} feeding this level is 7.9, in turn consistent with spin and parity assignments of 2−, 3± or 4±. Of these possibilities, the 4± values are probably less likely in view of the observed gamma-ray de-excitation pattern.

Either this level at 4445.3 keV or that at 4394.8 keV could correspond to the second 3− octupole state observed by Ricci, et.al.,[98] at an excitation energy of 4.4 MeV via nuclear reaction studies.

7.1.5 Conclusion A recent shell model calculation has been performed by McGrory[80] for Fe^{56}, Cr^{54}, and Fe^{57} assuming a ${}_{20}Ca^{48}_{28}$ core with additional protons restricted to the $1f_{7/2}$ shell and the two neutrons outside the filled $1f_{7/2}$ shell in Fe^{56} being allowed to occupy $2p_{3/2}$, $2p_{1/2}$, and $1f_{5/2}$ orbits. (As in atomic spectroscopy, quantum states may be characterized by a set of quantum numbers n, l, and j; the designation $1f_{7/2}$ refers to the state with principal quantum number $n = 1$, orbital angular momentum $l = 3$, and total angular momentum $j = 7/2$). The calculation fails to predict the 2+ level at 2957 keV which is presumably due to the excitation of protons from the $1f_{7/2}$ to the $2p_{3/2}$ orbit.[102]

The beta-decay of Co^{56} involves the transformation of a $1f_{7/2}$ proton and will therefore go mainly to configurations containing $1f_{5/2}$ neutrons (as the $1f_{7/2}$ shell is filled). The model[80] does predict admixtures of such configurations for the 4+ 2085-keV and (3+ or 4+) 3122-keV levels; however, the main concentration of the $1f_{5/2}$ neutron states would be expected to lie at higher energy.[102] The 3+ and 4+ levels in Fe^{56} could also be complex mixtures of shell model configurations including:

$(1f_{7/2}^{-2}, J_p{=}0;\ 2p_{3/2}1f_{5/2}, J_n{=}3 \text{ or } 4)_{J=3 \text{ or } 4}$, $(1f_{7/2}^{-3}, 2p_{3/2}, J_p{=}3 \text{ or } 4;\ 2p_{3/2}^{2}, J_n{=}0)_{J=3 \text{ or } 4}$, $(1f_{5/2}^{-3}, 2p_{3/2}, J_p{=}3 \text{ or } 4;\ 2p_{3/2}^{2}, J_n{=}0)_{J=3 \text{ or } 4}$, $(1f_{7/2}^{-2}, J_p{=}4;\ 2p_{3/2}^{2}, J_n{=}0)_{J=4}$, and $(1f_{7/2}^{-2}, J_p{=}2;\ 2p_{3/2}^{2}, J_n{=}2)_{J=3 \text{ or } 4}$.

Since the ground state of Co^{56} (4+) is of the $(1f_{7/2};\ 2p_{3/2})$ configuration,[37] transitions to all but the first of the above configurations are forbidden, in principle, by the selection rules for orbital angular momentum transfer, i.e., they are "l-forbidden." (Except for the first configuration, a transformation of a $1f_{7/2}$ proton to a $p_{3/2}$ neutron is required). Thus the hindrance of allowed beta-decay from Co^{56} to the 4+ 2085-keV and (3+ or 4+) 3122-,

3445-, and 3856-keV levels (observed experimentally; see Figure 55 for log ft values) can be understood from the above simple shell model considerations.

The ground state to ground state decay of Mn^{56} would require[102] the transformation of a $p_{3/2}$ neutron into an $f_{7/2}$ proton which is l-forbidden; thus decay will go predominantly to the states with admixture of the $(1f_{7/2}^{-3}; 2p_{3/2})$ proton configuration. If the $(1f_{7/2}^{-3}; 2p_{3/2})_{J=2+}$ configuration is at the same energy in Fe^{56} as in the chromium nucleus[80] it would be expected to mix with the predicted 2+ states, which would explain the allowed beta-decay to the 3370-, 2960-, and 2658-keV 2+ levels in Fe^{56}.

7.2 The Decay of Ge^{66} The excited states in Ga^{66} populated in the positron-decay of Ge^{66} are the subject of only one study published thus far in the literature; this work by Ricci, et.al.,[97] using scintillation detectors for beta- and gamma-spectroscopy for both single detector and beta-gamma and gamma-gamma coincidence studies shows levels populated in Ga^{66} with a maximum energy of 760 keV, whereas the ground state decay energy of Ge^{66} is 3 MeV.[64] As the Ge^{66} activity was available from another experiment[100] being undertaken at this laboratory, it was decided to investigate the gamma-rays following the decay of Ge^{66} with Ge(Li) detectors with one objective being to search for transitions de-exciting levels of higher energy than previously observed.[97]

7.2.1 Source Preparation The Ge^{66} sources were produced by bombarding chemically pure, metallic zinc foil with 26-MeV alpha particles from the University of Washington cyclotron. Following a suitable chemical separation,[100] which included dissolution of the irradiated target foils in 6N HCl containing Ge and Ga carriers, and distillation of the Ge fraction as the tetrachloride into 6N HCl, the samples were assayed with Ge(Li) detectors, either as liquid sources or precipitated as the sulfide onto filter paper discs. A series of spectra were obtained spaced in time so that impurity activities could be identified from their rate of decay and not assigned to the 2.4-hour Ge^{66} activity.

Impurity activities and gamma-rays assigned to these activities include 9.5-hour Ga^{66} (1040 keV), 78-hour Ga^{67} (93, 184, and 300 keV), and 40-hour Ge^{69} (574, 872, and 1107 keV). Because of the inherent high resolution of Ge(Li) detectors, the presence of these impurity gamma-rays did not affect the interpretation of the spectra as they had in part of the previous work.[97]

7.2.2 Single Detector Measurements Figures 56 and 57 show a gamma-ray single detector spectrum obtained from the decay of Ge^{66} using the 0.85 cm^3 Ge(Li) detector and electronic equipment described earlier. A gamma-ray of energy 536.9 keV is reported for the first time; the previously reported[97] gamma-ray of energy 185 keV is shown to be resolved into two gamma-rays of energy 181.9 and 189.8 keV. The previously reported[97] transition of energy 152 keV was not observed in the present work, and an upper limit of 0.5% is placed on its intensity; also the 381.4-keV gamma-ray was not found to be an unresolved (with NaI(Tl) detectors) doublet as required by Ricci, et.al.,[97] for their decay scheme. If the second gamma-ray were to exist, its energy would be 369.0 keV according to the present decay scheme, and could have easily been detected in the present work as its intensity was required to be approximately 33%.[97] The presence of a gamma-ray of energy 706.3 keV is confirmed. A search was made for higher energy gamma-rays resulting from the decay of Ge^{66}, but none were found which could not be assigned to the longer-lived impurity activities described above. The peak at 318 keV was also present in a spectrum taken about 15 hours after that shown in Figure 56, but could not be ascribed to any impurity activity from the information presently available in the literature. An upper limit of 0.5% is assigned to the intensities of higher energy gamma-rays in the Ge^{66} decay.

Table VII summarizes the data, presenting gamma-ray energies and intensities obtained in the present study along with the corresponding data of Ricci, et.al.,[97] for comparison.

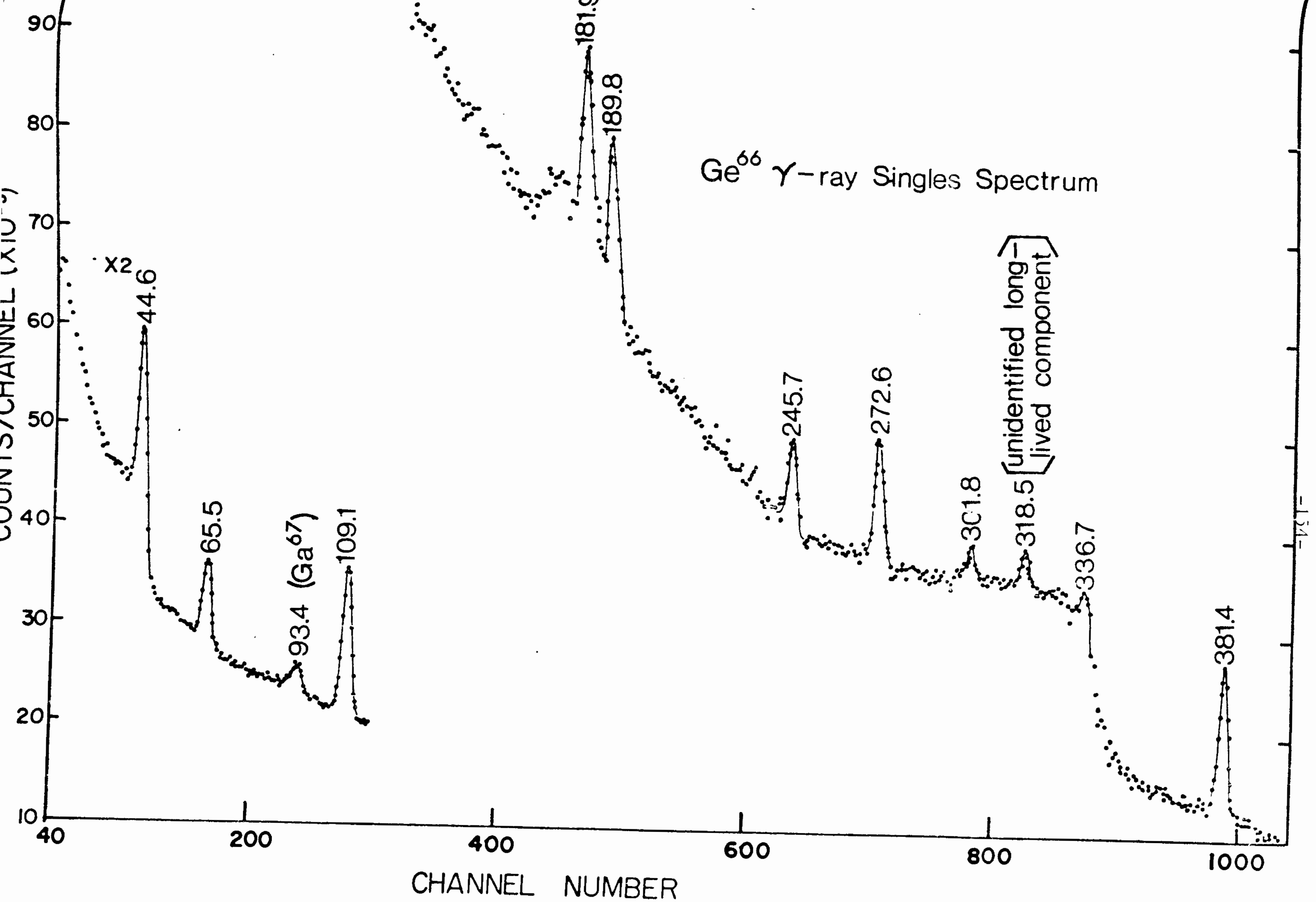

FIGURE 56

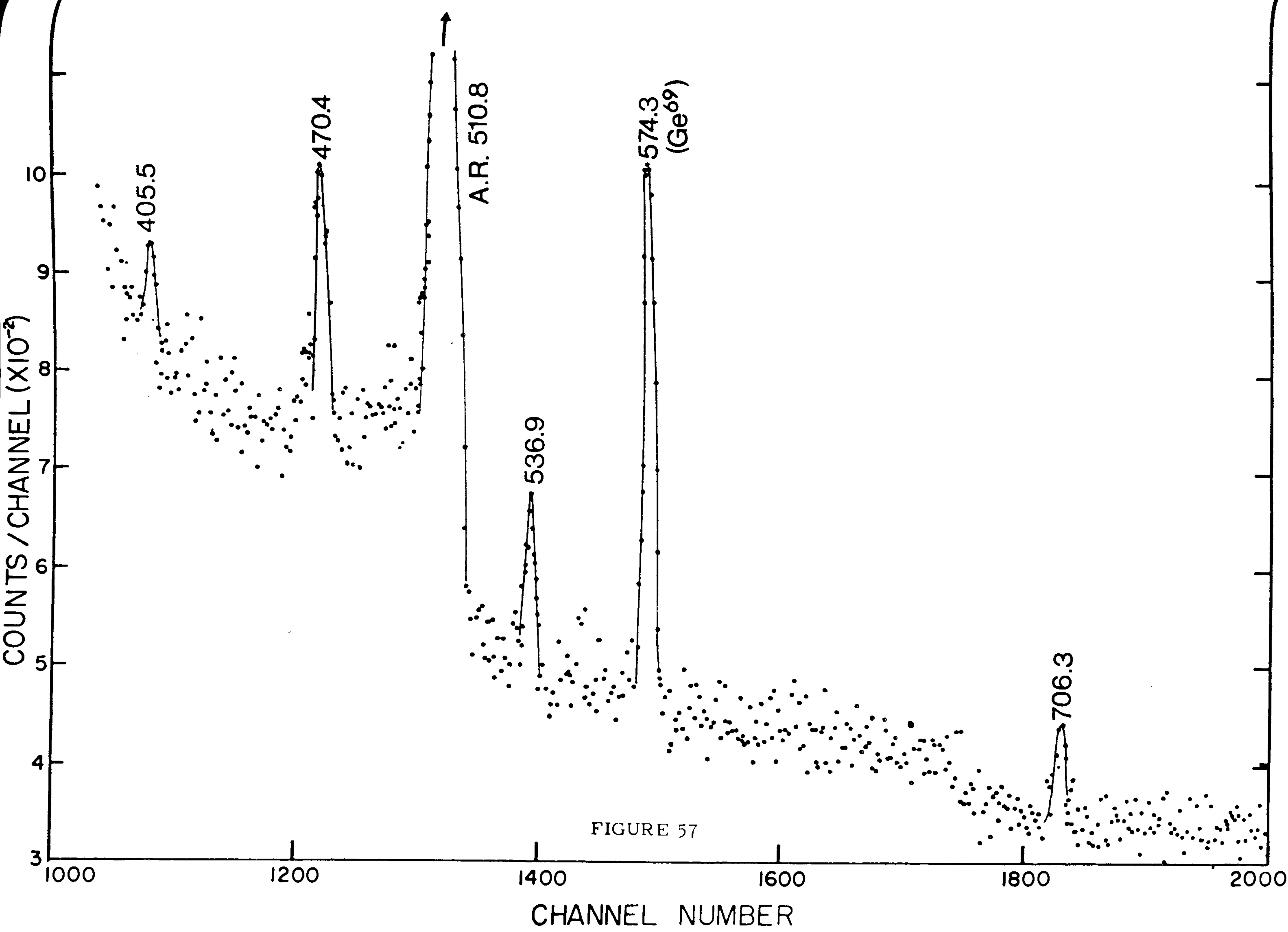

FIGURE 57

TABLE VII:

Gamma-ray energy and intensity measurements on Ge^{66}

Present Work			Ricci, et.al.[97]	
E_γ(keV)	I_{rel}	%/decay	I_{rel}	E_γ (keV)
44.6 ±0.5	94.6±9.5	31.4 ±5.5	78± 10	46 ±2
65.5 ±0.5	23.9±2.4	8.3 ±1.2	23± 2	68 ±2
109.1 ±0.5	40.8 ±4.1	13.6 ±1.8	46± 9	114 ±2
			≈2	152 ±4
181.9 ±0.5	13.6±1.4	4.6±0.7	47±10	185 ±4
189.8 ±0.5	20.3±2.0	6.8±1.0		
245.7 ±0.5	22.0±2.2	7.3±1.0	14±9	245 ±5
272.6 ±0.5	37.7±3.8	12.6±1.8	40±4	270±10
301.8 ±0.5	12.8±2.4	4.3±0.7	13±5	300±10
336.7 ±0.5	18.7±3.8	6.2±1.0	40±9	335±8
381.4 ±0.5	100	33.3±4.5	100	380±8
405.5 ±0.5	2.0±0.4	0.7±0.2	12±4	405±10
470.4 ±0.5	38.6±3.9	12.9±1.7	40±4	470±10
(515)	(40)	(13)		
536.9 ±0.5	24.7±2.5	8.2±1.2		
706.3 ±0.5	4.3±0.9	1.4±0.4	5± 1	710 ±10

The gamma-ray of energy 515 keV was not observed in the present work (see below); because the 511-keV full-energy peak due to annihilation quanta is broadened, in addition to detector contributions, by the Doppler shift of annihilation quanta energy due to the motion of the electron-positron system at the time of annihilation,[43] a postulated 515-keV gamma-ray would not be resolved from the 511-keV peak. The intensity ratio of the 511- and 515-keV peaks would also contribute to the failure to observe such a gamma-ray in the present work.

The agreement in gamma-ray energy and intensity between the two studies as shown in Table VII is within the quoted experiemental uncertainties

except for the relative intensity of the 405-keV transition. The inclusion of the 515-keV gamma-ray in the present work results in an additional uncertainty of approximately 5% in the intensity per decay values and is included in the above uncertainties.

The decay scheme derived from the present measurements is shown in Figure 58; the intensities of positron and K-capture decay to the various levels were calculated from the present gamma-ray intensities and K-capture to positron ratios given in the Table of Isotopes.[66] If the 515-keV transition were not included in the decay scheme, the log ft value for the decay to the 515.0-keV level would be increased by 0.2, and that of the 381.9-keV level decreased by 0.1; thus, the intensity of the 515-keV gamma-ray, whether included or excluded from the scheme, has little effect on the choice of spin and parity values for the levels.

The main features of the decay scheme of Ge^{66} as shown in Figure 58 are in agreement with that proposed by Ricci, et.al.,[97] with the following important differences: A new level is presently proposed at an energy of 536.9 keV. Because the 369-keV transition proposed by Ricci, et.al.,[97] was not observed (750.0-keV level to 381.9-keV level), the level at 381.9 keV is assumed to be populated by approximately 45% of the total ground state decay of Ge^{66} (as compared to $-2 \pm 6\%$ proposed previously[97]). Ricci, et.al.,[97] reported finding two positron groups of end-point energy 1.3 ± 0.1 and 2.0 ± 0.2 MeV whose relative intensities were approximately 100% and 10%, respectively.

7.2.3 Discussion of Results The decay scheme presented in Figure 58 was derived from the results of the present work based entirely upon the framework of the previously proposed[97] decay scheme and the energy sum

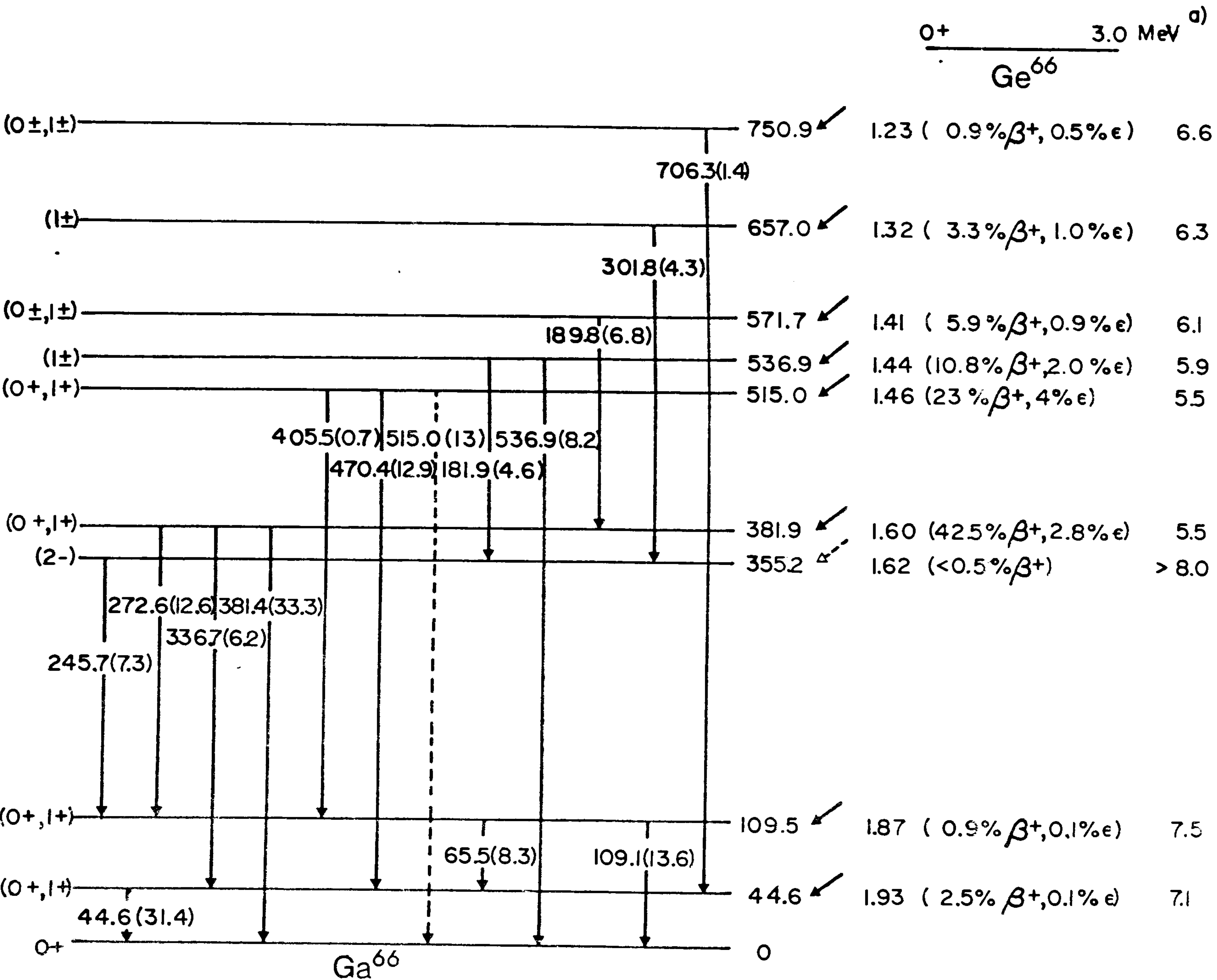

FIGURE 58

rule for the more accurate gamma-ray energy determinations obtained with the Ge(Li) detector. While the decay scheme presently obtained is consistent in energy and intensity balance, certain anomalies are apparent.

The Ground State (0+) The ground state of 9.5-hour Ga^{66} has been measured[43] to be 0+.

The 44.6-keV Level and 109.5-keV Level (0+ or 1+) The energies of these levels are proposed from the observation of the 44.6-keV, 65.5-keV, and 109.1-keV gamma-rays in the present work and cascade proposed by Ricci, et.al.[97] on the basis of observed gamma-gamma coincidences. The log ft values for beta-transitions to these levels, 7.1 and 7.5 respectively, point to spin and parity assignments of 0$\pm$ or 1$\pm$. The intensities and pattern of decay of the observed gamma-rays lead to the probable exclusion of the negative parity values in agreement with Ricci, et.al.[97]

The 355.2-keV Level (2-) The position of this level is established from the detection of the 245.7-keV gamma-ray and the level at this energy (360 keV) proposed by Ricci, et.al.[97] The log ft value of greater than 8 leads to possible spin and parity assignments of 0$\pm$, 1$\pm$, or 2-. The choice of 2- would seem to explain the absence of an observed transition to the 0$\pm$ ground state, however, one would still expect to observe a transition corresponding to the de-excitation of the 355.2-keV level to the 0+ or 1+ first excited state.

The 381.9-keV Level (0+ or 1+) Gamma-rays of energy 381.4, 336.7, and 272.6 keV were observed in the present work in agreement with similar results of Ricci, et.al.,[97] and their coincidence measurements. The log ft value for Ge^{66} decay to this level of 5.5 (evidently allowed) and the

observed gamma-transitions are consistent with 0+ or 1+ spin and parity.

The 515.0-keV Level (0+ or 1+) The energy assignment of this level is made on the basis of gamma-rays of energy 470.4 and 405.5 keV feeding the first and second excited states, respectively. The log ft value of 5.5 for the feeding of this level by decay of Ge^{66} points to possible spin and parity assignments of 0+ or 1+.

The Remaining Levels The positions of the remaining levels at energies of 536.9, 571.7, 657.0, and 750.9 keV were established on the basis of the energy relationship among the observed gamma-rays and the previously proposed[97] decay scheme. The pattern of gamma-ray de-excitation from these levels (all apparently 0+ and/or 1+) is peculiar in that higher energy transitions to states of similar spin and parity which would be expected to be favored are not observed. Coupled to this is the fact that although Ge^{66} has a decay energy of 3.0 MeV[64], the highest postulated level fed by beta decay is 751 keV. Thus there is a possibility that certain of the transitions postulated as de-exciting the levels discussed above which show anomalous character could be part of cascades from higher energy levels (above 751 keV) to the lower established levels.

7.3 The Decay of Ga^{68} The levels in Zn^{68} populated in the positron decay of 68-minute Ga^{68} have been studied by observing decay gamma-rays with Ge(Li) detectors. The results which have been obtained are in agreement with previous studies,[64] but as explained below, the results are to be taken as of a preliminary nature.

7.3.1 Source Preparation Sources were prepared by two different nuclear reactions which aided in differentiating between gamma-rays from the nucleus under study and from impurity activities. In one method, metallic targets of chemically pure zinc were irradiated with 26-MeV alpha particles at the University of Washington cyclotron. After a period of approximately two months in which all of the germanium and gallium activities, except Ge^{68} (280 day), were presumed to have decayed away, the Ge^{68} activity was separated by the method as previously described. The reportedly pure electron-capture decay of the Ge^{68} to Ga^{68} provides the required activity.

Sources were also prepared by irradiating chemically pure gallium metal with 14 MeV neutrons from the Texas Nuclear Corporation model 9900 neutron generator of this laboratory. Activity produced includes Ga^{68} by the $Ga^{69}(n,2n)$ reaction, Ga^{70} by $Ga^{71}(n,2n)$, Zn^{69m} by $Ga^{69}(n,p)$, and Zn^{71} by $Ga^{71}(n,p)$ reactions. No chemistry was performed.

7.3.2 Single Detector Measurements The gamma-ray single detector spectrum obtained with the 0.85 cm^3 Ge(Li) detector for a Ga^{68} source prepared by the first method described above is shown in Figures 59(a), (b). The results obtained for the determination of gamma-ray energies and intensities are shown in Table VIII; these include results obtained with the 8 cm^3 Ge(Li) detector and a Ga^{68} source prepared by neutron irradiation.

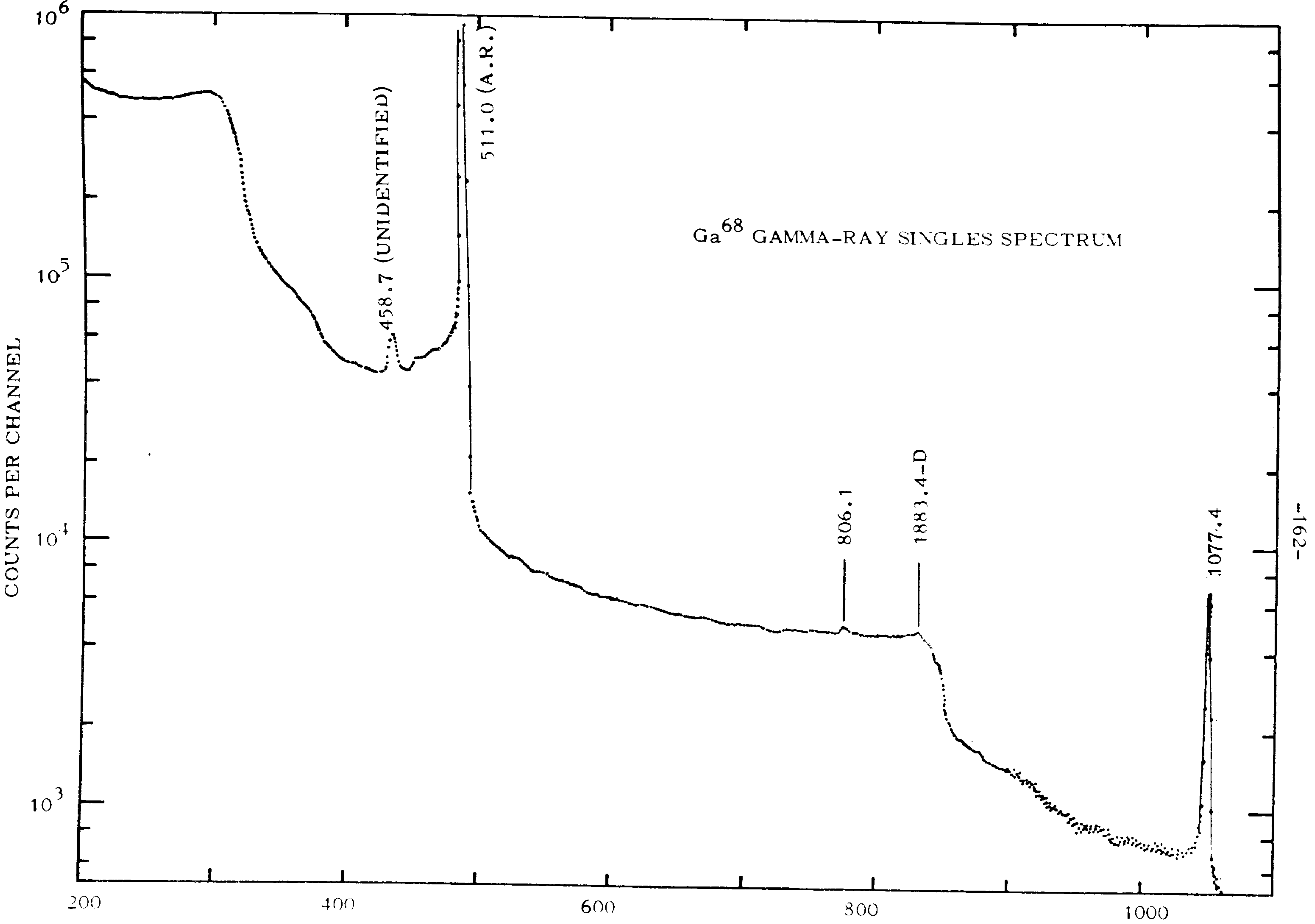

FIGURE 59 a

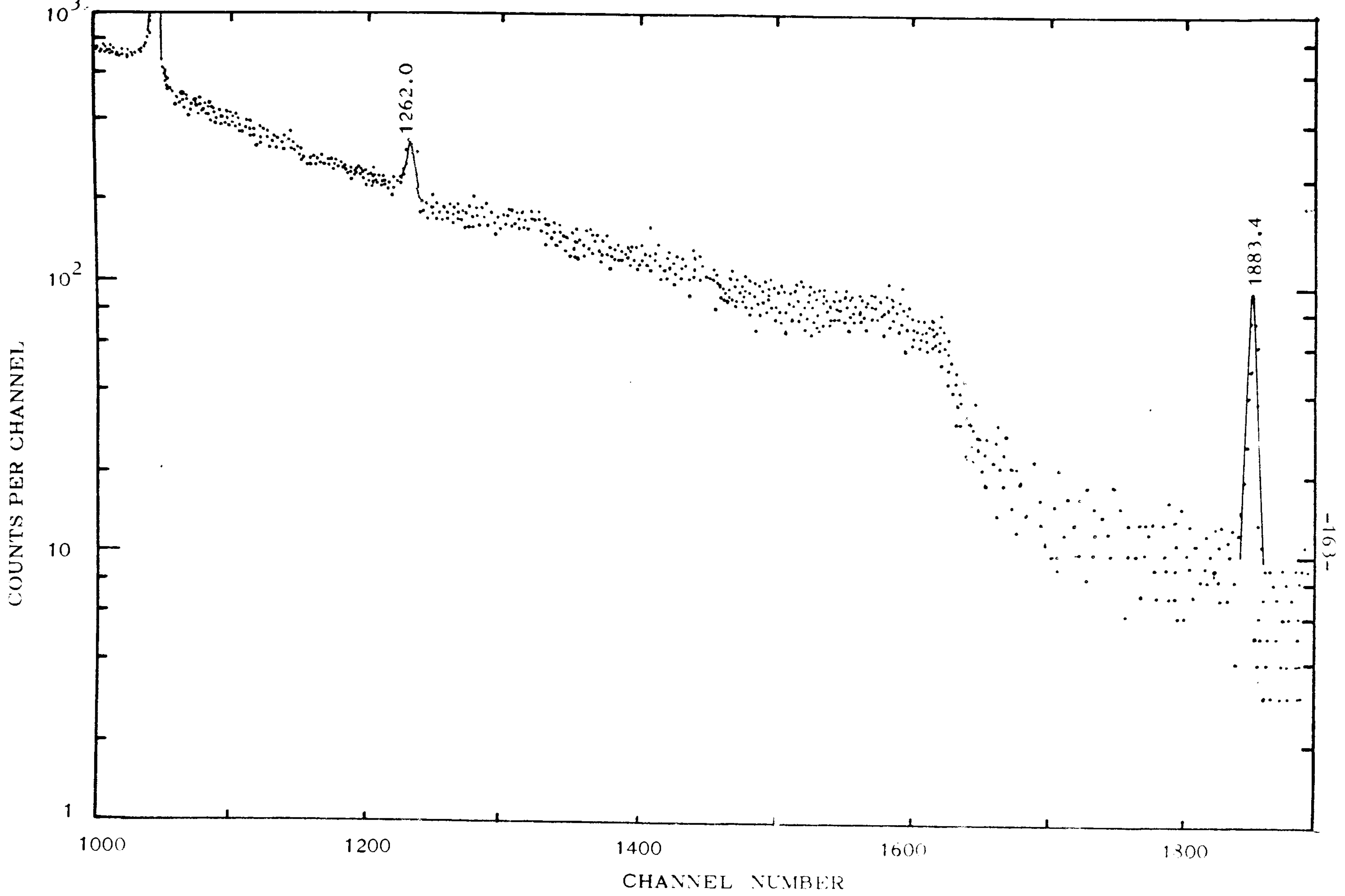

FIGURE 59 b

TABLE VIII:

Gamma-ray energy and intensity measurements on Ga^{68}

Present Work			Taylor and McPherson[117]	
E_γ (keV)	I_{rel}	%/decay	I_{rel}	E_γ (MeV)
806.1 ±0.5	2.0	0.10	12	0.80
1077.4 ±0.5 a)	100	5.0 b)	100	1.077
1262.0 ±0.5	3.6	0.18	4	1.26
			0.8	1.73 (?)
1883.4 ±0.5	4.0	0.18	4.2	1.87
(2339.4)	<0.1		0.13	2.32

a) 1077.6 0.8 keV measured with a Ge(Li) detector by Robinson, et.al.,[99] in Coulomb excitation of Zn^{68}.

b) assuming the positron branching ratio of reference 64.

The fairly intense peak at 458 keV shown in Figure 59(a) has not been assigned to the decay of Ga^{68} as it had not been detected in the measurement on the neutron-irradiated source using the 8 cm^3 detector. Gamma-rays not detected in both the samples prepared either by alpha-irradiation of zinc or neutron irradiation of gallium were designated as due to impurity activities

TABLE IX: Energies of gamma-rays assigned to impurity activities

Present Work		Previous Studies	
E_γ (keV)	Source	E_γ (keV)	Reference
439.3	Zn^{69m}	439	68
484.7	Zn^{71}	488	68
621.1	Zn^{71m}	620	68
1037.8	Ga^{70}	1042	64

Other gamma-rays of energy 576.[illegible] keV, [illegible] keV and 118[illegible] keV were detected in the sample prepared by the neutron irradiation of metallic gallium (but not in the chemically separated source) and could not be further identified.

7.5.3 Discussion of Results. The [illegible] ^{68} [illegible] is the same as proposed by previous workers [64]. The energy and intensity of gamma rays as obtained in the present work with Ge(Li) detector are more accurate than those previously reported. The spin and parity of levels as shown in Figure 60 for the present work were taken from the gamma-gamma angular correlation studies of Taylor and McPherson [illegible].

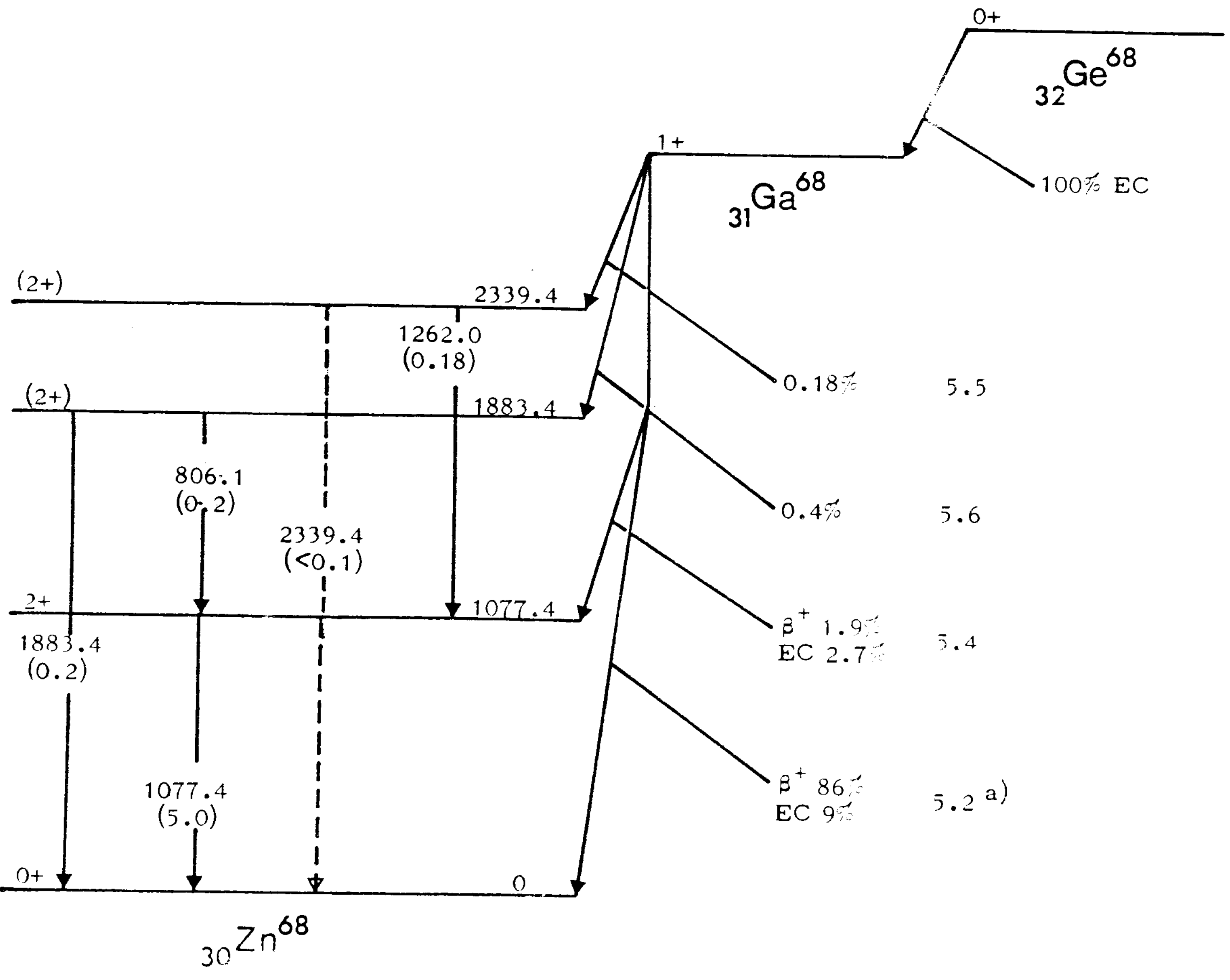

FIGURE 60

LITERATURE CITED

1. Adams, F., Nucl. Instr. and Meth. 48 338 (1967)

2. Alkhazor, G.D., Vorob'ev, A.A., and Komar, A.P., Bull. Acad. Sci. USSR (Physics Series) 29 1231 (1965); as cited in ref. 61

3. Antman, S.O., Landis, D.A., and Pehl, R.H., Nucl. Instr. and Meth 40 272 (1966)

4. Armantrout, G.A., IEEE Trans. Nucl. Sci. NS 13 (no. 1) 81 (1966)

5. Armantrout, G.A., IEEE Trans. Nucl. Sci. NS-13 (no. 3) 370 (1966)

6. Armantrout, G.A., Ibid., p. 328

7. Auble, R.L., McHarris, W.C., and Kelley, W.H., Nucl. Phys A91 225 (1967)

8. Benjamin, R.W., Buchanan, P.S., and Morgan, I.L., Nucl. Phys. 79 241 (1966)

9. Bienlein, J.K., and Dinter, H., Nucl. Phys. 55 113 (1964)

10. Bilger, H.R., and Mann, H.M., Bull. Am. Phys. Soc. 11 127 (1966)

11. Black, J.L., and Gruhle, W., Nucl. Instr. and Meth. 46 213 (1967)

12. Brown, W.L., and Wagner, S., ed., "Semiconductor Materials for Gamma-Ray Detectors," NRC Committee on Semiconductor Particle Detectors (June 24, 1966); unpublished

13. Brown, G., and Warren, S.E., Nucl. Phys. 77 365 (1966)

14. Burford III, W.B., and Verner, H.G., Semiconductor Junctions and Devices, p. 238, McGraw-Hill, New York (1965)

15. Camp, D.C., UCRL-50156 (March 1, 1967); unpublished

16. Camp, R., J. Appl. Phys. 25 489 (1954)

17. Cappelani, F., Fumagalli, W., Henuset, M., and Restelli, G., Nucl. Instr. and Meth. 47 121 (1967)

18. Carter, J., and Swalin, R.A., J. Appl. Phys. 31 7 (1960)

19. Cassatt, W., and Quigg, P.A., private communication

20. Chapman, G.T., Nucl. Instr. and Meth. 52 101 (1967)

21. Chasman, C., and Ristinen, R.A., BNL 8692 (December 1964)

22. Coleman, J.A., "Germanium for Gamma-Ray Detectors (A Review of Current Problems)," p. 37, IAEA Report on Lithium-Drifted Germanium Gamma-Ray Detectors, Panel Proceedings Series, Vienna (June 6, 1966)

23. Coleman, J.A., and Schwartzendruber, L.S., IEEE Trans. Nucl. Sci. NS-13 (no. 3) 240 (1966)

24. Crowell, C.R., and Sze, S.M., Appl. Phys. Lett., 9 242 (1966); as cited in ref. 61

25. Cumming, J.C., NAS-NRC Publication no. 3107, p. 25 (1962)

26. Cuttriss, D.B., Bell Sys. Tech. J. 40 590 (1961)

27. Davies, D.E., and Webb, P.P., IEEE Trans. Nucl. Sci. NS-13 (no. 1) 78 (1966)

28. Davisson, C.M., Chap. II, p. 37, Alpha, Beta, and Gamma-Spectroscopy, Siegbahn, K., ed., North-Holland, Amsterdam (1966)

29. Day, R.B., Dearnaley, G., and Palms, J.M., IEEE Trans. Nucl. Sci. NS-14 (no. 1) 487 (1967)

30. Dearnaley, G., and Northrop, D.C., Semiconductor Counters for Nuclear Radiations, 2nd ed., p. 25, Wiley, New York (1966)

31. Ibid., p. 71

32. Ibid., Chap. IV, p. 89

33. Ibid., pp. 123-126

34. Ibid., p. 196

35. de Castro Faria, N.V., and Lévesque, R.J., Nucl. Instr. and Meth. 46 325 (1966)

36. Diddens, A.N., Huiskamp, W.J., Severiens, J.C., Miedema, A.R., and Steenland, M.J., Nucl. Phys. 5 58 (1958)

37. Dolan, K.W., McDaniels, D.K., and Wells, D.O., Phys. Rev. 148 1151 (1966)

38. Easterday, H.T., Haverfield, A.J., and Hollander, J.M., Nucl. Instr. and Meth. 32 333 (1965)

39. Ewan, G.T., and Tavendale, A.J., Can. J. Phys. 42 2286 (1964)

40. Evans, J.S., Ph.D. Dissertation, Princeton University (1965)

41. Fano, U., Phys. Rev. 72 26 (1947)

42. Fox, R.J., IEEE Trans. Nucl. Sci. NS-13 (no. 3) 367 (1966)

43. Freedman, M.S., Porter, F.T., and Wagner, F., Phys. Rev. 151 899 (1966)

44. Freedman, M.S., Wagner, F., Porter, F.T., and Bolotin, H.H., Phys. Rev. 146 791 (1966)

45. Geballe, T.H., p. 341, Semiconductors, Hannay, N.B., ed., Reinhold, New York (1960)

46. Haering, R.R., and O'Hanlon, J.F., Proc. IEEE 55 692 (1967)

47. Hannay, N.B., Chap. I, p. 1, Semiconductors. Hannay, N.B., ed., Reinhold, New York (1960)

48. Hansen, M., and Anderko, K., Constitution of Binary Alloys, p. 745, McGraw-Hill, New York (1958)

49. Hansen, W.L., and Jarrett, B.V., Nucl. Instr. and Meth. 31 301 (1964)

50. Heath, R.L., USAEC Report IDO-16880-1, 2nd ed. (1964)

51. Henck, R., Stab, L., de Silva, G.L., Siffert, P., and Coche, A., IEEE Trans. Nucl. Sci. NS-13 (no. 3) 245 (1966)

52. Hoboken, Metallurgie, S.A., Hoboken, Belgium

53. Hollander, J.M., UCRL-16307 (1965)

54. Hornyak, W.F., Chap. IIA, p. 211, Nuclear Spectroscopy, Ajzenberg-Selove, F., ed., Academic Press, New York (1960)

55. Hotz, H.P., Mathieson, J.M., and Hurley, J.P., Nucl. Instr. and Meth. 37 93 (1965)

56. Jamini, M.A., IEEE Trans. Nucl. Sci. NS-14 (no. 1) 492 (1967)

57. Kashy, E., and Martin, R.E., Rev. Sci. Instr. 35 1364 (1964)

58. Katsanos, A.A., Huizenga, J.R., and Vonach, H.K., Phys. Rev. 141 1053 (1966)

59. Kingston, R.H., J. Appl. Phys. 27 101 (1956)

60. Kittel, C., Introduction to Solid State Physics, Chap. 10, p. 301, Wiley, New York (1967)

61. Klein, C.A., Raytheon Company Technical Memorandum T-751 (July 31, 1967); Bull. Am. Phys. Soc. 12 573 (1967)

62. Kopecky, J., Ratynski, W., and Warming, E., Nucl. Instr. and Meth. 50 333 (1967)

63. Lederer, C.M., Hollander, J.M., and Perlman, I., Table of Isotopes, 6th ed., pp. 188-189, Wiley, New York (1967)

64. Ibid., pp. 200-203

65. Ibid., p. 562

66. Ibid., p. 575

67. Levy, A.J., and Ritter, R.C., Nucl. Instr. and Meth. 49 359 (1967)

68. Li, A.C., and Monaro, S., Nucl. Phys. A91 353 (1967)

69. Lithium Corporation of America, New York, N.Y.

70. Llacer, J., IEEE Trans. Nucl. Sci. NS-11 (no. 3) 221 (1964)

71. Llacer, J., IEEE Trans. Nucl. Sci. NS-13 (no. 1) 93 (1966)

72. MacDonald, J.R., and Grace, M.A., Nucl. Phys. A92 593 (1967)

73. Malm, H.L., and Fowler, I.L., IEEE Trans. Nucl. Sci. NS-13 (no. 1) 62 (1966)

74. Mann, H.M., Bull. Am. Phys. Soc. 11 127 (1966)

75. Mann, H.M., Bilger, H.R., and Sherman, I.S., IEEE Trans. Nucl. Sci. NS-13 (no. 3) 252 (1966)

76. Mann, H.M., Janarek, F.J., and Helenberg, H.W., IEEE Trans. Nucl. Sci. NS-13 (no. 3) 336 (1966)

77. Many, A., Goldstein, Y., and Grover, N.B., Semiconductor Surfaces, Chap. 4, p. 128, North-Holland, Amsterdam (1965)

78. Ibid., p. 165

79. Mayer, J.W., J. Appl. Phys. 33 2894 (1962)

80. McGrory, J.B., Phys. Lett. 21 64 (1966)

81. Miller, G.L., "The Physics and Operation of Semiconductor Particle Detectors with Particular Reference to Gamma Detectors," p. 3, "Semiconductor Materials for Gamma-Ray Detectors," Brown, W.L., and Wagner, S., ed., NRC Committee on Semiconductor Particle Detectors (June 24, 1966); unpublished

82. Miller, G.L., and Gibson, W.M., Nuclear Electronics I, Conference Proceedings Belgrade, IAEA, Vienna (1961); cited in ref. 31

83. Miller, G.L., Pate, B.D., and Wagner, S., IEEE Trans. Nucl. Sci. NS-10 (no. 1) 220 (1963)

84. Miner, C.E., UCRL-11946 (February 24, 1965)

85. Minnesota Mining and Manufacturing Co.; #56 yellow, polyester, thermosetting electrical tape

86. Monteith, L.K., Rev. Sci. Instr. 35 388 (1964)

87. Moore, W.J., Physical Chemistry, p. 683, Prentice-Hall, Englewood Cliffs, N.J. (1962)

88. Northrop, D.C., and Simpson, O., Proc. Phys. Soc. 80 262 (1962)

89. Norton Company; diamond wheel, special type D1A1R, D-220-N, 100M-1/8, 6x0.024x1$\frac{1}{4}$"

90. "Notes on the Preparation of Semiconductor Materials," Materials Laboratory, Electrical Engineering Department, Imperial College, London (1964); unpublished

91. Paige, E.G.S., J. Phys. Chem. Solids 16 207 (1961)

92. Pell, E.M., J. Appl. Phys., 31 291 (1960)

93. Pettersson, H., Bergman, O., and Bergman, C., Ark. Fys. 29 423 (1965)

94. Popov, Yu. M., Soviet Researches in Luminescence, p. 62, Consultants Bureau, New York (1964); as cited in ref. 61

95. Reidy, J.J., and Weidenbeck, M.L., Nucl. Phys. 70 518 (1965)

96. Reiss, H., Fuller, C.S., and Morin, F.J., Bell Sys. Tech. J. 35 535 (1956)

97. Ricci, R.A., Girgis, R.K., and van Lieshout, R., Nucl. Phys. 21 177 (1960)

98. Ricci, R.A., Jacmart, J.C., Liu, M., Riou, M., and Ruhla, C., Nucl. Phys. A91 609 (1967)

99. Robinson, R.L., Stelson, P.H., McGowan, F.K., Ford, J.L.C., and Milner, W.T., Nucl. Phys. 74 281 (1964)

100. Ruddy, F.H., private communication

101. Sachs, M., Solid State Theory, Chap. 9, p. 244, McGraw-Hill, New York (1963)

102. Shapiro, M.H., Hinrichsen, P.F., Middleton, R., and Mohindra, R.K., Phys. Lett. 19 573 (1965); Hinrichsen, P.F., Shapiro, M.H., and Van Patter, D.M., Nucl. Phys. A101 81 (1967)

103. Sher, A.H., and Pate, B.D., "Techniques in Semiconductor Radiation Detector Fabrication," 21st Annual Meeting, ACS, N.W. Region (June 1967)

104. Sher, A.H., and Pate, B.D., Nucl. Instr. and Meth. 53 339 (1967)

105. Sher, A.H., and Pate, B.D., submitted to Nucl. Phys.

106. Sher, A.H., Pate, B.D., O'Hanlon, J.F., and Haering, R.R., Nucl. Instr. and Meth. 53 341 (1967)

107. Shockley, W., Solid-State Electronics 2 35 (1961); as cited in ref. 61

108. Sperduto, A., and Buechner, W.W., Phys. Rev. 134 B142 (1964)

109. Sproull, R.L., Modern Physics, 2nd ed., p. 266, Wiley, New York (1963)

110. Ibid., p. 387

111. Sullivan, M.H., and Eigler, J.H., J. Electrochem. Soc. 104 226 (1957)

112. Sylvania Electric Co., Chem. and Met. Div., Towanda, Pa.

113. Takacs, J., Nucl. Instr. and Meth. 33 171 (1965)

114. Tavendale, A.J., IEEE Trans. Nucl. Sci. NS-12 255 (1965)

115. Tavendale, A.J., IEEE Trans. Nucl. Sci. NS-13 (no. 3) 315 (1966)

116. Tavendale, A.J., and Fowler, I.L., Chalk River Report GPI-57, (November 1964)

117. Taylor, H.W., and McPherson, R.M., Can. J. Phys. 41 554 (1963)

118. Taylor, J.M., Semiconductor Particle Detectors, Chap. I, p. 1, Butterworths, London (1963)

119. Ibid., pp. 48-56

120. Ibid., pp. 124-126

121. Ibid., p. 162

122. Valdes, L., Proc. IRE 42 420 (1954)

123. van Roosbroeck, W., Phys. Rev. 139 A1702 (1965)

124. Veloric, H.S., and Greig, W.J., RCA Rev. 21 437 (1960)

125. Webb, P.P., Green, R.M., Fowler, I.L., and Malm, H.L., IEEE Trans. Nucl. Sci. NS-13 (no. 3) 351 (1966)

126. Webster's New Collegiate Dictionary, p. 153, Merriam, Springfield, Mass. (1953)

APPENDIX A

FOUR-POINT PROBE

A. The design of the four-point probe for measuring resistivities of surfaces of the germanium crystals was taken from Valdes[122] and is shown schematically in Figure A1. The probe itself consists of four steel pins arranged in a line and about 1 mm apart, imbedded in a block of Teflon. Current is passed through the two outer pins, and the floating potential is measured across the inner pair of pins. The source of DC-current was a 1.5 volt battery, the current was measured with a Triplett model 630-PLK volt-ohmmeter, and the voltage with a Hewlett-Packard model 419A DC-null voltmeter. For equally spaced probes, the resistivity is given by[122]

$$\rho = (V/I)2\pi s \qquad (\Omega\text{-cm}) \qquad \text{(A-1)}$$

where V is the measured floating potential difference between the two inner probes in volts, I is the measured current through the outer pair of probes in amps, and s is the spacing between the probes in cm. For probes 1 mm apart, equation A-1 becomes:

$$\rho = 0.63(V/I) \qquad (\Omega\text{-cm}) \qquad \text{(A-2)}$$

which is valid for measurements taken a distance $L \geq 3$ mm from an edge of the crystal. For measurements taken near an edge of the crystal (axis of probes parallel to edge), a correction factor F must be added:

$$\rho = \rho_o F(L/s) \qquad (\Omega\text{-cm}) \qquad \text{(A-3)}$$

where ρ_o is obtained from equation A-2, and the correction factor F is

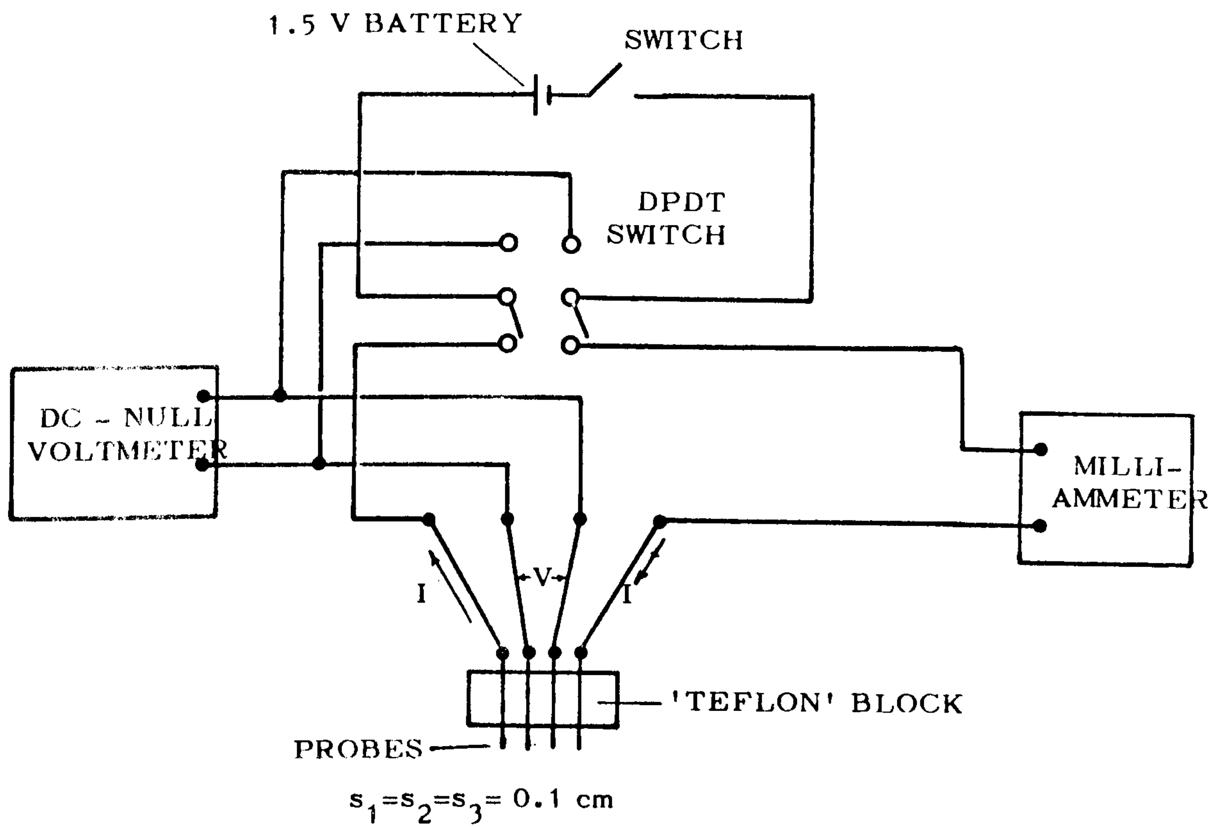

FIGURE A1

taken from charts given by Valdes[122]. A test of the four-point probe was made on a sample of germanium of 35-37 Ω-cm resistivity (data supplied by manufacturer). An average of 8 measurements on one surface of the lapped crystal yielded:

$$\rho = 0.63\left[\frac{0.028\text{ volts}}{0.0005\text{ amps}}\right] = 35.3\ \Omega\text{-cm}$$

APPENDIX B

CRYOSTAT DESIGN for Ge(Li) DETECTORS

B. Cryostats have been constructed for maintaining Ge(Li) detectors at 77°K and under high vacuum. The overall design of the cryostats was based upon that of Chasman and Ristinen[21] as shown in Figure B1. The detector mounting pedestals were based upon a design of Miner[64], and three modifications were built for use in the present work, as shown in Figure B2.

B.1 Basic Cryostat Design As shown in Figure B1, the outer vacuum jacket has been constructed of stainless steel; the vertical copper cold-finger is silver-soldered at the bottom of the outer jacket and extends into a Linde LD-25 "super-insulated" dewar. The horizontal copper member of the cold-finger clamps onto the top of the vertical member and is drilled to receive the aluminum detector mounting pedestal. The end-cap is of aluminum, and the electrical feed-through is a Microdot S-93 hermetically sealed connector which is mounted on the cryostat with low vapor-pressure epoxy cement (Varian Assoicates, "Torr Seal"). The back wall of the vacuum chamber is drilled and tapped to receive a thermocouple gauge tube (Haystings-Raydist DV-6M) and suitable high vacuum valve. The original model used a 1 liter/sec ion pump to maintain the vacuum; however, later models have used activated charcoal as a cryo-adsorbant which when cooled to 77°K was capable of maintaining pressures below 10^{-5} mm Hg. Thus the dependence upon electricity for running vacuum pumps has been eliminated. Number 30 enameled copper wire used between the electrical feedthrough and the detector contact provides the necessary

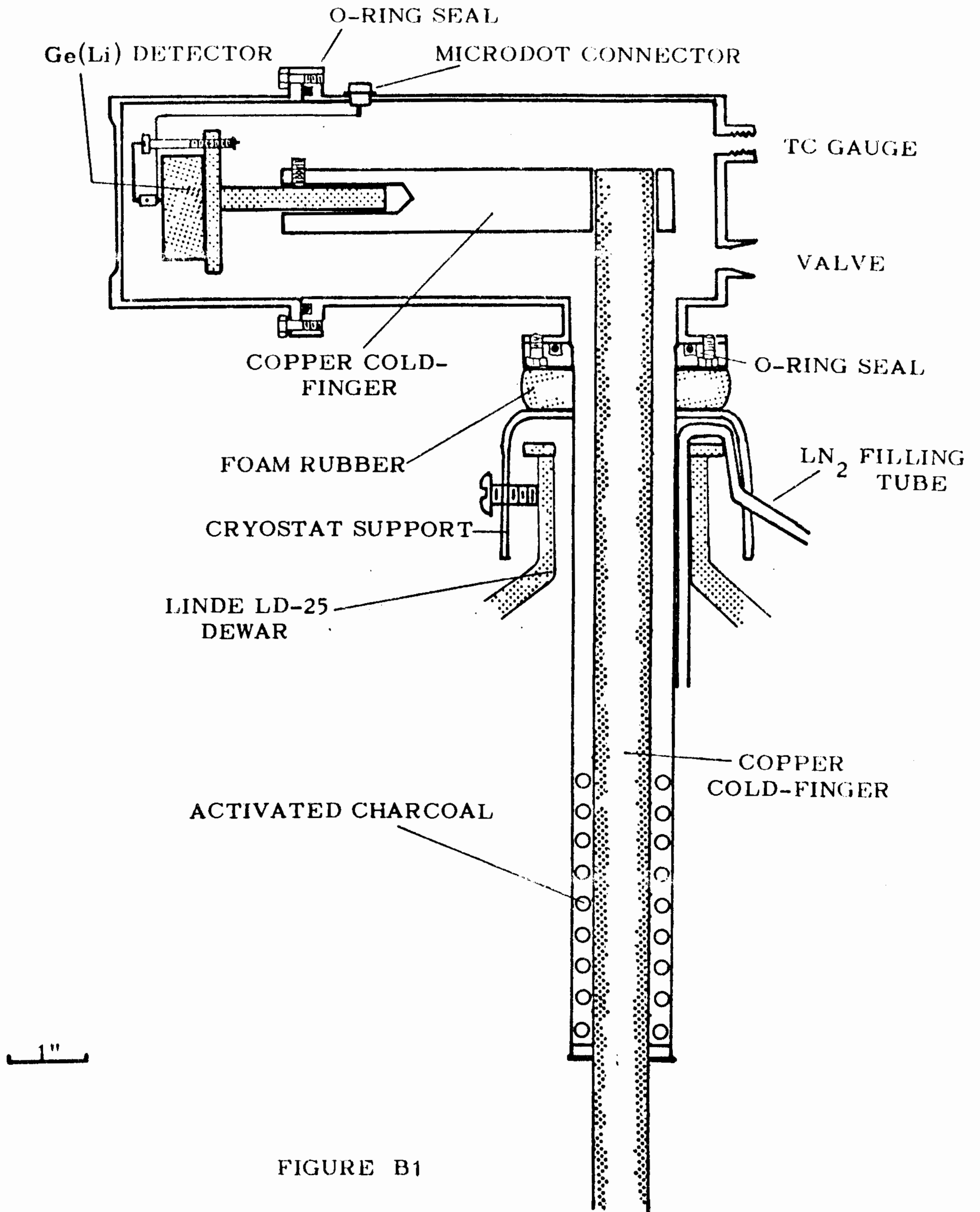

FIGURE B1

bias and signal connection between detector and preamplifier. The capacitance due to this system has been measured to be approximately 3-4 pf.

B.2 Detector Mounting Pedestals The three modifications of the detector mounting pedestal which have been used in the present work are shown in Figure B2. In modification A, the detector is held vertically so that radiation impinges on the face of the detector. As shown, a brass machine screw, which has been drilled to receive a length of spring steel wire onto which is afixed a Teflon insulator and copper contact, is threaded into the base of the aluminum pedestal. Modification B is essentially identical in construction to A, except the detector is held in a horizontal position; this mount which has been used in the CaF_2-coating procedure is shown in greater detail in Figure 25.

Modification C has been used for larger volume Ge(Li) detectors. For these detectors, the aluminum cap and supporting flange on the cryostat body have been enlarged. In this configuration, the detector is held on the pedestal by the copper contact which is afixed to a Teflon bar which in turn is held by two stainless steel screws. This mounting pedestal design permits rapid mounting of the detector, so that exposure of the freshly etched surface to the ambient is minimized.

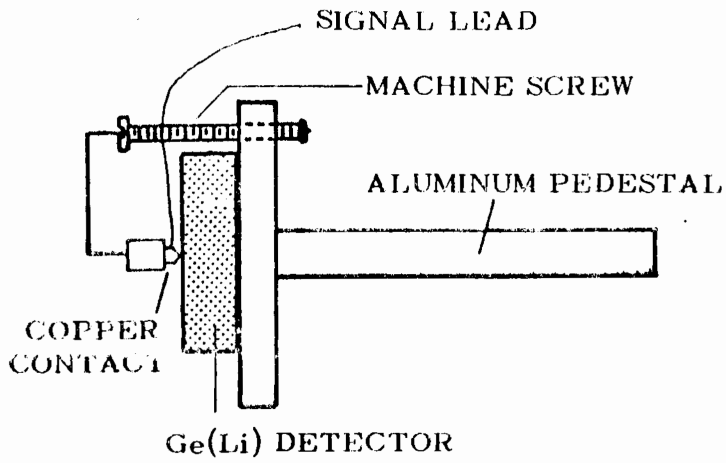

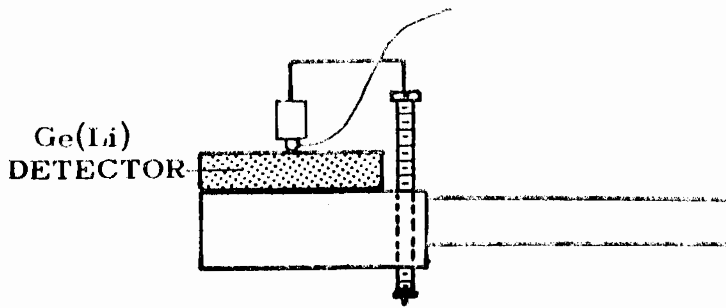

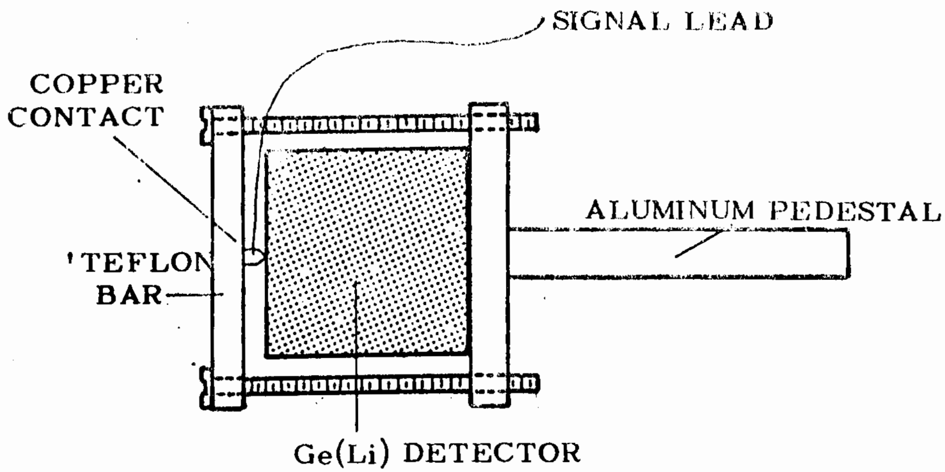

FIGURE B2

APPENDIX C

STANDARD GAMMA-RAY ENERGIES USED in CALIBRATION MEASUREMENTS

C. The energies of the gamma-ray standards listed below were taken from Lederer, et.al.,[65] and references cited therein.

Gamma-Ray Energy (keV)	Source
511.006 ±0.002 (m_oc^2)	Na^{22}
1274.53 ±0.10	Na^{22}
1368.526 ±0.044	Na^{24*}
2753.92 ±0.12	Na^{24*}
121.97 ±0.05	Co^{57}
136.33 ±0.04	Co^{57}
1173.226 ±0.040	Co^{60}
1332.483 ±0.046	Co^{60}
661.595 ±0.076	Cs^{137}
569.63 ±0.08	Bi^{207}
1063.58 ±0.06	Bi^{207}

* Produced by the $Al^{27}(n,\alpha)$ reaction using 14 MeV neutrons from the Texas Nuclear Corporation model 9900 neutron generator of this laboratory; all other sources obtained commercially.

APPENDIX D

FORTRAN PROGRAM 'MFIT'

D. A FORTRAN IV computer program, MFIT, has been used extensively for determining calibration constants and gamma-ray energies in Ge (Li) spectroscopy; the program was run on the Simon Fraser University IBM system 360/40 computer. The program consists of the MAIN program which controls the input and output of data, subroutine subprogram PFIT written by Mr. R. Ferguson of this university, which performs the least-squares fitting and computations of the constants of the polynomial (equation 6-2), and function subprogram GCALC which calculates gamma-ray energies from the constants and channel numbers. The subroutine PFIT performs the least-squares fitting procedure of the standard gamma-ray energies and peak locations (channel numbers) to polynomials starting with the specified degree M up to degree 10. The program compilation at the end of this section goes to degree 5, controlled by statement number 35 of the MAIN program. Any number of sets of data can be run.

A typical data deck will consist of the following:

CARD 1: BLANK

CARD 2: COMMENT CARD containing experiment identification, etc.

CARD 3: CONTROL CARD

```
1 2 3 4 5 6  7 ←—(col. numbers)
  M   N     NX
```

where M is the degree of the first polynomial fit (normally 2), N is the number of data cards with standard gamma-ray energies and channel numbers, and NX is the number of data cards with channel numbers for which the energy is to be calculated

CARD 4-N: Standard gamma-ray energies (cols. 1-10) and channel no. (cols. 11-20)

CARD 5-NX: Channel numbers of gamma-ray peaks whose energies are to be calculated (cols. 1-10)

LAST DATA CARD: BLANK if another data set follows (i.e., first card of following data deck), or containing the number "3" punched in col. 2 if final card of last data deck.

A listing of a typical data deck is as follows:

```
         GA 67    X10 40.650.51.0     150V    7/12/67 - COMMENT CARD
 2 6 16                           - CONTROL CARD
 121.97     165.0
 511.006    766.0
 749.4     1134.0
 846.6     1286.0      N = 6
1012.9     1542.0
1037.6     1582.0
 120.5
 235.0
 261.5
 299.5
 398.0
 414.0
 440.5
 528.5          NX = 16
 551.0
 584.5
 740.5
 766.0
1063.0
1207.0
1348.0
1581.5
```

(A typical data output is given in Table III)

```
FORTRAN IV G LEVEL 0, MOD 0                MAIN                 DATE = 67298          11/20/15          PA

0001     210     READ (5,110) LIMIT
0002     110     FORMAT (I2)
0003             IF (LIMIT.EQ.3) GO TO 200
0004             DIMENSION X(100),Y(100),A(11,11),B(11),C(11),P(20),CNUM(100),
               1RUN(20)
0005             READ (5,111) RUN
0006     111     FORMAT (20A4)
0007             READ (5,102) M, N, NX
0008     102     FORMAT (I2, I2, I3)
0009             DO 101  I=1,N
0010     101     READ (5,100)  Y(I), X(I)
0011     100     FORMAT (2F10.0)
0012             READ (5,107)  (CNUM(I), I=1,NX)
0013     107     FORMAT (F10.0)
0014             WRITE (6,112)  RUN
0015     112     FORMAT (1H1, 20A4//)
0016     1111    CALL PFIT (M,N,C,Y,X)
0017             MP = M + 1
0018             WRITE (6,1003)  (C(I), I=1, MP)
0019     1003    FORMAT (10X, E20.9///)
0020             WRITE (6,103)
0021     103     FORMAT (18X,1HX,11X,1HE,10X,6HE CALC///)
0022             DO 104  J = 1,N
0023             ESTD = GCALC(C, X(J), M)
0024     104     WRITE (6,105)  X(J),Y(J),ESTD
0025     105     FORMAT (10X, 3F12.3//)
0026             WRITE (6,109)
0027     109     FORMAT (//10X,11HCHANNEL NO.,10X,7HE GAMMA///)
0028             DO 190  J=1,NX
0029             ENX = GCALC(C,CNUM(J),M)
0030     190     WRITE (6,108)  CNUM(J),ENX
0031     108     FORMAT (10X, F11.3, F17.3/)
0032             WRITE (6,333)
0033     333     FORMAT (1H1)
0034             IF (M.EQ.5)  GO TO 210
0035             M = M+1
0036             GO TO 1111
0037     200     STOP
0038             END
```

```
FORTRAN IV G LEVEL 0, MOD 0                PFIT                DATE = 67298

0001              SUBROUTINE PFIT (M,NN,C,Y,X)
0002              DIMENSION X(100),Y(100),A(11,11),B(11),C(11),P(20)
0003              NUMBER = NN
0004       1111   MX2 = M*2
0005              DO 5 I=1,MX2
0006              P(I) = 0.
0007              DO 5 J=1,NUMBER
0008          5   P(I) = P(I) + X(J)**I
0009              N = M + 1
0010              DO 6 I=1,N
0011              DO 6 J=1,N
0012              K = I+J-2
0013              IF(K)7,7,8
0014          8   A(I,J) = P(K)
0015              GO TO 6
0016          7   A(1,1) = NUMBER
0017          6   CONTINUE
0018              B(1) = 0.
0019              DO 10 J =1,NUMBER
0020         10   B(1) = B(1)+Y(J)
0021              DO 11 I=2,N
0022              B(I) = 0.
0023              DO 11 J=1,NUMBER
0024         11   B(I) = B(I) + Y(J)*X(J)**(I-1)
0025              NM1 = N - 1
0026              DO 12 K =1,NM1
0027              KP1 = K + 1
0028              L = K
0029              DO 13 I=KP1,N
0030              IF(ABS(A(I,K)) - ABS(A(L,K))) 13,13,14
0031         14   L = I
0032         13   CONTINUE
0033              IF(L-K)15,15,16
0034         16   DO 17 J=K,N
0035              TEMP = A(K,J)
0036              A(K,J) = A(L,J)
0037         17   A(L,J) = TEMP
0038              TEMP = B(K)
0039              B(K) = B(L)
0040              B(L) = TEMP
0041         15   DO 12 I=KP1,N
0042              FACTOR = A(I,K)/A(K,K)
0043              A(I,K) = 0.
0044              DO 18 J=KP1,N
0045         18   A(I,J) = A(I,J) - FACTOR*A(K,J)
0046         12   B(I) = B(I) - FACTOR*B(K)
0047              C(N) = B(N)/A(N,N)
0048              I = NM1
0049         19   IP1 = I + 1
0050              SUM = 0.
0051              DO 20 J =IP1,N
0052         20   SUM = SUM + A(I,J)*C(J)
0053              C(I) = (B(I) - SUM)/A(I,I)
0054              I = I - 1
0055              IF(I)21,21,19
0056         21   CONTINUE
0057              RETURN
0058              END
```

FORTRAN IV G LEVEL 0, MOD 0 GCALC DATE = 67298

```
0001            FUNCTION GCALC (C,Z,M)
0002            DIMENSION C(11)
0003            GCALC = C(M + 1)
0004            DO 1  I = 1, M
0005       1    GCALC = GCALC * Z + C(M+1-I)
0006            RETURN
0007            END
```